Stellingen

behorende bij het proefschrift

"Heat Transport during Gas Tungsten Arc Welding".

1. De bewering van Eagar, dat de warmte-inbreng in het werkstuk bij gebruik van helium beschermgas groter is dan die bij gebruik van argon beschermgas omreden van de grotere warmtegeleidingscoëfficient van helium, is onjuist.
   T.W. Eagar, Advanced Joining Technologies, Chapmann and Hall, July 1990, p 61.

2. De bevinding van Cram, als zou de meeste warmte die ten goede komt aan de elektrode afkomstig zijn van straling, ontwikkeld in de boog, is een gevolg van het gebruik van niet van toepassing zijnde literatuurgegevens.
   L.E. Cram, J.Physics D: Applied Physics 16 (1983), p 1643.

3. De temperatuurprofielen, zoals die door Kou en Tsai voor een TIG-elektrode zijn berekend, leiden tot de fysisch onverklaarbare conclusie dat de warmte-ontwikkeling aan de tip van de elektrode negatief wordt bij hogere stroomsterkte.
   S. Kou, M.C. Tsai, Welding Journal Research Supplement 64 (1985), 9, p 266s.

4. Zij die voorstaan dat de waarde van de warmtecapaciteit van elektronen in een boogplasma niet gelijk is aan de waarde, die uit de klassieke statistisch-mechanische analyse volgt (C_p=3R/2), kunnen niet ongewijzigd gebruik maken van gemeten temperatuurprofielen waarbij deze benadering wel is gevolgd.
   C.J. Allum, Ph. D. thesis, Cranfield Institute of Technology, Cranfield (1982).

5. Het gebruik van de piektemperatuur in het werkstuk voor de berekening van de warmte-inbreng bij het booglassen, zoals gebruikt door Niles en Jackson, levert onbetrouwbare resultaten op.
   R.W. Niles, C.E. Jackson, Welding Journal Research Supplement 54 (1975), 1, p 25s.

6. Als alle fysische eigenschappen van materialen met een voldoende nauwkeurigheid bekend zouden zijn, zouden vele onderzoekers grote problemen ondervinden bij het "fitten" van hun fysisch model aan de experimentele resultaten.

7. Die studentengezelligheidsverenigingen, die in hun statuten de vergroting van de sociale vaardigheden van hun leden als één van hun doelstellingen hebben opgenomen, moeten zich node afvragen of zij hun leden niet zodanige omgangsvormen aanleren, dat het contact met niet-leden juist bemoeilijkt wordt.

8. Een slecht geweten gaat vaak samen met een slecht geheugen.
   K. Waldheim, diverse interviews voor schrijvende en beeldende pers.

9. Het uitwisselen van stellingen door promovendi, teneinde enkele niet uit het promotiewerk voortvloeiende stellingen te kunnen presenteren, is in strijd met het promotiereglement.

10. Zij die zich niet de moeite getroosten de taal van hun gastland te leren, geven daarmee uiting aan een gebrek aan respect voor 's lands cultuur.

Johan Zijp

Delft, oktober 1990.

Heat Transport during Gas Tungsten Arc Welding

Cover: A 150 A arc struck in argon shielding gas between a tungsten-2% lanthania electrode and a stainless steel workpiece.

Heat Transport
during
Gas Tungsten Arc Welding

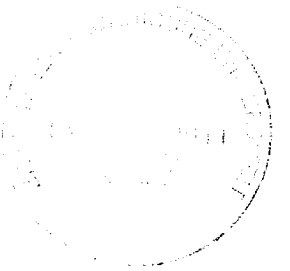

proefschrift

ter verkrijging van de graad van doctor aan de
Technische Universiteit Delft,
op gezag van de Rector Magnificus,
Prof. Drs. P.A. Schenck,
in het openbaar te verdedigen ten overstaan van een
commissie aangewezen door het College van Dekanen op

maandag 29 oktober 1990 te 16.00 uur
door

Johannes Petrus Zijp,
geboren te Langedijk,
metaalkundig ingenieur.

Dankwoord

Na 12 jaar aan de T.U. te hebben vertoefd, heb ik dan uiteindelijk mijn Delftse periode afgerond met de voltooiing van mijn proefschrift. Een en ander is natuurlijk niet volledig op eigen kracht gebeurd. Vele familieleden, vrienden, collegae en[1)] vakgenoten hebben op direkte en indirekte wijze hieraan bijgedragen. Een dankwoord aan al diegenen, die mij op enigerlei wijze hebben gesteund, is hier dan ook op zijn plaats.

Als eerste wil ik hierbij mijn ouders noemen, die altijd, zij het vrijwel nooit op de voorgrond, aanwezig zijn geweest.

Aad van der Voort, Gijs Kerkhof en Willem Brabander wisten de te fabriceren opstellingen te vervaardigen binnen een tijdspanne die in de meeste semi-overheids-instellingen voor onmogelijk wordt gehouden, en hebben daarmee veel bijgedragen aan de experimentele kant van mijn werk. Voor wat betreft de uitvoering van de proeven, is een belangrijk gedeelte van de resultaten beschreven in hoofdstuk vier van dit proefschrift, gebaseerd op het afstudeerwerk van Peter van Ingen.

Bij de uitwerking van deze, en vele andere resultaten, zijn de discussies met collegae uit mijn sectie van groot belang geweest. Hierbij wil ik met name Ben Stoop, Marcel Hermans en mijn kamergenoot Jan Paul Krugers noemen. Dat de voornoemde discussies niet altijd op het vakgebied betrekking hadden en vaak ook niet op het Laboratorium plaatsvonden, heeft in vele opzichten bijgedragen aan mijn plezierige tijd in Delft. Ook de overige leden van het G.G. wil ik in deze dankzegging betrekken.

Voor de verzorging van het tekenwerk heeft Jan Pehlemann gezorgd, die daarbij mijn wisselende typografische inzichten voor lief heeft genomen. Erik Thomassen heeft geholpen bij het ontwerpen van de omslag.

Verder wil ik Prof. L. van der Sluis van de T.U. Delft en Prof. W.R. Rutgers van de T.U. Eindhoven bedanken voor hun nuttig commentaar op het concept-proefschrift.

---

1) In een dankwoord als dit komen de beperkingen van de Nederlandse taal aan het licht. In het Japans, bijvoorbeeld, bestaan er verschillende vertalingen voor het Nederlandse woordje 'en'. Bij opsommingen zijn er twee mogelijkheden: als de opsomming volledig is, wordt in het Japans het partikel 'to' gebruikt, bij een onvolledige opsomming gebruikt men het partikel 'ya'.

Het moge de lezer duidelijk zijn, dat in dit dankwoord het woordje 'en' bij een vertaling in het Japans als 'ya' vertaald zou moeten worden.

Mijn broer Jan bedank ik voor vele correcties op mijn soms wat fantasierijk Engels taalgebruik.

Als laatste wil ik mijn promotor, Prof. G. den Ouden bedanken. Vanaf mijn kandidaatsexamen Metaalkunde heb ik in zijn sectie onderzoek mogen verrichten, en daarbij van de geboden experimentele vrijheid en de goede sfeer in zijn groep mogen genieten. Daarenboven heeft hij in alle bovengenoemde stadia van mijn promotie als (pro)motor van mijn onderzoek gefungeerd.

Delft, 1 sept. 1990

Johan Zijp.

Contents

1. General Introduction

Arc welding processes are of great importance in construction work. Welding has significant advantages over other joining processes when regarding cost and structural integrity. The history of welding dates back to the bronze age, i.e. around 3500 BC. The only joining process available at that time was hot forging. The first example of the joining of two ferrous metals dates from the era of Tutenkhamon (1350 BC). However, the actual development of welding as a joining technique for constructional use only starts in the 19th century. In 1885, the first patent on arc welding with a carbon stick electrode was granted to Bernados and Olszewski. This was followed by Slavianoff in 1889, who patented the arc welding with a melting metal electrode. Using these electrodes, weld quality is very low due to the absence of any form of protection of liquid metal against the environment. Thus, these processes did not gain instant recognition. The autogenous welding process patented in 1900 by Le Chatelier, however, was implemented by industry worldwide within a decade. Arc welding followed suit after Kjellberg patented the arc welding process with covered stick electrodes in 1907. The coating of these electrodes consisted mainly of paper, asbestos and chalk, sometimes mixed with other materials such as aluminium powder. The coatings provided an acceptable degree of protection of the liquid metal. This process is now known as shielded metal arc welding (SMAW). From 1930 to 1950, several other welding processes were developed. Among them were processes such as gas tungsten arc welding (GTAW), gas metal arc welding (GMAW) and submerged arc welding (SAW). During the last few decades all these processes saw a rapid development in terms of weld quality, urged by the ever improving steel quality.

The amount of money, involved in these four processes, is substantial. In 1981 the direct and indirect welding costs in The Netherlands amounted to about 3,000,000,000 DFL [1.1] (direct costs including materials and personnel, indirect costs comprising interest and depreciation). Welding costs amount to 10-20% of the total cost in metal industry. Therefore, any improvement in cost efficiency is of vital importance. In this respect, the GMAW process has significant advantages over the

SMAW and GTAW process. It was calculated [1.1], that GMAW bears only 33 to 42% of the costs involved in SMAW.

Despite the obvious advantages, industry in Europe has been less successful in implementing these cost efficient welding techniques than competitors in the U.S. and Japan [1.2]. Moreover, metal industry in The Netherlands has been even less successful than the metal industry in the rest of Europe [1.3]. This is attributed to a lack of knowledge in industry and inefficient knowledge transfer from research institutes and welding institutions to this industry.

Over the last few decades, emphasis in welding research has shifted from manual processes such as SMAW towards mechanized and automated processes such as GMAW and SAW. Robotic arc welding, using the GMAW and GTAW process, has also gained much impetus in recent years. With the increasing interest in mechanization and automation of the arc welding process, a lack of fundamental knowledge concerning arc physics has become apparent. In particular, the heat transport during arc welding is still poorly understood. In this respect, the heat flow mechanisms at the arc-electrode boundaries are of great importance. Although much literature exists on the subject, the complexity of the arc is such, that no comprehensive model has yet been developed.

The goal of this study is to gain fundamental knowledge about the heat flow processes occurring during arc welding by means of calorimetric and heat conduction measurements. In in-situ calorimetric experiments, the workpiece and electrode are cooled directly or indirectly by a liquid flow. The mass flow of liquid and its temperature rise are a direct measure of the amount of heat entering the workpiece and electrode. In heat conduction experiments the temperature cycle in the workpiece is used to calculate the workpiece heat flow. Since the measurement of the temperature cycle by thermocouples has the disadvantage of being an indirect method in which approximating analytic formulae have to be used to obtain the final results, calorimetric experiments are to be preferred.

This thesis is set up as follows. In Chapter 2, the theoretical background of arc welding processes and some important elements of arc physics are discussed. Special

attention is given to the heat transport mechanisms in the arc, in particular the heat transport from the arc to the anode and cathode.

Chapter 3 deals with calorimetric experiments. The calorimetric setup is described and the accuracy and reproducibility of the calorimetric method is discussed. The results of experiments on the influence of cathode composition, anode composition, arc length, arc current, polarity, shielding gas flow rate and shielding gas composition are presented.

In Chapter 4, experiments on the influence of ambient pressure and shielding gas composition are discussed. The experimental setup in the pressure vessel is described and a procedure is presented to calculate the heat flow to the workpiece from its thermal cycle. Results of heat conduction experiments carried out in the pressure vessel are given.

The results described in Chapters 3 and 4 are discussed in Chapter 5. The effect of the welding parameters on the heat flow to anode and cathode is explained in qualitative and quantitative terms.

In Chapter 6, an adjusted heat flow model is proposed on the basis of the discussion given in Chapter 5.

References

1.1 J.Ph. van Dok, A.J. Nooijens,
"De lastechniek in Nederland".
Report AGA (1983).

1.2 P.C. Hobart,
"The future of the European welding industry".
Metal Construction (1983),1, p 11.

1.3 H.R. Commandeur, P. Taal,
"Netwerken en de diffusie van nieuwe lastechnieken in het midden- en kleinbedrijf".
Report RvB 354-89, Erasmus University Rotterdam (1988).

2. Theoretical background

2.1 Introduction

Arc plasmas are widely used as concentrated heat sources in welding processes and in furnaces in the metallurgical industry. Attempts to understand the physics of heat transport in arc plasmas date from 1955 [2.1]. However, in spite of the research efforts made over the years, the fundamentals of heat flow during arc welding are still poorly understood. This is mainly a consequence of the lack of theoretical insight into plasma processes. Especially, non-equilibrium situations at the plasma-electrode interfaces still pose a huge challenge. Due to the small dimensions of these transition regions, experimental determination of the local plasma state is practically impossible. Results of calculations performed in the last decennium are inconsistent due to the lack of data on the physical properties of the species involved and the complexity of the problem in general [2.2, 2.3].

In this chapter, a physical description of the structure of the welding arc is given. Furthermore, the theoretical background of heat transport processes is discussed. Arc physics is dealt with in the next section. The heat transport processes which play a role in the welding arc and workpiece are reviewed in § 2.3.

2.2 Structure of the welding arc

2.2.1 General characteristics of the arc

A welding arc is an electric discharge in a partially ionized gas (plasma). Arc discharges can be distinguished from other forms of discharges (glow, corona, lightning) by their relatively high current (10 to 1000 A) and low voltage (10 to 40 V). In the low-current region, a lower limit exists because the plasma temperature decreases with decreasing arc current, ultimately resulting in an insufficient degree of ionization. To maintain a sufficient degree of ionization, arc voltage increases and the glow discharge regime is entered. When constricted arcs are used, as in plasma welding, a lower arc current can be employed. Generally speaking, there is no upper limit to arc current, though arc stability may suffer as the arc plasma becomes turbulent at high arc current.

The most readily obtainable parameters governing arc behaviour are the arc current and the arc voltage. Arc voltage usually decreases with arc current up to about 50 A and shows a slight increase at higher current (see Fig. 2.1). The minimum in the arc voltage-arc current characteristic also depends on arc length and on the composition of the shielding gas, the anode and the cathode.

When arc length is increased, arc voltage increases as well. This increase is approximately proportional to arc length, suggesting that the field strength in the arc column is independent of arc length. The state of the electrodes is of great importance to the arc voltage. As the electrodes' surfaces play a significant role in the physics of the arc, changes in the thermodynamic state of these surfaces can substantially affect arc voltage. This is demonstrated by the often observed irreversible behaviour of the arc. In such a case, once arc current is increased from a certain level, decreasing the current to the original level does not produce the original arc voltage.

The arc is constricted in both the anode region and cathode region. Based on the type of constriction and the arc appearance, various modes are distinguished. Basically, two cathode modes exist. In the normal mode (NM), arc attachment to the cathode is more or less diffuse. In the cathode spot mode (CSM), a constricted spot

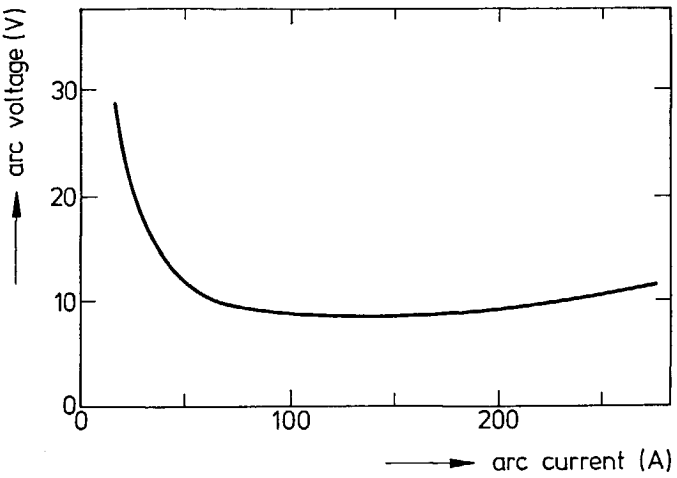

Figure 2.1 : A typical arc current-arc voltage characteristic of a Gas Tungsten Arc.

is observed, which is sometimes found to move rapidly over the cathode surface. Arc voltage is higher in CSM. For the anode, a similar distinction can be made. In the normal mode (NM), the arc is diffusely attached to the anode. When the anode spot is constricted (anode spot mode, ASM), arc voltage is higher and the arc moves rapidly over the anode surface. Although the onset of these modes is governed primarily by arc current, arc mode can change due to the thermodynamic state of the electrode surfaces. These observations lead to the conclusion, that the reproducibility of arc discharges is limited.

The welding arc can be divided into three regions (Fig. 2.2): the arc column, the anode fall region and the cathode fall region. The arc column is a region, in which well established plasma physics theories can be applied. The plasma in the arc column is considered to be in Local Thermodynamic Equilibrium (LTE), i.e. the energetic coupling between electrons and heavy particles is relatively strong and electrons and heavy particles are in mutual equilibrium (i.e. have the same temperature). Total equilibrium does not exist, since the electrons and heavy particles are not in equilibrium with the photons, which can escape from the plasma. The field strength in the arc column is relatively low (~10^3 V/m) and its temperature is high (5000-25000 K).

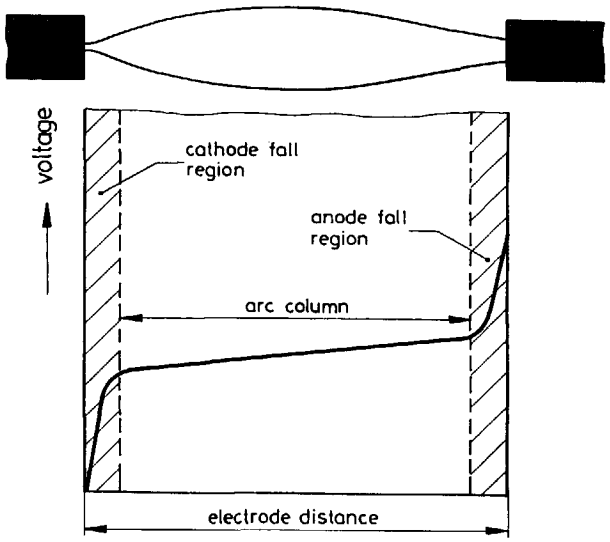

Figure 2.2 : A simple model of the welding arc.

Near the electrodes, two layers of a thickness in the order of the electron mean free path (typically several microns) are formed. These layers are known as the anode fall region and cathode fall region. The electric field strength in these regions can be as high as 10^7 V/m. Due to the high field strength and the modest collision frequencies, the electron temperature and heavy particle temperature deviate significantly.

In Fig. 2.2, three voltage drops can be distinguished. The total arc voltage V_t consists of the voltage drop over the anode fall region V_a, the voltage drop in the cathode fall region V_c and that in the arc column V_p

$$V_t = V_a + V_c + V_p \tag{2.1}$$

In the next sections, a more comprehensive description of the arc column, the anode fall region and the cathode fall region will be given.

Arc column temperature

The most important parameter governing arc plasma behaviour is plasma temperature. To maintain a sufficient degree of ionization, the plasma temperature has to exceed 10000 K for arcs in inert gases and 5000 K for metal vapour arcs. The degree of ionization α is a function of temperature, as Saha has shown using a statistical mechanics analysis

$$\frac{\alpha^2}{1-\alpha^2} = 3 \cdot 10^{-7} \frac{T^{5/2}}{p} \exp\left(-\frac{E_i}{kT}\right) \tag{2.2}$$

In this equation, T, p, k and E_i represent temperature, pressure, the Boltzmann constant and the ionization energy.

The arc temperature can be measured spectroscopically and by means of electrostatic probes. In spectroscopic experiments, the spectrometer measures all radiation produced in a small bundle, crossing the arc. A so-called Abel transformation of the spectroscopic data is necessary to obtain the radial temperature profile. The prime source of error in the measurement of the temperature profile is the sensitivity of the Abel transformation to small changes in spectroscopic data from the arc boundary. Furthermore, the emissivity of the plasma is unknown. Line intensity ratios can be used to circumvent this problem. Results obtained from spectroscopic analysis show, that arc column temperature is high in the vicinity of the cathode (15000 to 25000 K) and drops to about 10000 to 15000 K above the anode [2.4, 2.5] (see Fig. 2.3). The spatial resolution of this method is in the order of 0.1 mm.

With thin tungsten probes which sweep through the arc, the ion and electron densities can be obtained [2.6]. From these data, arc temperature can be calculated using the Saha equation (2.2). The main uncertainty in this method emanates from the capturing mechanism of the ions and electrons. To obtain accurate results, corrections have to be made for the depletion of ions and electrons around the probe and for the chilling effect of the probe on its surroundings [2.7].

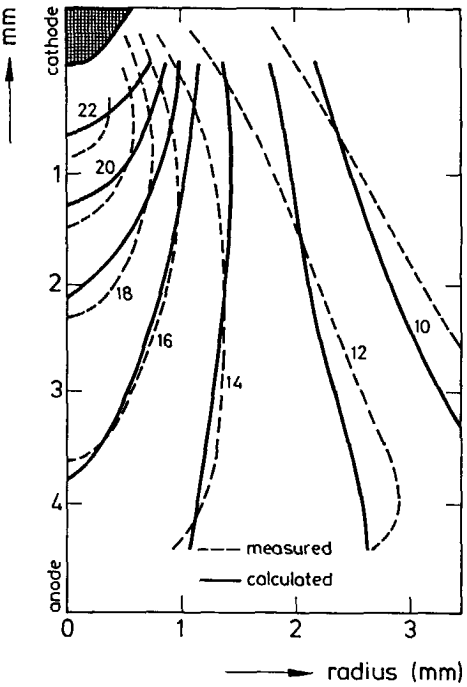

Figure 2.3: A typical temperature profile of the arc (from [2.5], temperatures in thousands of K).
200 A arc current, argon shielding gas.

Electrical properties

As the inertia of electrons is much smaller than that of ions, charge transport is realized primarily by electrons. A good estimate of the proportion of the current carried by ions is given by the relative mobility of the electrons and ions: $\sqrt{(m_e/m_i)}$, in which m_e and m_i are the electron and ion mass. For argon, the ion current contribution amounts to about 0.4% of the total arc current. In helium, this fraction is about 1.2%.

The electrical conductivity and the electric field strength are of prime importance in describing the heat balance of the arc column. In the one-dimensional case, the heat production in the arc column per unit volume, Q, can be written as

$$Q = \sigma E^2 \tag{2.3}$$

In this equation, σ represents the electrical conductivity and E the electric field strength.

Assuming LTE, electrical conductivity is only dependent on plasma composition, ambient pressure and temperature. The conductivity can then be calculated using a statistical mechanics analysis [2.8]. As the electrical conductivity is closely related to the electron density, it will show a similar dependence on temperature. Conductivity in an argon plasma is negligibly small at plasma temperatures below 5000 K and reaches a plateau at a temperature of about 20000 K. At this temperature, all argon atoms are at least singly ionized. Due to the higher ionization energy of helium, the electrical conductivity of helium is lower than that of argon at plasma temperatures below 20000 K.

Data on the influence of pressure are less explicit. According to the Saha equation (2.2), the degree of ionization α decreases with pressure. The electron density ($\alpha p/kT$), however, shows a more complex dependence on ambient pressure. It can be deduced from equation (2.2), that the electron density increases with the square root of the ambient pressure at plasma temperatures at which the degree of ionization is low, and shows a proportional dependence on ambient pressure for sufficiently ionized plasmas. This results in the electrical conductivity to increase with ambient pressure at plasma temperatures of about 15000 K and above, and to decrease with ambient pressure at plasma temperatures lower than about 10000 K.

Ambient pressure also affects heat transport mechanisms in the arc, such as convection, conduction and radiation. Thus, the arc temperature profile will change as ambient pressure is changed. It is evident that in a welding arc, the effect of pressure on the electrical conductivity and arc temperature profile can not be calculated using the limited data just given.

The electric field strength in the arc column is relatively low. For argon, values of around 0.8 V/mm are reported. In helium, values of 1.5 to 2 V/mm are found. The electric field strength is usually assumed to be independent of the axial position in the arc. Investigations have shown, that this assumption may not be correct. In argon, for example, values of 1.5 to 2.5 V/mm have been reported near the cathode [2.7, 2.9, 2.10]. The electric field strength is usually calculated from the slope of arc voltage-arc

length curves. Assuming the voltage drops near the electrodes to be independent of arc length, this will yield reliable field strength values.

Arc voltage-arc length curves show an essentially linear behaviour, with a slope which decreases only slightly as arc length is increased. Some investigators have found arc voltage to increase as arc length was decreased below values of 0.5 mm [2.11]. This behaviour is more pronounced at low arc current (< 50 A) and is probably associated with an encounter of the anode and cathode transition regions.

Radiation, convection and conduction

The arc plasma loses energy by three mechanisms : radiation, convection and conduction. Radiation is produced as a result of inelastic collisions of particles. Conduction is based on elastic collisions. Both mechanisms depend primarily on the nature and the relative velocities of the particles, i.e. on the composition and temperature of the plasma. Convection is due to the drift velocity of the plasma as a whole.

Radiation can be produced in free-free, free-bound, bound-free and bound-bound transitions. The bound-bound transitions generate a discrete spectrum which is often used in spectroscopic emission measurement of the plasma temperature. The other transitions give rise to a continuum spectrum. Many experiments have been done to determine the radiative source strength of the arc plasma. Evans [2.10] measured the radiation produced in argon plasmas and found the radiative source strength to be in the order of 10 W/mm^3 at plasma temperatures of 10000 to 20000 K. For plasmas containing 1 at.% iron, this increases to above 1000 W/mm^3. It should be noted, however, that the arc temperature decreases when low ionization constituents are present. Thus, the difference in radiative power will not be as high as can be concluded from the data just presented.

Not all radiation produced escapes from the arc plasma. Photo ionization and other processes involving photons, will reduce radiative losses. Arc plasmas are usually regarded as optically thin [2.12], i.e. no absorption takes place and all radiation produced escapes from the arc. Allum [2.7] measured the total radiation in argon arcs and found it to account for about 20% of the power appearing in the arc

column. Compared to the arc power, radiation accounted for 3 to 8% of arc power depending on arc length (2 to 8 mm). In helium, the absolute radiative power loss was found to be as high as in argon. Due to the higher field strength in helium plasmas, however, the percentage of arc power and column power appearing as radiation is lower in helium arcs. Radiative losses from the arc increase as ambient pressure is increased.

Convection can be generated as a consequence of temperature differences in the arc (buoyancy). This mechanism, however, is totally overshadowed by the pressure build-up induced by Lorentz forces. Due to the high arc current involved, a significant interaction between the charge carriers and the arc magnetic field exists. Lorentz forces acting on the charge carriers induce a pressure build-up in the centre of the arc column, which increases as the arc radius becomes smaller. Maecker [2.13] has shown the pressure build-up to be equal to

$$p - p_0 = \frac{\mu_0 I^2}{4\pi R^2} \tag{2.4}$$

in which p, p_0, I, R and μ_0 represent the pressure in the arc column, the ambient pressure of the surrounding gas, the arc current, the arc radius and the permeability of vacuum. In this equation, the arc is supposed to have a cylindrical cross-section and current density is assumed to be constant over the entire cross-section. A correction factor should be applied to account for a Gaussian current density distribution.

As the arc is constricted at the cathode and diverges towards the anode, a pressure gradient exists which accelerates the arc plasma from the cathode to the anode. This results in the formation of a cathodic plasma jet. In some instances, the anode constriction gives rise to a similar anode jet. At the arc lengths employed in welding, the cathode jet usually dominates. The maximum plasma jet velocity v is related to the induced pressure difference between anode and cathode p_a-p_c by the equation

$$p_a - p_c = \tfrac{1}{2}\rho v^2 \qquad (2.5)$$

in which ρ is the plasma density.

This equation does not account for viscous losses in the arc. FEM calculations of the velocity field in arc plasmas which do include viscous effects arrive at plasma velocities of several hundred meters per second. Researchers employing laser techniques found a maximum plasma velocity of 105 m/s in the midplane of the arc [2.14].

A more indirect way to measure the plasma velocity, is to measure stagnation pressures at the anode [2.15] and the cathode [2.16]. A small hole in the anode or the cathode is connected to a pressure measuring device. A quadratic dependence of the anode pressure on arc current was found. By applying equation (2.5), plasma velocities of several hundred meters per second were calculated. Pressure measurements at the cathode, however, are less reliable, since the hole in the cathode significantly influences cathodic behaviour. It is thus impossible to measure the pressure at the cathode spot itself.

The mass flow due to convection is in the order of 50 mg/s [2.14, 2.17]. This convection by the cathode plasma jet forms a significant contribution to the anode heating. When an anode jet is formed, anode heat input is found to decrease [2.2]. This convective mass flow also accounts for some of the power losses in the arc column. The heated arc plasma will transfer part of its energy to the anode, but most heat will be lost to the surroundings. In argon arcs, convective heat losses amount to about 60% of the power appearing in the arc column. Due to the differences in density, specific heat and thermal conductivity, power losses in the column of a helium arc are mainly attributed to conductive processes.

When a weld pool is formed, the plasma jet depresses the weld pool and hence increases weld bead depth. The most important feature of the plasma jet, however, is its contribution to the directional stability of the arc. Thermally induced turbulence can decrease arc stability, as has been shown in experiments at elevated pressures [2.7].

It must be noted, however, that although plasma jet velocity is very high, the plasma jet does not prevent ions to travel from the anode to the cathode. Comparison

of the viscous and electric forces involved leads to the conclusion that the electric field strength in the arc column is high enough to dominate the ion flow and electron flow.

As was already stated, thermal conduction is due to elastic collisions between particles. As such, thermal conductivity can be calculated using similar statistical mechanics analyses, as those used to calculate the radiative power.

The thermal conductivity of argon plasmas and helium plasmas rises considerably with temperature. A slight maximum can be found at plasma temperatures where ionization and recombination processes contribute to the heat transport process. In molecular gases, the dissociation and recombination processes also give rise to an increase in thermal conductivity.

2.2.3 *Anode fall region*

As the anode itself does not produce ions, an excess negative charge is present in its vicinity, producing the anode voltage drop. This so-called anode fall region has dimensions in the order of the electron mean free path λ_e and the Debye length λ_d (the distance over which charged particles affect other charged particles). Both are in the order of 1 μm. Since ions do not exist in the anode fall region, all charge transport takes place by electrons. To comply with the charge neutrality principle in the arc column, ions are formed by thermal ionization in a boundary layer which covers the anode fall region. The boundary layer establishes a smooth transition from the anode fall region to the arc column and has a thickness of several hundreds of microns.

The physical processes taking place in the anode fall region are dependent on the plasma composition. In this respect, metal vaporization is expected to be of importance [2.18, 2.19]. Most metals have ionization energies much lower than those of the shielding gases commonly used in GTA welding. In gas metal arc welding (GMAW) and shielded metal arc welding (SMAW), metal drops traversing the arc produce significant amounts of metal vapour. Arc temperature in such arcs is found to be much lower than in gas tungsten arcs. In GTA welding, metal vapours have only been detected close to the anode surface [2.20]. These vapours can significantly

influence the processes in the anode fall region. Generally speaking, arc voltage is found to be lower when the anode contains elements with low ionization potential.

As mentioned earlier, two anode modes can be distinguished. The anode spot mode (ASM), is found to occur at an arc current below 50 A [2.21], but this transition current increases with increasing ambient pressure. Allum [2.7] found the anode spot mode to be buoyancy governed, i.e. ASM only occurred when the anode was placed below the cathode. In ASM, movement of the anode spot can increase arc length. The anode jet which is formed decreases the convective heat transport from the arc column to the anode. Thus, anodic efficiency will be lower in ASM than in the diffuse normal mode (NM).

In normal mode, the cathode jet dominates the plasma flow in front of the anode. The stagnation pressure measured at the anode is relatively low, typically 0.01 bar. The pressure at the anode increases with increasing arc current and decreases with increasing arc length. The associated arc force on the anode can give rise to a surface depression of the weld pool of several millimeters, thus increasing weld pool penetration.

The current density at the anode can be measured using a split anode, in which the arc current to both anode sections is measured. The arc is moved slowly across the anode and an Abel transformation can be used to obtain the radial current density profile. Nestor [2.22] used such an arrangement and arrived at peak current densities of about 10^7 A/m^2 for anodes in NM. Current density is usually described by a Gaussian distribution function. The half-width of this distribution is in the order of 2 to 4 mm for anodes in NM and increases with increasing arc current and increasing arc length [2.23]. The split-anode technique just described is also used to measure the heat flux distribution at the anode. Due to convective and radiative contributions, the half-width of the heat flux distribution is slightly larger than the half-width of the current density distribution.

The field strength in the anode fall region can be as high as 10^6 V/m. Direct measurement of this parameter, however, is practically impossible. Using the Poisson relation

$$\nabla \cdot \vec{E} = -\frac{\rho}{\varepsilon_0} \tag{2.6}$$

in which E represents the electric field strength, ρ the charge density and ε_0 the permittivity of vacuum and assuming the electron current density in the collisionless fall region to be totally determined by the electric field induced drift (i.e. electrons entering the fall region have no initial velocity), the Child-Langmuir expression can be obtained

$$\lambda \approx \left(\frac{4\varepsilon_0}{9}\right)^{1/2} \left(\frac{2e}{m}\right)^{1/4} \frac{V_a^{3/4}}{J^{1/2}} \tag{2.7}$$

in which λ, e, m, V_a and J represent the anode fall region thickness, the electron charge and electron mass, the anode voltage drop and the current density. Substituting appropriate values in equation (2.7) yields an anode fall region thickness of several micrometers, which is of the same order as the Debye length and the electron mean free path. With an anode voltage drop of several volts, a field strength of about 10^6 V/m is found.

Considerable confusion exists about the value of the anode voltage drop V_a. Basically, three methods have been employed to assess its value. In calorimetric experiments, extrapolation of the anode heat input to zero arc length eliminates radiative and convective column contributions. Using this method, the anode voltage drop is found to lie between 1 and 3 V.

With probe measurements, the plasma voltage in front of the anode can be measured. As the probe is several tenths of millimeters thick, this yields an upper estimate of the anode voltage drop. Anode voltage drops as high as 7 V have been reported.

Calculations by Dinulescu [2.2] on the distribution functions of the species involved in the anode fall region arrived at negative anode voltage drops, implying that a positive space charge exists in front of the anode. Negative voltage drops of -1

to -3 V were reported. The thickness of the anode fall region was calculated to be 1 to 2 μm. The anode boundary layer, which forms the transition between the arc column and the anode fall region, was found to be as thick as 500 μm.

No comprehensive mathematical modelling of the anode fall region has yet been performed. The basic problems are the deviations from equilibrium, which necessitate the adoption of two-temperature models, and the lack of knowledge of basic physical constants such as viscosity, electrical conductivity and thermal conductivity. Calculated anode voltage drops should therefore be judged with some skepticism.

2.2.4 *Cathode fall region*

The cathode fall region is the least understood region of the arc. Plasma temperature and field strength are higher than in the anode fall region. Unlike the situation in the arc column and in the anode fall region, charge transport takes place by both electrons and ions.

The physical processes occurring in the cathode fall region may be described as follows. Because of the high temperature and the high electric field strength at the cathode surface, electrons are emitted. This results in transpiration cooling, because in evaporating an electron, an energy equal to the work function of the cathode material is dissipated. After travelling a distance equal to the electron free path, electrons collide with heavy particles and thermal ionization takes place. In this collision zone, electrons leave in the direction of the anode, whereas the less mobile ions travel slowly to the cathode. Because of the limited mobility of the ions, a positive space charge is formed, producing the cathode voltage drop. The ions travelling to the cathode transfer part of their kinetic energy to the cathode. In addition, the ions are neutralized, releasing their ionization energy. This increases cathode temperature, favouring thermal emission of electrons.

Emission of electrons from the cathode can occur in the presence of high electric fields (field emission), or as a result of high temperature (thermal emission). Thermal emission is the most common mechanism in the case of refractory metals, as used in

GTA cathodes. The Richardson equation relates the current density J to the temperature T

$$J = AT^2 \exp\left(-\frac{\phi}{kT}\right) \tag{2.8}$$

in which ϕ is the work function of the cathode and A a constant depending on the cathode material. The constant A is about $6 \cdot 10^5$ A/m^2K^2 for most metals. Field emission only takes place when electric field strength is high enough. When field emission occurs, current density is extremely high ($\sim 10^{11}$ A/m^2). Current densities of this magnitude have never been found in welding arcs. It is suggested, however, that such a high field strength could exist when positive ions condense on isolating oxide films on the cathode [2.24].

The current density at the cathode is difficult to measure. A mean current density can be obtained when the cathode spot dimensions are known. Results from photographic estimates of the cathode spot diameter indicate that current densities of about 10^8 A/m^2 exist at pure tungsten cathodes. From the Child-Langmuir expression (equation (2.7)) given earlier, similar current densities are calculated. In GTA welding, the cathode usually consists of tungsten with possible additions of thoria or other oxides. Addition of oxides with a low work function is expected to increase cathodic current densities.

Current densities can of course be calculated using equation (2.8), if the cathode temperature is known. Measurement of the cathode temperature by spectroscopic means is tricky, however, because the arc produces a significant amount of radiation, which obscures the measurements. Electrode temperature is usually measured at some distance from the cathode tip. The temperature at the tip is then obtained by extrapolation. Tip temperatures of 2700 to 3600 K have thus been found [2.25]. Oxide containing electrodes showed a lower cathode tip temperature than pure tungsten electrodes.

The field strength in the cathode fall region is higher than in the anode fall region, typically 10^7 V/m. This is mainly due to the fact that the cathode voltage drop is

much higher than the anode voltage drop, typical cathode voltage drops being 5 to 10 V.

2.3 Heat transport processes

2.3.1 Heat transport in the arc

In this section, heat flow processes will be discussed for the arc column, the anode region and the cathode region. The heat transport during arc welding has been the subject of many investigations. One of the parameters which has received specific attention is the process efficiency. The process efficiency η is defined as

$$\eta = \frac{Q}{V_t I} \tag{2.9}$$

in which Q is the power transferred to the workpiece and V_t and I the arc voltage and arc current. In GTA welding, the workpiece is the anode and the tungsten electrode is used as cathode. A better approach, is to distinguish between anodic and cathodic efficiency, in which Q in equation (2.9) stands for the power transported to either anode or cathode.

Anodic efficiency is found to be as high as 75 to 85%, although values as low as 60% and as high as 95% are also reported. Anodic efficiency is observed to decrease with increasing arc length and increasing pressure. Data on the influence of arc current on anodic efficiency are inconsistent.

Cathodic efficiency has received much less attention, despite its influence on cathode erosion. In most cases, cathodic efficiency is found to be lower than 10%.

From the above figures follows that the heat loss in the column is relatively small. With an anodic efficiency of 75% and a cathodic efficiency of 5%, still only 20% of the arc power is lost in the arc column.

Arc column

In mathematical analyses of the arc column, the most accessible method is to write down the equations for the conservation of energy, momentum and mass.

In vector notation, the heat flow balance in a stationary situation can be written as

$$\sigma E^2 = C_p \rho \vec{U} \cdot (\nabla T) + \nabla \cdot (-\kappa \nabla T) + R \tag{2.10}$$

in which ρ, C_p, $\vec{U}$, T, κ and R represent the gas density, specific heat, velocity, temperature, thermal conductivity and radiative heat loss per unit volume. The left hand term is the power production per unit volume. The right hand terms express heat losses due to convection, conduction and radiation respectively. It should be noted, that the plasma velocity $\vec{U}$ is species dependent. Corrections should be made to account for the difference in drift velocities of electrons, atoms and ions. For this reason, the enthalpy transport due to electron drift is treated as a separate term in some mathematical analyses.

The conservation of momentum yields

$$\rho \vec{U}(\nabla \cdot \vec{U}) = -\nabla p + \eta \nabla(\nabla \cdot \vec{U}) + \vec{J} \times \vec{B} + (\rho - \rho_0)\vec{g} \tag{2.11}$$

with p the ambient pressure, η the viscosity, J the current density, B the magnetic induction, ρ the plasma density, ρ_0 the density of the surrounding air and g the gravitational constant. In this equation, the right hand terms express forces due to pressure gradients, viscous forces, electromagnetic forces and buoyancy respectively.

Finally, the law of conservation of mass dictates

$$\rho \nabla \cdot \vec{U} = 0 \tag{2.12}$$

In the arc column, no current field lines and magnetic field lines are generated. Furthermore, no space charge exists. This leads to the following conservation laws

$$\nabla \cdot \vec{J} = 0 \quad ; \quad \nabla \cdot \vec{B} = 0 \quad ; \quad \nabla \cdot \vec{E} = 0 \tag{2.13}$$

The set of equations (2.10) to (2.13) have not yet been solved. Simplifications made usually involve the assumption of a channel-type discharge with constant diameter, absence of radiation or convection, or the introduction of fixed temperature or current density distributions.

Some useful calculations have been performed by a.o. Hsu [2.26], Kovitya [2.27] and Ushio [2.4]. In general, calculated temperature and current distributions compare well to the results obtained experimentally. The relative contributions of radiation, convection and conduction in equation (2.10) have not yet been calculated with adequate accuracy, due to simplifications necessary in the mathematical analysis.

As was stated in § 2.2.2, the radiative term in equation (2.10) was measured to account for about 20% of the heat loss in the arc column in the case of argon. The convective term can account for as much as 60% of the total column power, but in helium arcs, the conductive term is thought to dominate.

Anode

A simple expression for the heat input to the anode Q_a, accounts for the contribution of the anode voltage drop V_a, the thermal energy of the impinging electrons, the work function of the anode ϕ_a and other column contributions consisting of radiation and conduction

$$Q_a = V_a I + \frac{3k\Delta T}{2e} I + \frac{\phi_a}{e} I + c_a V_p I \tag{2.14}$$

in which I, ΔT, c_a and V_p represent the arc current, the temperature difference between the arc column and the anode, a constant and the voltage drop over the arc column.

As has been shown in § 2.2.3, considerable confusion exists about the value of the anode voltage drop V_a. Values of -3 to 7 V are mentioned in literature.

The second term in equation (2.14) represents the Thomson effect (see Appendix B). Electrons entering the anode have an average thermal energy of 3kT/2. At an arc plasma temperature of 10000 K and an arc current of 100 A, this yields an

anode heat input of 130 W. When the work function of the anode is added, the total electron associated heat flow amounts to about 580 W (using ϕ_a=4.5 eV).

The column contribution to the anode heat input in equation (2.14) is the most difficult to assess. In equation (2.14), this contribution is described as a fraction of the column power. As this fraction c_a is a function of arc current, arc length and other parameters, this is probably not a very accurate approach. A better approach is, to separate the column contribution into a radiative and a convective term.

The radiative term is difficult to assess. The radiative power of the arc column is not known with adequate accuracy. Calculations are hampered not only by the inaccuracy of the arc column temperature profile, but also by uncertainties in the emissivity of the plasma, which has been taken to be as low as 0.01 to 0.001 [2.7]. Allum [2.7] measured the radiation from the arc column to account for about 20% of the arc power. With this figure, a simple approximation can be made. Assuming that half of this radiation reaches the anode and that the absorption coefficient of the anode averaged over all incident angles is 0.3, about 6% of the column power will be transferred to the anode. As the column power is 10 to 30% of the arc power, the radiative contribution to the anode will be 2% of the arc power at most. This is a very small contribution and can thus be neglected.

The foregoing implies that heat flow from the arc column to the anode region is mainly due to convection and conduction. Because of the plasma jet, a laminar boundary layer is formed in front of the anode which is much thinner than in the case of a buoyancy governed gas flow. In this boundary layer, heat transport occurs through conduction. As the axial heat transport by conduction is negligible compared with the axial heat transport by convection (plasma jet velocities being in the order of 100 m/s), the heat transport from the arc column to the anode region is referred to as the column convective contribution in this work, rather than as the column conductive contribution. This column convective contribution Q_{cv} can be described as

$$Q_{cv} = \frac{K\ A\ Nu\ \Delta h}{L\ C_p} \tag{2.15}$$

with K a constant, A the area of heat transfer, Δh the enthalpy difference between the hot gas and the anode, L the characteristic flow length, C_p the gas specific heat and

Nu the Nusselt number. For a flow impinging on a flat plate, the Nusselt number is defined by

$$Nu = B\ Re^{1/2}\ Pr^{1/3} \tag{2.16}$$

with B a constant (about 0.8 for arc plasmas) and Re and Pr the Reynolds and Prandtl numbers respectively.

There are many uncertainties in evaluating equations (2.15) and (2.16). Due to uncertainties in the temperature profile close to the anode, the gas density, specific heat and viscosity are not known with great accuracy. In addition, it must be noted that even the relationship between those physical properties and the temperature is not well established. Furthermore, the heat transfer area A and the flow length L are only known within certain limits. Finally, the constant K is dependent on the existence of LTE. In the absence of LTE, K may increase by two orders of magnitude.

Equations (2.15) and (2.16) have been evaluated by several workers and heat transport contributions of 5% [2.28] to 12-28% [2.16] of the total anode heat input were found for normal welding arcs (typically 100 A, 12 V). Ushio [2.29] used formulations which deviate from equations (2.15) and (2.16), and arrived at a convective contribution of 36% for a 2.16 kA arc at an arc voltage of 90 V. Wilkinson [2.30] performed experiments using an anode assembly consisting of three circular parts and found the convective contribution to account for over 50% of the total anode heat input for any arc length in excess of 6 mm.

It is evident that evaluation of the convective contribution to the anode heat transport is difficult. Contributions of 20% of the total anode heat input are thought to be reasonable for arcs operating in 'normal' welding situations.

Cathode

For the cathode, a similar heat transport equation as that of the anode (equation (2.14)) may be given. In this case, the work function and the Thomson effect act as a heat drain

$$Q_c = V_c I - \frac{3k\Delta T}{2e} I - \frac{\phi_c}{e} I + c_c V_p I \qquad (2.17)$$

in which ΔT and c_c represent the temperature difference between the arc column and the cathode and a constant.

The cathode voltage drop V_c is about 5 to 10 V and is usually obtained by applying equation (2.1). Extrapolation of the arc voltage to zero arc length eliminates the voltage drop over the arc column and V_c can be calculated by

$$V_c = V_t^{l=0} - V_a \qquad (2.18)$$

The Thomson effect is dependent on the electron temperature in the plasma adjacent to the cathode. A plasma temperature of 20000 K represents a realistic estimate. This means, that at an arc current of 100 A, the cooling of the cathode region due to the Thomson effect amounts to 260 W.

The work function is the most difficult parameter to assess. For pure tungsten, a value of 4.6 eV is usually adopted. For electrodes containing oxides, values as low as 2.4 eV have been reported. In the case of pure tungsten, the total electron-related cooling effect will thus be 720 W at an arc current of 100 A. Clearly, the heat production due to the cathode voltage drop in equation (2.17) has to be higher than this value in order to keep the electrode tip at a sufficiently high temperature.

2.3.2 *Heat transport in the workpiece*

For a large part, weld quality is controlled by the microstructural changes taking place in the workpiece as a result of the weld thermal cycle. The thermal cycle in and close to the weld bead is given schematically in Fig. 2.4 and has been the subject of both analytical and numerical analyses. The first analytical approach of the weld thermal cycle was given by Rosenthal [2.31]. Assuming that the heat source has infinitely small dimensions, that physical constants are independent of temperature and that no heat exchange with the environment takes place, equations were derived for 2-dimensional and 3-dimensional heat flow. In the 2-dimensional case, the plate

is regarded as thin, i.e. isotherms are perpendicular to the plate surface. The temperature is a function of time and place according to

$$\text{2-D} : \quad T(t,r) - T_0 = \frac{Q_a}{2\lambda d v}\left(\frac{\alpha}{\pi t}\right)^{1/2} \exp\left(-\frac{r^2}{4\alpha t}\right) \tag{2.19}$$

In the 3-dimensional case, the isotherms are semi-circular and the temperature at any time and place is governed by

$$\text{3-D} : \quad T(t,r) - T_0 = \frac{Q_a}{2\pi\lambda v t} \exp\left(-\frac{r^2}{4\alpha t}\right) \tag{2.20}$$

Here, T and T_0 represent the temperature at distance r from the weld centre line at time t and the plate temperature prior to welding. Q_a, v, d, λ and α represent the heat input, the travel speed, the plate thickness, the thermal conductivity and the thermal diffusion coefficient.

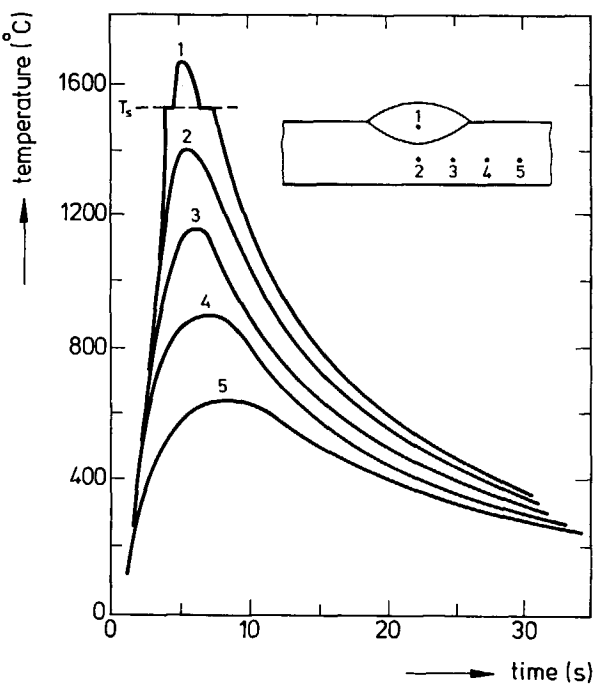

Figure 2.4: Schematic representation of the thermal cycle in a steel workpiece.

The peak temperature and cooling rate are the two most important characteristics of the thermal cycle, since they govern the weld metallurgical structure. The peak temperature determines which metallurgical reactions take place during the heating up period. The cooling rate determines whether there is sufficient time for the reverse reactions to take place during the cooling down period of the weld. If this is not the case, non-equilibrium structures are present after welding. In steel for example, martensitic structures can be found when the cooling rate has been too high. This seriously reduces the mechanical properties of the weld.

The peak temperature T_p is described by the following equations

$$2\text{-D} : \quad T_p(r) - T_0 = \left(\frac{1}{2\pi e}\right)^{1/2} \frac{\alpha Q_a}{\lambda d r v} \tag{2.21}$$

$$3\text{-D} : \quad T_p(r) - T_0 = \frac{2\alpha Q_a}{\pi e \lambda r^2 v} \tag{2.22}$$

Simple equations describing the cooling rate can only be extracted analytically from equations (2.19) and (2.20) for r=0. The equations thus obtained, however, have been found to accurately describe the cooling rate even at a fair distance from the heat source. The equations are

$$2\text{-D} : \quad \frac{\partial T}{\partial t} = - \frac{2\pi\lambda^2 d^2 v^2 (T - T_0)^3}{\alpha Q_a^2} \tag{2.23}$$

$$3\text{-D} : \quad \frac{\partial T}{\partial t} = - \frac{2\pi\lambda v (T - T_0)^2}{Q_a} \tag{2.24}$$

Distinction between the 2- and 3-dimensional approach can be made by combining equations (2.23) and (2.24), or equations (2.21) and (2.22). Thus, a critical thickness can be calculated.

In work on heat flow during arc welding, the thermal cycle of the workpiece can be used to obtain the anode heat input. To measure the thermal cycle, thermocouples

are placed in the workpiece. The heat input is then calculated from the thermal cycle by using one of the equations (2.21) to (2.24).

The most obvious drawback of the analytical approach is that physical constants are assumed to be independent of temperature. For example, in experiments using peak temperature, anodic efficiencies as low as 60% were calculated [2.32]. These values are thought to be unrealistic in view of data presented by other authors.

Modelling of the heat flow in the workpiece has also been done using a numerical approach. In numerical modelling of the heat flow in the workpiece, a distinction must be made between the rather straightforward formulations describing heat flow in the solid workpiece and those describing heat flow in the weld pool.

The heat flow in the solid workpiece can be described reasonably accurately using the analytical solutions just presented. Thus, emphasis in numerical modelling of the workpiece thermal cycle has shifted to the assessment of residual stresses. In this respect, the high temperature mechanical properties of the materials involved are of prime importance.

When modelling heat flow in the weld pool, the most important objective has been to find a relationship between the heat input and the weld pool size. In modelling the weld pool heat flow, the incorporation of fluid flow due to buoyancy, surface tension gradients and Lorentz forces still poses a challenge. The surface tension gradient is highly dependent on the chemical composition of the workpiece, as small amounts of surface active elements can profoundly alter weld pool dimensions [2.33]. The electro-magnetic Lorentz force in the weld pool is due to the divergence of the passing current. Thus, the current density distribution at the weld pool-arc interface is of great importance. Unfortunately, the boundary conditions at the weld pool-arc interface are not known with great precision.

References

2.1 G. Busz-Peuckert, W. Finkelnburg,
"Die Abhängigkeit des Anodenfalles von Stromstärke und Bogenlänge bei Hochtemperaturbögen".
Zeitschrift für Physik 140 (1955), p 540.

2.2 H.A. Dinulescu, E. Pfender,
"Analysis of the anode boundary layer of high intensity arcs".
Journal of Applied Physics 51 (1980), 6, p 3149.

2.3 D.M. Chen, E. Pfender,
"Two-temperature modeling of the anode contraction region of high-intensity arcs".
IEEE Transactions on Plasma Science PS-9 (1981), 4, p 265.

2.4 M. Ushio, F. Matsuda,
"Mathematical modelling of heat transfer of welding arcs (part 1)".
IIW Doc 212-528-82 (1982).

2.5 G.N. Haddad, A.J.D. Farmer,
"Temperature measurements in gas tungsten arcs".
Welding Journal Research Supplement 64 (1985), 12, p 339s.

2.6 M. Dudeck, G. Poissant, B.R. Rowe, J.L. Queffelec, M. Morlais,
"Plasma diagnostics by Langmuir probes and UV absorption".
Journal of Physics D: Applied Physics 16 (1983), p 995.

2.7 C.J. Allum,
"The characteristics and structure of high pressure (1-42 bars) gas tungsten arcs".
Ph. D. thesis, Cranfield Institute of Technology, Cranfield (1982).

2.8 S. Chapman, T.G. Cowling,
"The mathematical theory of non-uniform gases".
Cambridge University Press, Cambridge (1952).

2.9 H. Olsen,
"Temperature measurements in high current arc plasmas".
American Physical Society Bulletin (1957), 1, p 81.

2.10 D.L. Evans, R.S. Tankin,
"Measurement of emission and absorption of radiation by an argon plasma".
Phys. Fluids 10 (1967), 6, p 1137.

2.11 K. Ando, J. Nishikawa,
"Studies on anode and cathode energy of TIG arc".
IIW DOC 212-158-68 (1968).

2.12 K.C. Lapworth,
"Spectroscopic temperature measurements in high temperature gases and plasmas".
Journal of Physics E: Scientific Instruments 7 (1974), 6, p 413.

2.13 H. Maecker,
"Plasmaströmungen in Lichtbogen infolge eigenmagnetischer Kompression".
Zeitschrift für Physik 141 (1955), p 198.

2.14 G. Seeger, W. Tiller,
"Laser diagnostics on the TIG arc".
Conference on Arc Physics and Weld Pool Behaviour, London (1979).

2.15 A. Sadek, M. Ushio, F. Matsuda,
"Gas-tungsten-arc cathode and related phenomena".
Transactions of the Japanese Welding Research Institute 16 (1987), 1, p 195.

2.16 P.A. Schoeck,
"An investigation of the anode energy balance of high intensity argon arcs in argon", in :
"Modern developments in heat transfer".
Academic Press, New York & London (1963).

2.17 K.C. Hsu, K. Etemadi, E. Pfender,
"Study of the free-burning high-intensity argon arc".
Journal of Applied Physics 54 (1983), 3, p 1293.

2.18 G.J. Dunn, T.W. Eagar,
"Metal vapours in gas tungsten arcs: Part II.
Theoretical calculations of transport properties".
Metallurgical Transactions A 17A (1986), 10, p 1865.

2.19 T.F. Chase, W.F. Savage,
"Effect of anode composition on tungsten arc characteristics".
Welding Journal Research Supplement 50 (1971), 11, p 467s.

2.20 G.J. Dunn, C.D. Allemand, T.W. Eagar,
"Metal vapours in gas tungsten arcs: Part I.
Spectroscopy and monochromatic Photography".
Metallurgical Transactions A 17A (1986), 10, p 1851.

2.21 A. Matsunawa, K. Nishiguchi,
"Arc characteristics in high pressure argon atmospheres".
Conference on Arc Physics and Weld Pool Behaviour, London (1979).

2.22 O.H. Nestor,
"Heat intensity and current density distributions at the anode of high current, inert gas arcs".
Journal of Applied Physics 33 (1962), 5, p 1638.

2.23 N.S. Tsai, T.W. Eagar,
"Distribution of the heat and current fluxes in gas tungsten arcs".
Metallurgical Transactions B 16B (1985), 12, p 841.

2.24 A.E. Guile,
"Processes at arc cathode roots on non refractory metals having films of their own oxide".
Conference on Arc Physics and Weld Pool Behaviour, London (1979).

2.25 M. Ushio, A.A. Sadek, F. Matsuda,
"GTA electrode temperature measurement and its related phenomena".
IIW DOC 212-733-89 (1989).

2.26 K.C. Hsu, K. Etemadi, E. Pfender,
"Two-temperature modelling of the free-burning, high-intensity arc".
Journal of Applied Physics 54 (1983), 8, p 4359.

2.27 P. Kovitya, L.E. Cram,
"A two-dimensional model of gas-tungsten welding arcs".
Welding Journal 67 (1986), 12, p 34.

2.28 M.B.C. Quigley, P.H. Richards, D.T. Swift-Hook, A.E.F. Gick,
"Heat flow to the workpiece from a TIG welding arc".
Journal of Physics D: Applied Physics 6 (1973), p 2250.

2.29 M. Ushio, J. Szeleky, C.W. Chang,
"Mathematical modelling of flow field and heat transfer in high-current arc discharge".
Ironmaking and Steelmaking 8 (1981), 6, p 279.

2.30 J.B. Wilkinson, D.R. Milner,
"Heat transfer from arcs".
British Welding Journal 7 (1960), 2, p 115.

2.31 D. Rosenthal,
"Mathematical theory of heat distribution during welding and cutting".
Welding Journal Research Supplement 20 (1941), 5, p 220s.

2.32 R.W. Niles, C.E. Jackson,
"Weld thermal efficiency of the GTAW process".
Welding Journal Research Supplement 54 (1975), 1, p 25s.

2.33 C.R. Heiple, J.R. Roper, R.T. Stagner, R.J. Aden,
"Surface active element effects on the shape of GTA, laser and EB welds".
Welding Journal Research Supplement 62 (1983), 3 , p 72s.

3. Calorimetric Experiments

3.1 Introduction

This chapter deals with calorimetric experiments which have been performed to measure the heat transport to both the anode and cathode in gas tungsten arcs at ambient pressure. Experiments have been carried out to measure the influence of cathode composition, anode composition, arc current, arc length, polarity, shielding gas flow rate and shielding gas composition.

In the first sections of this chapter, the calorimetric setup and procedure will be described. The experiments performed to verify the correct functioning of the calorimeter are also included in this section. Next, the results of the calorimetric experiments will be presented. Some of the results obtained are already discussed in this chapter. These discussions will only be very brief, aiming at a global understanding of the trends in heat flow which have been found. A more thorough discussion will be presented in Chapter 5.

3.2 Experimental setup and procedures

3.2.1 Experimental setup

In order to measure the heat transport during stationary GTA welding, a calorimetric setup was built, as illustrated schematically in Fig. 3.1. The heat entering the workpiece and torch is being carried away by the cooling water and, assuming that this is the only cooling mechanism for both workpiece and torch, water flow rate

and temperature rise are a direct measure of the amount of heat entering the workpiece and the torch. Two separate water ways were used to be able to measure both the anode heat input and the cathode heat input.

The workpiece calorimeter consisted of a circular stainless steel water compartment, on which the workpiece was mounted using four steel clamps. O-rings were used to seal off the water compartment. To maintain symmetry, both water inlet and current supply were located at the calorimeter bottom centre. Two water drains were placed in the vicinity of the water inlet. Thus, the cold water entered the calorimeter right under the arc and was led to the outer regions of the workpiece by a PVC disk. Relatively thick specimens (up to 10 mm) were used in order to simulate the welding situation as closely as possible. Some investigators [3.1] use very thin specimens, which offer the advantage of low thermal inertia. The drawback in using these thin specimens is, that the temperature at the workpiece-arc interface is much

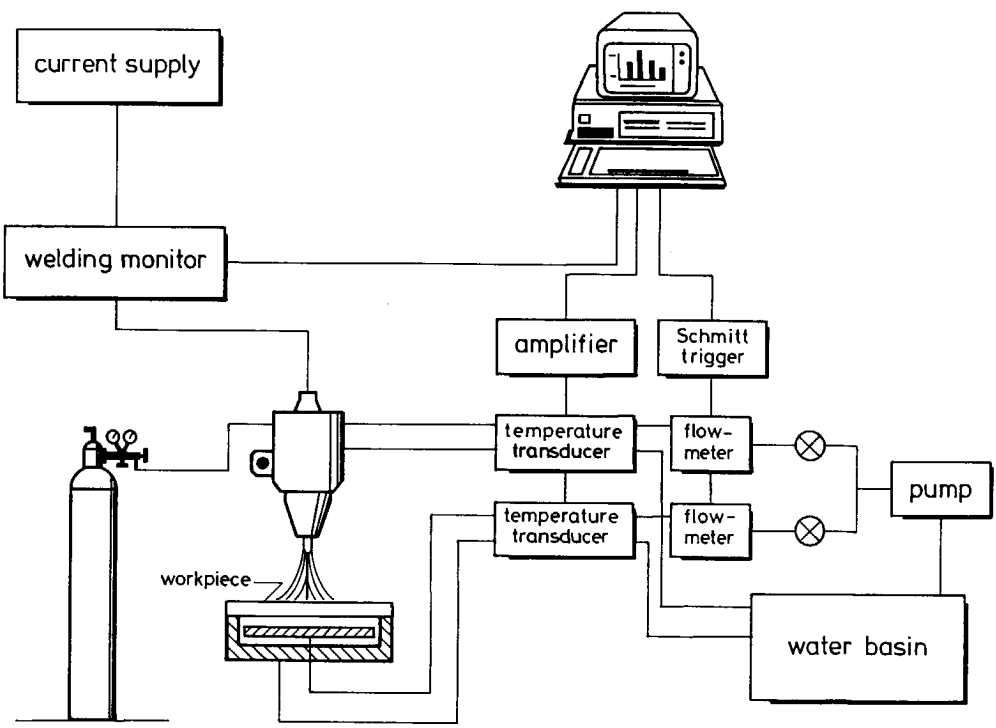

Figure 3.1: Schematic representation of the calorimetric setup.

lower than in a realistic welding situation. When using thick (10 mm) plates, a small molten pool can establish. Various authors indicate, that metal vapours, originating from such a pool, can significantly change the behaviour of the welding arc [3.2]. To avoid unnecessary workpiece preparation, rectangular plates were used rather than circular workpieces.

All experiments were performed using a self made copy of an industrial torch (Smit-Weld). The torch was adapted to be able to withstand high ambient pressures, necessary for the experiments described in Chapter 4. Furthermore, the water cooling of the torch was improved. In view of the pressure demands, a relatively large copper torch body was constructed (Fig. 3.2).

All electrodes used were ground to obtain a top angle of 60°. The electrode compositions and diameters are given in Table 3.1.

Table 3.1: Composition and diameter of the electrodes used.

electrode composition	diameter (mm)	top angle (°)
W	3.2	60
W - 2% ThO_2	3.2	60
W - 2% ThO_2	4.8	60
W - 2% La_2O_3	3.2	60
W - 2% Y_2O_3	3.2	60

The arc current was supplied by an ESAB DTA 300 current supply unit, which proved to possess excellent stability. The Open Circuit Voltage (OCV) of this current supply was 51 V. The current entered the workpiece near the water inlet positioned at the centre of the calorimeter bottom part. This symmetrical positioning prevented magnetically induced arc wander.

The arc current was led through a shunt. The output of this shunt and the arc voltage were subsequently passed on to a welding monitor, an electronic device which serves various purposes. Firstly, it serves as a complete galvanic separation between the welding setup and the measuring devices by means of opto-couplers. Secondly, it provides filtering of high-frequency noise and finally, it serves as an amplifier which was used to obtain a 10 mV/V and 1 mV/A input signal for the

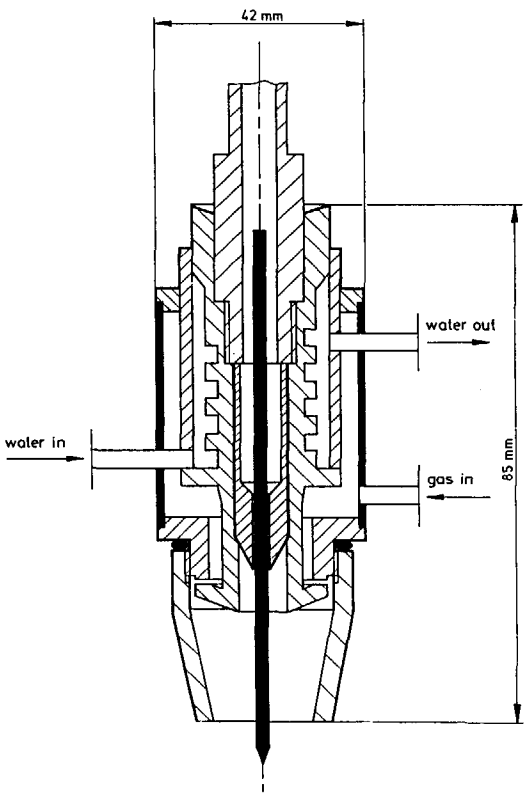

Figure 3.2 : Schematic representation of the welding torch used.

analog-digital convertor in the computer.

Water was pumped through the calorimeters by an AC electric pump. Maximum throughput was found to be about 2 l/min. The water was contained in a basin which could hold up to 150 liters. This basin was employed to ensure a constant water inlet temperature during the experiment. The heat capacity of the water in the basin was about 4.2·150=630 kJ/K. Welding during long times (>1 hour) with a net heat flow to the anode and cathode of, for instance, 1 kW will lead to an increase in water temperature of 5 to 6°C. To adjust for this temperature rise, the water was partially refreshed during the longer lasting experiments so that the total temperature rise during any experiment did not exceed 3°C.

Water flow was measured using Brooks Oval Flow meters. These flow meters have a typical accuracy of 1%, which was confirmed during calibration measurements. The passive output of these flow meters consisted of a microswitch which opens and closes with each revolution of the ovals. A 15 V DC Voltage Supply Unit and a

Schmitt-trigger were employed to obtain a one cycle per revolution signal. These cycles were then counted by the computer. Water flow was regulated by means of needle valves placed in the inlet water ways. The flow meters were located immediately after these needle valves.

The temperature of the cooling water was measured using AD 592-C temperature transducers. These temperature transducers have a typical accuracy and long-term stability of 0.1°C. The current output of 1 mA/K was transformed into a voltage output of 10 mV/K which could be used as the input signal for the analog-digital convertor in the computer. A differential scheme was used to obtain directly the temperature difference between water inlet temperature and water outlet temperature.

Gas was supplied either directly from the pressure regulator on the gas container, or through a self designed gas mixing setup when performing experiments with gas mixtures. Gas flow was measured by gas flow meters having an accuracy of 0.1 l/min.

Workpiece materials used were copper, tungsten, iron and Fe510 steel, in the form of plates. The chemical composition of these materials is given in Table 3.2. In the case of iron and Fe510 workpieces, plates of dimensions 400·160·10 mm were used. The copper plate had dimensions of 200·160·10 mm and the tungsten used consisted of a disk of diameter 45 mm and thickness 10 mm which was shrunk in a brass plate. This brass had little or no influence on the behaviour of the calorimeter, since brass has similar thermal properties as tungsten.

An Olivetti PC, fitted with a Tecmar Labmaster board, was used to collect the information obtained from the welding monitor, the water flow meters and the temperature measuring devices. To eliminate electrical noise from the 220 V current supply, an isolating transformer was used. A pascal/assembler program was written to obtain the necessary data from the Labmaster board and to write them to disk. The Labmaster board had a maximum conversion rate of 40 kHz at a 12 bits accuracy. The 12 bits accuracy leads to a digitalization error of $(\frac{1}{2})^{12}$=0.025%. In calibration experiments, the accuracy of the Labmaster was indeed found to be 0.2 mV on a full scale of 1 V.

The maximum conversion rate of the analog - digital conversion board was not reached, as the massive amount of data thus obtained could never have been stored.

Table 3.2: Composition of the workpiece materials used.

workpiece		Cu	W	Fe	Fe 510
element					
Cu	(wt%)	balance	<0.01	0.007	0.17
W	(wt%)	-	balance	-	-
Fe	(wt%)	<0.01	<0.01	balance	balance
C	(wt%)	-	-	0.02	0.17
Mn	(wt%)	-	-	0.04	1.13
Si	(wt%)	-	-	0.07	0.26
P	(wt%)	-	-	-	-
S	(wt%)	-	-	-	-
Ti	(wt%)	-	-	-	0.017
V	(wt%)	-	-	-	<0.01
Cr	(wt%)	<0.01	<0.01	0.03	0.24
Ni	(wt%)	-	-	0.04	0.31
Zn	(wt%)	-	<0.01	-	-

The program was written in such a way, that the data, obtained over a period of five seconds, were averaged before they were written to disk. This kept the data files in a manageable form. Moreover, averaging the obtained data (temperature, voltage and current) greatly reduced scatter in these data.

Every data point written to disk is the average of about 30000 samples. A typical data file thus consisted of about 500 to 1000 data points and was 25 to 50 kBytes in size. Averaging the collected data proved to enhance the reliability and significantly reduced the effects of electrical noise.

3.2.2 *Measuring method and experimental procedure*

To measure the heat flow to the workpiece and electrode using the calorimetric setup just described, two methods can be employed.

- When thermal equilibrium of the calorimeter is reached, the heat flow to the workpiece and the electrode can be calculated from the specific heat of the water, the rise in water temperature ΔT and the mass flow rate of water $\dot{m}$ by using the equation

$$Q = 4.18\ \Delta T\ \dot{m} \tag{3.1}$$

- It is also possible to integrate the heat flow to the workpiece and the electrode over time during the entire experimental measuring cycle. The heating up and cooling down period of the calorimeter have to be included in this integration. As the calorimeter cools very slowly, the measurement has to be extended long after the arc is extinguished. In fact, the experiment must go on until the original thermal equilibrium is reached again. Thus, an integral of both gross arc power and net heat input can be obtained.

For purpose of comparison, several experiments were performed in which both methods were used to obtain anodic efficiency and cathodic efficiency. The anodic efficiency η_a and the cathodic efficiency η_c are defined as

$$\eta_a = \frac{Q_a}{V_t I} \quad ; \quad \eta_c = \frac{Q_c}{V_t I} \tag{3.2}$$

in which Q_a, Q_c, V_t and I represent the anode heat input, cathode heat input, arc voltage and arc current respectively. The results obtained show excellent agreement (Table 3.3). Differences between the results obtained with these two methods are smaller than 0.4% and 0.1% for the anodic efficiency and cathodic efficiency respectively.

The disadvantage of the second method is, that an experiment can take more than one hour to complete. As this does not contribute to the accuracy of the experiments, it was preferred to use the first method and perform several measurements in a single run. In such experiments, thermal equilibrium was awaited after the first set of welding parameters chosen. When thermal equilibrium was reached, a measurement was made. The welding parameters were then changed and another measurement was

Table 3.3: Comparison between efficiencies obtained using two different methods.
Copper anode, 3.2 mm W-ThO_2 electrode, 3 mm arc length in argon shielding gas.

	Thermal equilibrium		Integrated heat flow	
I (A)	η_a (%)	η_c (%)	η_a (%)	η_c (%)
50.1	71.8	6.3	72.4	6.3
101.0	76.6	3.5	76.2	3.5
152.4	76.3	3.3	76.4	3.3
203.2	77.3	2.9	77.4	2.8
255.5	77.5	3.1	77.9	3.0

made when the new thermal equilibrium was reached. Unless otherwise stated, the results presented in this chapter have been obtained in this way.

The obvious drawback of this procedure is that changes in the composition or geometry of the workpiece and electrode, taking place in the first stages of the experiment, will affect later measurements. The composition of the electrode, for instance, might change due to evaporation of oxides, whereas its geometry might alter due to erosion of the electrode tip. Similar effects may occur at the anodic workpiece.

Two sets of experiments were performed to examine the possible influence of electrode and workpiece degradation on the heat flow to anode and cathode. In an experimental setup with a copper anode, tungsten-thoria electrode and 3 mm arc length in argon shielding gas, the heat flow to the anode and cathode was measured using two different methods. Heat flow was measured as a function of arc current.

The first set of experiments consisted of separate measurements, in which the arc was shut off after each measurement and electrode and workpiece preparation was performed prior to each experiment. The second set of data was obtained by increasing arc current in steps of 50 A from 50 A up to 250 A in a continuous experimental run. At each arc current, equilibrium was awaited before water temperature and water flow rate were measured. The results of both experimental series are given in Table 3.4 and show that the method chosen does not influence the

outcome of the experiments beyond the normal reproducibility of the arc process itself. Apparently, changes in composition and appearance of the workpiece and electrode at low arc current do not influence the heat flow processes taking place at higher arc current. This implies that electrode erosion at low arc current does not affect arc behaviour at high arc current.

The experiments described in this chapter were always performed in such a way, that heat input to the anode and cathode increased during the experiment. When measuring the influence of arc current or arc length, the experiment was started at low arc current or arc length. When measuring the influence of shielding gas composition (in argon-helium mixtures), the experiment was started with a pure argon shielding gas flow, and helium content was increased during the experiment.

Arc ignition was accomplished by short-circuiting with a carbon stick electrode at low arc current. The short circuit was made at a relatively large distance from the electrode tip, so that no degradation of the electrode took place.

Table 3.4: Comparison between efficiencies obtained in separate experimental runs and efficiencies obtained in a continuous experimental run. Copper anode, 3.2 mm W-ThO_2 electrode, 3 mm arc length in argon shielding gas.

Separate runs			Continuous run		
I (A)	η_a (%)	η_c (%)	I (A)	η_a (%)	η_c (%)
50.1	71.8	6.3	50.2	70.1	5.8
101.0	76.6	3.5	100.0	75.8	4.1
152.4	76.3	3.3	150.8	78.9	3.5
203.2	77.3	2.9	201.2	80.3	3.5
255.5	77.5	3.1	251.2	79.4	3.1

3.2.3 *Thermal inertia of the calorimeter*

In order to measure heat transport properly, it is essential that thermal equilibrium is reached. The thermal inertia of the calorimeter thus becomes an important factor. Figure 3.3 shows the typical response of the workpiece calorimeter and torch calorimeter to an instantaneous change in arc current of 50 A.

Assuming an exponential relationship between the temperature increase of the calorimeter cooling water and time, it can be concluded that the time constants governing the response of the workpiece calorimeter and torch calorimeter are about 50 and 100 s respectively. Using these time constants, the minimum time lapse to obtain valid heat input values would be 500 s, in which case the equilibrium will be approached to within 0.005% and 0.7% respectively.

It must be noted, that the experimental parameters used in obtaining Fig. 3.3 represent one of the worst cases encountered during the actual experiments. Experiments with a copper workpiece or a workpiece of reduced thickness will, for instance, result in a considerable decrease of the thermal inertia of the calorimetric setup.

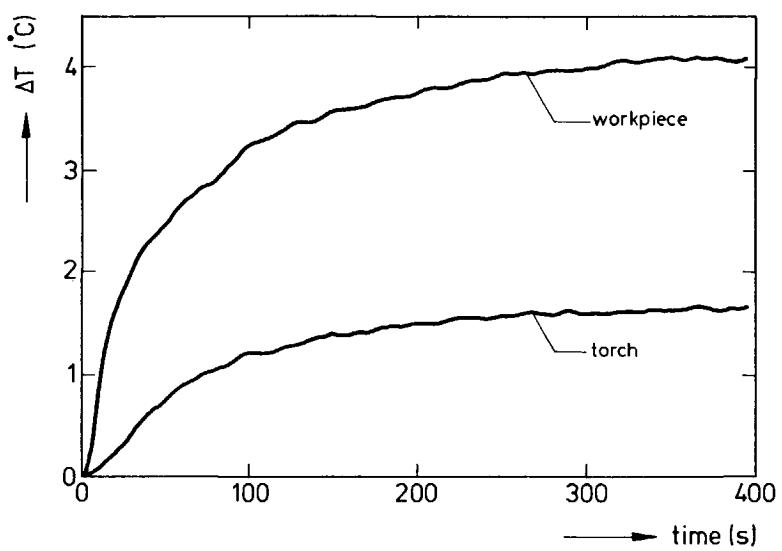

Figure 3.3 : Typical response of the calorimetric setup.

To obtain valid results, thermal equilibrium of the calorimeters was awaited for 500 s in all experiments.

3.2.4 *Influence of water flow rate on measured efficiencies*

Experiments were performed to assess the influence of the water flow rate in the anode calorimeter and cathode calorimeter on the measured heat input. The results of these experiments are presented in Fig. 3.4. The measured anodic efficiency is shown to be strongly dependent on the employed water flow rate through the workpiece calorimeter. Below a water flow rate of 15 ml/s, the measured efficiency decreased significantly from an otherwise constant value of about 75%. Furthermore, it was noticed that when the water flow rate was decreased below 15 ml/s, the temperature at the outer edges of the workpiece increased to well over 50°C and thermal equilibrium could not be reached within reasonable time.

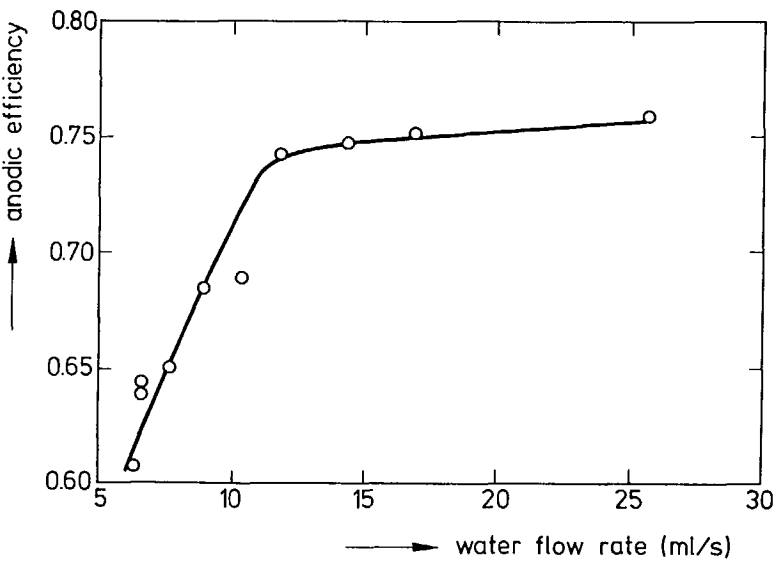

Figure 3.4 : Anodic efficiency as a function of the water flow rate through the workpiece calorimeter.

It is concluded that below a certain water flow rate, the water in the calorimeter is heated to boiling temperature and is subsequently vaporized. Thus, the heat transport coefficient between workpiece and cooling water decreases abruptly due to the presence of a water vapour layer just beneath the workpiece bottom surface and proper functioning of the calorimeter is no longer guaranteed.

A similar effect was not found in the case of the torch calorimeter (see Fig. 3.5). This might be caused by the relatively large cooling surface area of the torch and the low cathode heat input. Therefore it can be concluded that within the range of water flow rates employed, no water vapour is formed in the cooling circuit of the torch.

In subsequent experiments, the water flow rate was maintained above 18 ml/s and 3 ml/s for the workpiece and the torch respectively.

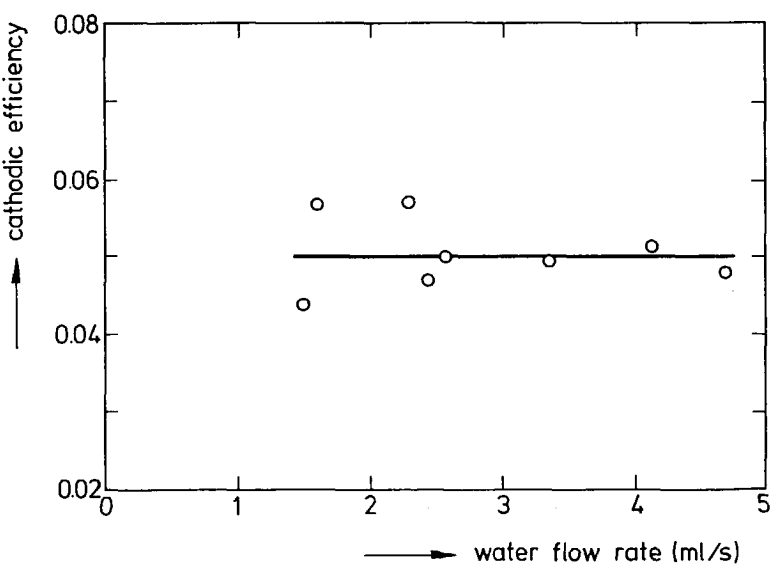

Figure 3.5 : Cathodic efficiency as a function of the water flow rate through the torch calorimeter.

3.2.5 *Reproducibility and accuracy*

There are several sources of error and bad reproducibility in measuring the heat flow during arc welding. The most important error sources are :

- The inaccuracy of the measurement of arc current, arc voltage, water temperature and water flow rate. This inaccuracy is known to be very small (see § 3.2.1).
- Limited reproducibility of cathode and anode surface conditions. Deviations in the electrode top angle and the electrode grinding direction, for instance, can significantly alter the arc behaviour [3.3]. Surface contamination of anode or cathode can also be of importance. In this work, the top angle of the electrode was ground to 60°±5°. Both the electrode and the workpiece were ground shortly before the experiment was carried out.
- Limited accuracy of the preset arc length. Arc length was preset using a screw, with an accuracy of 0.05 mm. The thermal expansion of the electrode during arcing can account for a decrease in arc length of up to 0.1 mm. Furthermore, electrode erosion will increase arc length. At an arc column field strength of 1 V/mm, a change in arc length of 0.1 mm will result in a change in arc voltage of 0.1 V. This is low, compared to the total arc voltage of about 10 V.
- Electrical noise from outside sources. This degrades both the performance of the temperature measuring transducers and the functioning of the analog-digital convertor. As the data points were averaged over 30,000 samples, electrical noise was not a problem during experiments.
- Intrinsic instabilities of the arc discharge itself are also a source of noise. As heat flows were all measured over a period of one minute at least, this did not pose serious problems.

All in all, the reproducibility and accuracy of the experiments was found to be satisfactory. For instance, in a typical experiment carried out with an arc current of 100 A and an arc length of 0.5 to 7 mm in argon shielding gas, arc voltage was found to be reproducible to within 0.2 V. Anode heat input and cathode heat input were reproducible to within 20 W and 5 W respectively and differences in the calculated efficiencies did not exceed 0.02 and 0.005 respectively.

The only significant systematic error in the measurement of the anode heat input and cathode heat input is due to heat losses to the surroundings. The radiative, conductive and convective heat losses from the calorimeters to the surroundings should be so small that the effect on the heat flow measurement can be neglected. Heat losses from the workpiece calorimeter and electrode calorimeter were calculated to be small indeed (see Appendix A). For instance, heat losses from the workpiece were calculated to be smaller than 3% of the total workpiece heat input.

To validate the employed calorimetric method and to check to what extent heat drains such as those mentioned above affect the heat flow measurements, an experiment was performed in which all three basic heat flows were measured (to the workpiece, to the electrode, to the surroundings). The setup for this experiment is given schematically in Fig. 3.6. A 3.2 mm W-ThO_2 electrode was used at a fixed arc length of 3 mm and a 10 l/min argon shielding gas flow.

At an arc current of 100 A, it was found that the sum of the three heat flows mentioned approximates the arc power to within 3%. Thus it can be concluded that the results obtained with the calorimetric setup have an acceptable accuracy.

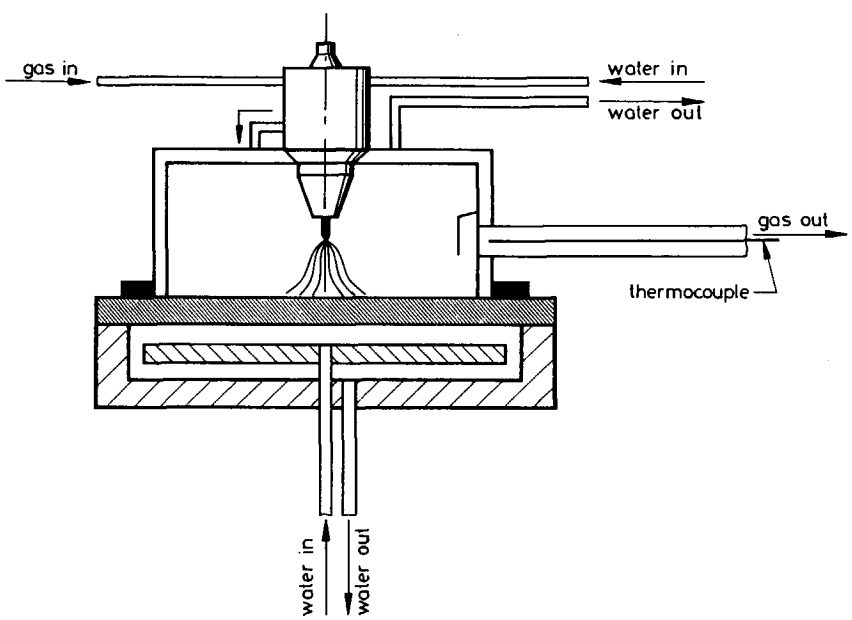

Figure 3.6 : Schematic illustration of the experimental setup to measure all three basic heat flows.

In these experiments, the anodic efficiency was found to be a few percent higher than in 'normal' calorimetric experiments. This is obviously due to the increased convective contribution of the hot gas, present just above the workpiece. The gas temperature measured was in the order of 100 to 150°C. The outer extremities of the workpiece were much hotter in these experiments, giving rise to a heat loss which is not accounted for.

3.3 Results and discussion

In this section the results of the calorimetric experiments are presented. The arc voltage V_t, anode heat input Q_a and cathode heat input Q_c were measured as a function of the cathode conditions and anode conditions, arc current, arc length, polarity, shielding gas flow rate and shielding gas composition. From the data obtained, the anodic efficiency η_a and cathodic efficiency η_c were calculated using equation (3.2). Unless otherwise stated, experiments were performed with tungsten-thoria electrodes of diameter 3.2 mm and a top angle of 60° at an arc length of 3 mm, an arc current of 100 A in an argon shielding gas flow of 10 l/min on a copper anode. These standard conditions are given as a reference in Table 3.5.

Table 3.5: The standard experimental conditions.

electrode composition	tungsten - 2% thoria
electrode diameter	3.2 mm
electrode top angle	60°
workpiece material	copper
workpiece dimensions	plate 160·200·10 mm
arc current	100 A
polarity	straight (electrode negative)
arc length	3 mm
shielding gas composition	pure argon
shielding gas flow rate	10 l/min

3.3.1 *Influence of cathode conditions*

In order to examine the influence of cathode conditions on heat transport, three sets of experiments were performed. Firstly, the influence of the cathode diameter on arc voltage and the heat flow to anode and cathode was examined. Secondly, experiments were done to investigate whether the grinding direction of the electrode did have a noticeable effect on cathode heat input. Finally, the influence of cathode composition was examined using electrodes containing different kinds of oxide additions.

Influence of electrode diameter

Experiments were performed with tungsten-thoria electrodes of diameter 3.2 and 4.8 mm for an arc current of 50 to 250 A on an iron workpiece. Electrodes with smaller diameters were not used, since these would suffer too much erosion at high arc current. The arc voltage, anode heat input, cathode heat input, anodic efficiency and cathodic efficiency of both electrodes are given in Table 3.6. The table shows that arc voltage, heat input and efficiency are affected by electrode diameter. This was expected, since the better cooling of the electrode of 4.8 mm diameter will decrease the temperature at the electrode tip, which in turn decreases electron thermal emission. Thus, the cathode voltage drop is expected to be affected. However, because of the inconsistency in the results obtained, no clear conclusions can be drawn from these data.

Influence of cathode surface conditions

Experiments were performed with two tungsten-thoria electrodes, each ground in a distinctly different way to obtain a 60° top angle. The first electrode was ground radially, the second electrode axially. Both electrodes were 3.2 mm in diameter. Although some evidence exists in literature, that electrodes ground axially suffer less severe erosion than electrodes ground otherwise, the results obtained indicate that the grinding direction of the electrodes do not have any significant effect on the arc voltage, anode heat input, cathode heat input, anodic efficiency or cathodic efficiency (see Table 3.7). In subsequent experiments, electrodes were always ground radially.

influenced by cathode composition. The extrapolated zero arc length voltage is 9.5, 8.0, 8.2 and 8.0 V for the pure tungsten, tungsten-thoria, tungsten-yttria and tungsten-lanthania electrodes respectively. If it is assumed that the anode voltage drop is not influenced by the change in cathode composition and that the zero arc length voltage indeed represents the sum of the anode voltage drop and the cathode voltage drop, the change in the extrapolated zero arc length voltage is caused by a change in cathode voltage drop. Therefore, the cathode voltage drop in front of the tungsten electrode is about 1.5 V higher than the cathode voltage drop when using electrodes containing oxide additions.

The cathode heat input is depicted in Fig. 3.8 as a function of arc length. This figure shows that the oxide-doped electrodes consume less heat than the pure tungsten electrode. This is due to the lower work function of the oxide containing electrodes. In Fig. 3.9 the cathodic efficiency of the oxide containing electrodes and the cathodic efficiency of the pure tungsten electrode are plotted as a function of arc length. The figure shows that the cathodic efficiency of oxide-doped-electrodes is about 0.02 lower than the cathodic efficiency of a pure tungsten electrode. It must be noted, that all oxide containing electrodes show an essentially similar behaviour in terms of arc voltage, cathode heat input and cathodic efficiency.

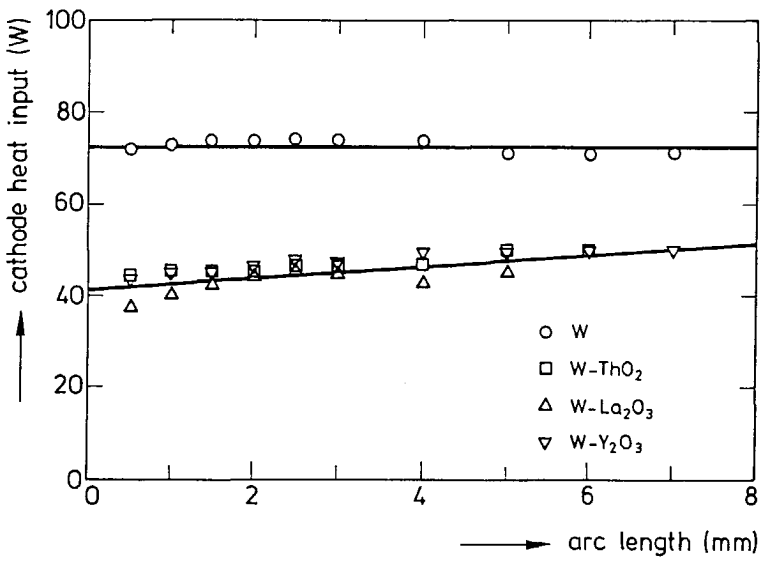

Figure 3.8 : Influence of electrode composition and arc length on cathode heat input. Tungsten anode, 3.2 mm electrode, 100 A arc current in argon shielding gas.

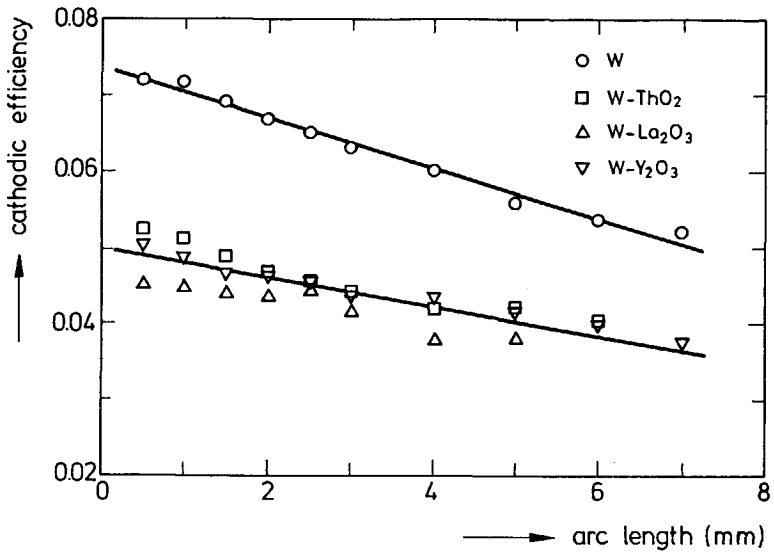

Figure 3.9 : Influence of electrode composition and arc length on cathodic efficiency. Tungsten anode, 3.2 mm electrode, 100 A arc current in argon shielding gas.

Although cathode composition was not expected to influence the anode heat input, heat flow to the tungsten workpiece was found to be higher in the case of pure tungsten electrodes (about 10%). Due to the increased arc power, however, the anodic efficiency when using tungsten electrodes is lower by about 0.04.

In a second series of experiments, the heat flow to a pure tungsten electrode and a tungsten electrode containing 2% ThO_2 was measured as a function of arc current. Use was made of a tungsten workpiece. These experiments were performed to assess whether the favourable behaviour of oxide-doped electrodes was in some way dependent on arc current. It was thought, that at high arc current and the associated high electrode temperature, oxides might be evaporated, thus cancelling their favourable influence on the electron thermal emission at the cathode.

The heat flow to the tungsten and the tungsten-thoria electrode is plotted as a function of arc current in Fig 3.10. As was also found in the experiments with variable arc length (Fig. 3.8), the heat flow to the tungsten electrode is considerably higher than the heat flow to the tungsten-thoria electrode. Again, cathodic efficiency is highest for tungsten electrodes. Tungsten electrodes have a cathodic efficiency which

is 0.01 to 0.02 higher than the cathodic efficiency of oxide-doped electrodes. The difference in cathodic efficiency, however, decreases with increasing arc current.

As in the experiments with variable arc length, the anode heat input is higher when using pure tungsten electrodes. The anodic efficiency when using pure tungsten electrodes, however, is about 0.02 to 0.05 lower than the efficiency found when employing tungsten-thoria electrodes. The lower anodic efficiency is clearly caused by the higher arc voltage when using pure tungsten electrodes, resulting in a higher arc power.

In order to examine the erosion behaviour of the electrodes further, EPMA experiments were performed on tungsten-thoria electrodes after welding for one hour at various arc currents. The results of these experiments show that the tip of the electrode is completely depleted of thoria after welding at 250 A for 1 hour (see Fig. 3.11). At an arc current of 100 A, the thoria depletion zone was about 10 times smaller in depth. This indicates that the beneficial effect of thoria vanishes when welding at high arc current. The depletion of thoria at higher arc current could thus

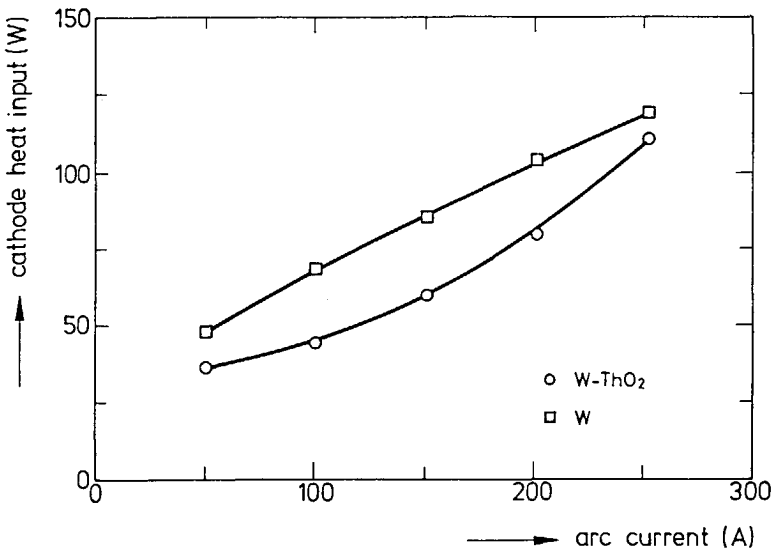

Figure 3.10 : Influence of electrode composition and arc current on cathode heat input. Tungsten anode, 3.2 mm electrode, 3 mm arc length in argon shielding gas.

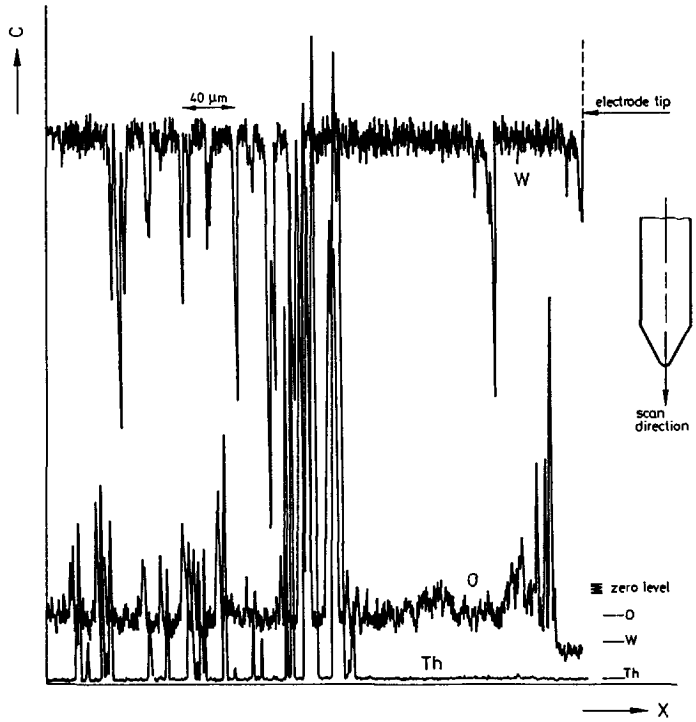

Figure 3.11 : EPMA analysis of the tip of a 3.2 mm W-ThO_2 electrode after 1 hour of welding at 250 A at an arc length of 3 mm in argon shielding gas.

explain the decreased difference in cathode heat input at increased arc current, as shown in Fig. 3.10.

3.3.2 *Influence of anode conditions*

In this section, experiments are described which have been carried out on workpieces of copper, tungsten, iron and mild steel (Fe 510). The effect of workpiece composition on arc voltage and heat flow was measured as a function of arc length over an arc length range of 0.5 to 7 mm. In a second set of experiments, attention was paid to the possible effect of the presence of molten anode material on anode heat transport. Metal vapours can significantly alter the behaviour of the arc. Due to the low ionization potential of most metals, ionization can take place at a relatively low plasma temperature. This means that the presence of metal vapours in the arc will

result in a decrease in arc temperature. Melting of the anode material took place when iron and steel workpieces were used. By reducing the workpiece thickness of these materials, the cooling of the anode was improved, so that melting no longer took place.

Influence of anode composition

Experiments were performed using workpieces of copper, iron, steel and tungsten. The heat flow to these anodes was measured as a function of arc length. Due to the presence of molten anode material, the minimum arc length in experiments on iron and steel workpieces was 1 mm.

The obtained arc voltage-arc length curves for the four anode materials are shown in Fig. 3.12. The figure shows, that arc voltage is only slightly influenced by workpiece composition and that copper workpieces show higher arc voltage than workpieces of steel, iron and tungsten. This might be a consequence of the absence of molten or vaporized material, or of the lower surface temperature of the copper anode.

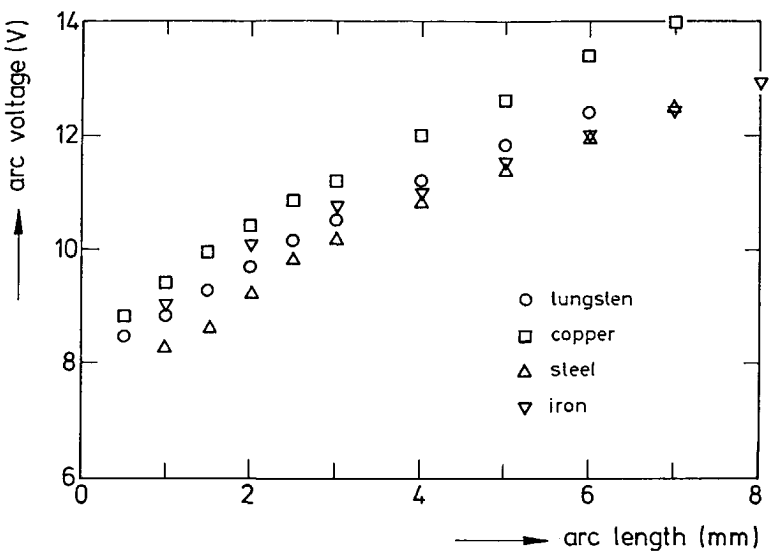

Figure 3.12 : Arc voltage versus arc length for various anode materials.
3.2 mm W-ThO_2 electrode, 100 A arc current in argon shielding gas.

The anode heat input shows a similar dependence on arc length as the arc voltage shown in Fig. 3.12. This results in anodic efficiency to be virtually independent of anode composition (Fig. 3.13).

The cathode heat input and the cathodic efficiency were both found to be independent of the anode material.

Influence of the presence of molten anode material

Complementary to the measurements just described, experiments were performed to assess the influence of anode melting on heat transport. During the previous experiments, the copper and tungsten workpieces did not show any visible melting, whereas in the case of workpieces of iron and mild steel, small molten pools were formed. To study the effect of anode melting, iron workpieces of three thicknesses were used (2, 5 and 10 mm). The workpieces of 2 and 5 mm thickness did not show any melting at an arc current of 100 A, whereas small molten pools were formed when using a workpiece of 10 mm thickness.

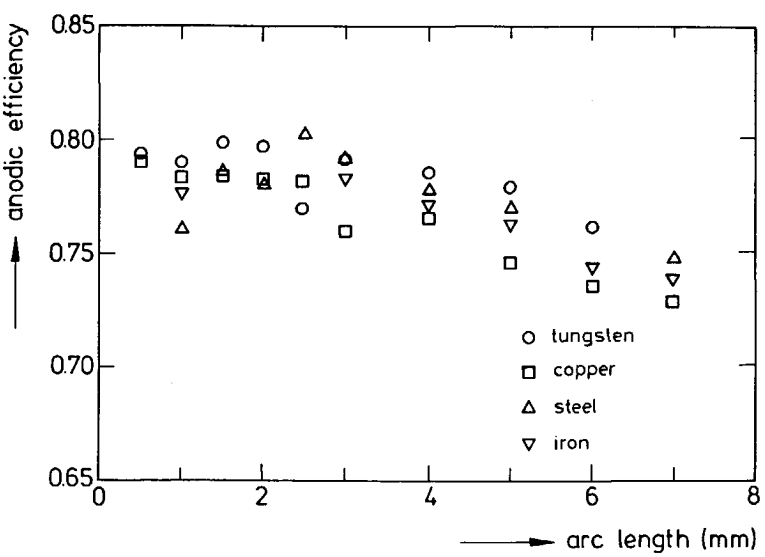

Figure 3.13 : Anodic efficiency versus arc length for various anode materials. 3.2 mm W-ThO_2 electrode, 100 A arc current in argon shielding gas.

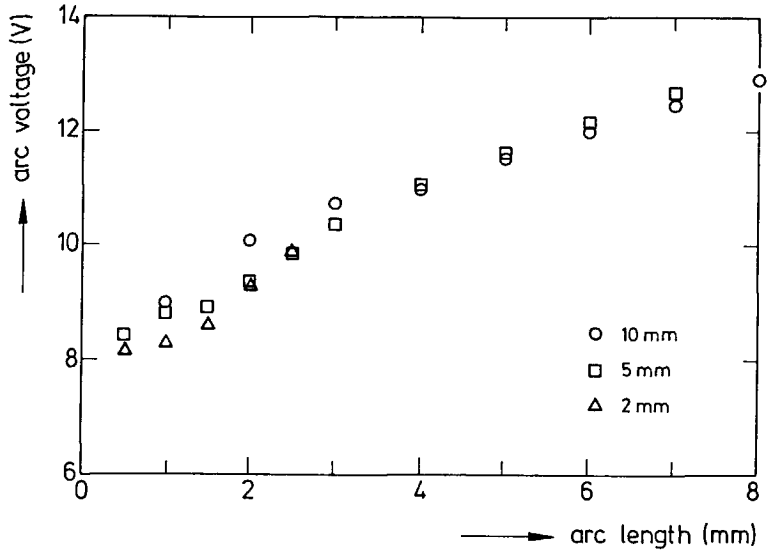

Figure 3.14 : Influence of workpiece thickness on arc voltage-arc length curves. Iron anode, 3.2 mm W-ThO_2 electrode, 100 A arc current in argon shielding gas.

The arc voltage and the heat flow to these three iron workpieces was measured as a function of arc length. The arc voltages measured are presented in Fig. 3.14. Comparing the arc voltage-arc length curves obtained, it becomes clear that arc voltage is hardly influenced by the presence of molten anode material. The anode heat input shows a similar dependence on arc length as the arc voltage shown in Fig. 3.14. The anodic efficiencies of the three workpieces are given in Fig. 3.15 as a function of arc length.

As expected, the cathode heat flow was found not to be affected by the melting of the workpiece.

From the arc voltage-arc length plots obtained in the experiments, the arc column field strength and the zero arc length voltage were calculated. The results are listed in Table 3.8. The table shows that the arc column field strength and the zero arc length voltage, representing the sum of cathode voltage drop and anode voltage drop, are only slightly influenced by anode composition or by melting of the anode material.

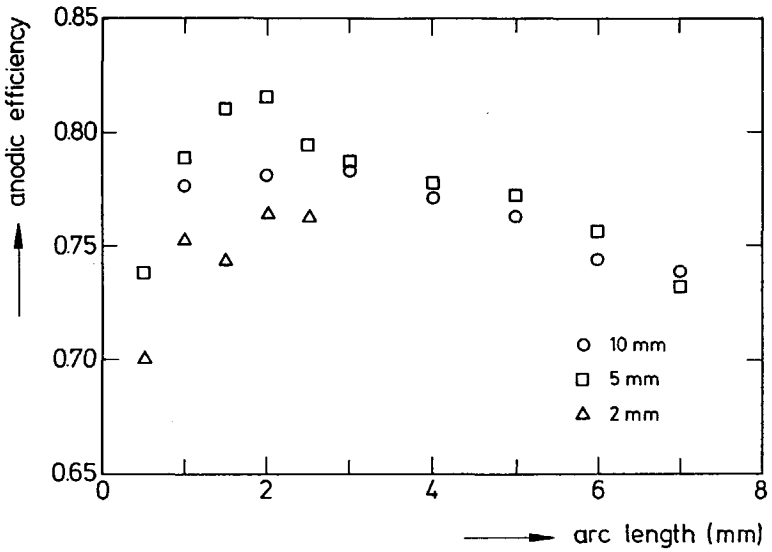

Figure 3.15 : Influence of workpiece thickness and arc length on anodic efficiency. Iron anode, 3.2 mm W-ThO_2 electrode, 100 A arc current in argon shielding gas.

Table 3.8: Zero arc length voltage and arc column field strength for various anode materials.
3.2 mm W-ThO_2 electrode, 100 A arc current in argon shielding gas.

anode material	anode thickness (mm)	zero arc length voltage (V)	field strength (V/mm)
Copper	10	8.5	0.95
Tungsten	10	8.0	0.83
Steel	10	7.2	1.00
Iron	10	8.2	0.88
Iron	5	8.0	0.76
Iron	2	7.5	0.89

3.3.3 *Influence of arc current*

The influence of arc current on arc voltage and on the heat flow to the workpiece and electrode was first investigated in the region of 50 to 250 A. Experiments were performed with 3.2 mm tungsten-thoria electrodes on iron workpieces in argon shielding gas.

The arc voltage-arc current characteristic of a 3 mm arc in argon is given in Fig. 3.16. In this figure, the arc voltage is shown to rise slowly with arc current. In Fig. 3.17 the measured arc power, anode heat input and cathode heat input are given as a function of arc current. Almost straight lines were found, suggesting a linear relationship between arc current and arc power, anode heat input and cathode heat input. It is obvious that the heat flow to the workpiece and electrode increases with increasing arc current. The fact that there is a linear correlation can be explained by the approximating heat transport equations given in Chapter 2. As most of the anode heat sources and cathode heat sources in these equations show a direct proportionality between heat flow and arc current, a linear dependence is to be expected.

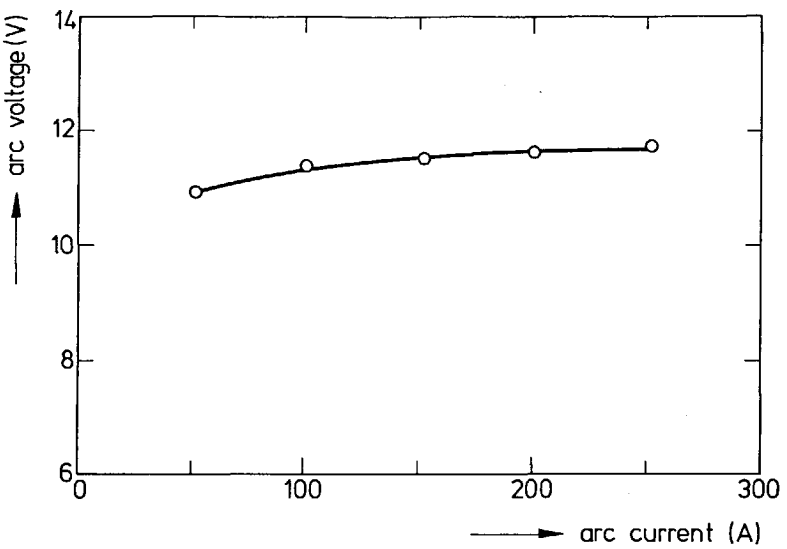

Figure 3.16 : Arc voltage as a function of arc current.
Iron anode, 3.2 mm W-ThO_2 electrode, 3 mm arc length in argon shielding gas.

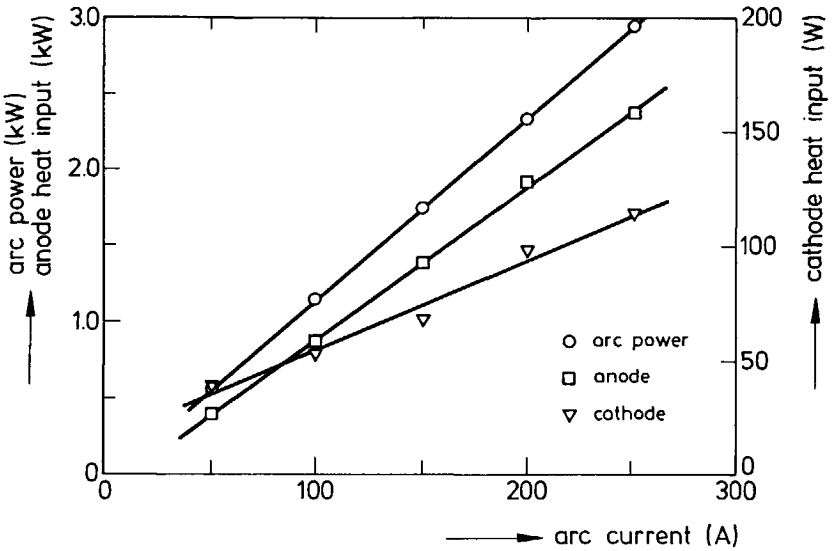

Figure 3.17 : Arc power, anode heat input and cathode heat input as a function of arc current.
Iron anode, 3.2 mm W-ThO_2 electrode, 3 mm arc length in argon shielding gas.

The anodic efficiency and cathodic efficiency are shown as a function of arc current in Fig. 3.18. There is a gradual increase in anodic efficiency from about 70% at 50 A to 75-80% for an arc current of 100 A and above. These findings are in good agreement with findings by other authors [3.4]. The cathodic efficiency decreases from about 7% at 50 A to about 4% at 250 A.

Experiments were also performed on pure copper anodes. The results obtained in these experiments are similar to those just described for iron anodes.

To examine, whether changes in arc mode as described in § 2.2.1 occur when varying arc current, some additional experiments were performed at low arc current. Matsunawa and Nishiguchi [3.5] found the arc mode to change at about 50 A, whereas Goldman [3.6] distinguished five cathode modes with some of the transition currents in the same region.

In the experiments performed, arc current was increased in small steps from 10 A to 100 A. In the case of a transition in arc mode, arc voltage, anode heat input and cathode heat input are expected to show a stepwise response. In Fig. 3.19 the arc

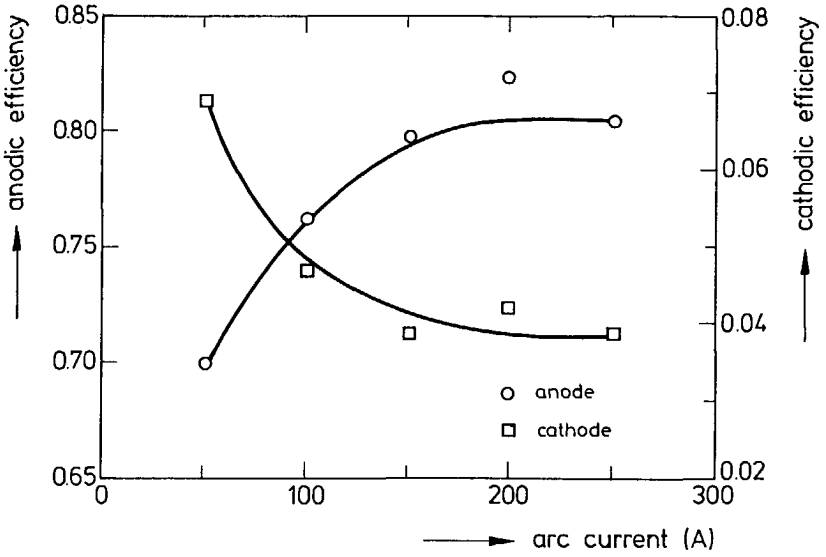

Figure 3.18 : Anodic efficiency and cathodic efficiency as a function of arc current. Iron anode, 3.2 mm W-ThO_2 electrode, 3 mm arc length in argon shielding gas.

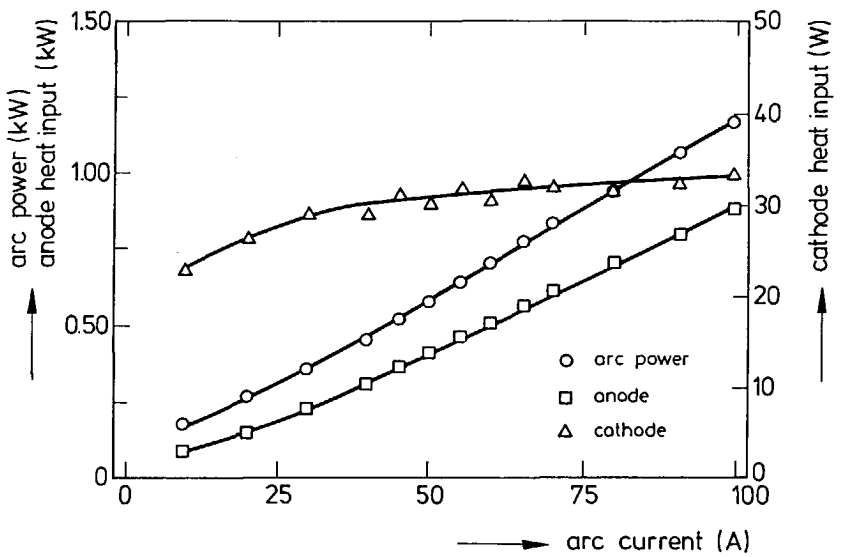

Figure 3.19 : Arc power, anode heat input and cathode heat input at low arc currents. Copper anode, 3.2 mm W-ThO_2 electrode, 3 mm arc length in argon shielding gas.

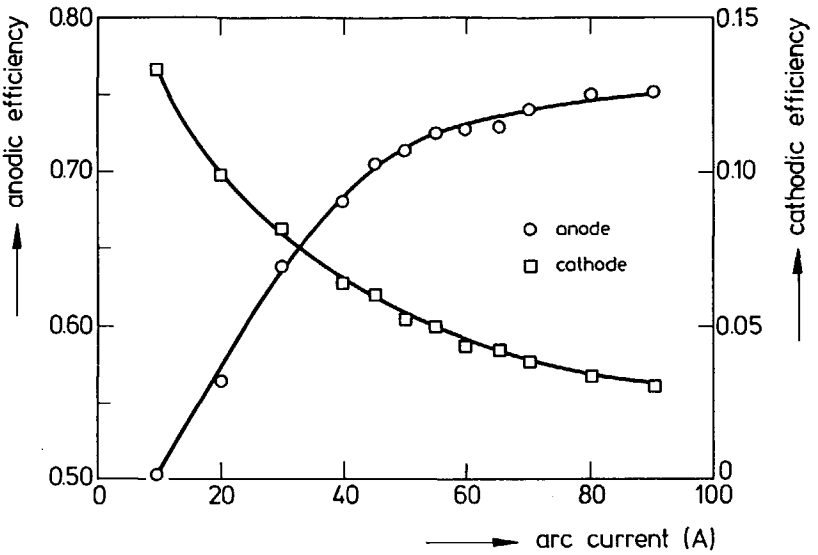

Figure 3.20 : Anodic efficiency and cathodic efficiency for low arc currents. Copper anode, 3.2 mm W-ThO_2 electrode, 3 mm arc length in argon shielding gas.

power, anode heat input and cathode heat input are given as a function of arc current. The figure shows, that no abrupt change in heat flow occurs. Examination of the anodic efficiency and cathodic efficiency, given in Fig. 3.20, leads to the same conclusion. This indicates that under the experimental conditions chosen, there is no evidence of a change in arc mode.

3.3.4 *Influence of arc length*

Experiments were performed with an arc current of 50, 100 and 200 A on a copper workpiece at arc lengths of 0.5 to 7 mm. Typical arc voltage-arc length curves were already shown in Figs. 3.7 and 3.12 in § 3.3.1 and § 3.3.2 respectively.

The arc power and the power entering the anode and cathode at an arc current of 100 A for a copper workpiece are shown in Fig. 3.21. As the theory predicts, the anode heat input increases with arc length. This increase is due to the fact, that part of the heat produced in the arc column is transported to the anode by means of radiation and convection. As arc length increases, more power is dissipated in the arc

column and thus, more of it is transported to the anode. The cathode heat input is virtually independent of arc length. Apparently, radiative and convective heat transport from the arc column to the cathode is negligibly small.

In Fig. 3.22, the anodic efficiency and cathodic efficiency are shown as a function of arc length. Although the anode heat input increases with increasing arc length, the anodic efficiency decreases with increasing arc length. Increasing arc length also results in a decrease of the cathodic efficiency. This leads to the obvious conclusion that more heat is lost in the arc column as arc length is increased. Apparently, only a small part of this extra heat generated is transferred to the anode and cathode.

Experiments were also performed on workpieces of iron, mild steel and tungsten. The results in terms of heat flow and efficiency match the results found when using copper workpieces.

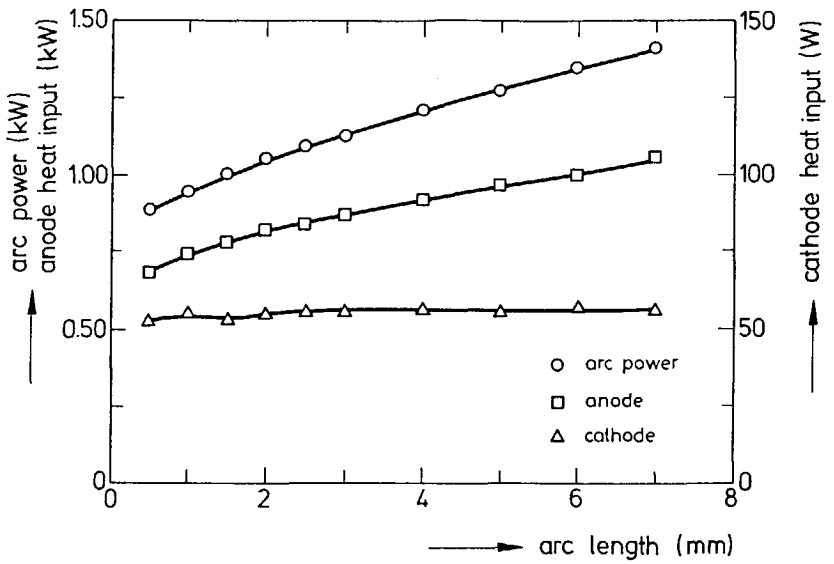

Figure 3.21 : Effect of arc length on arc power, anode heat input and cathode heat input.
Copper anode, 3.2 mm W-ThO_2 electrode, 100 A arc current in argon shielding gas.

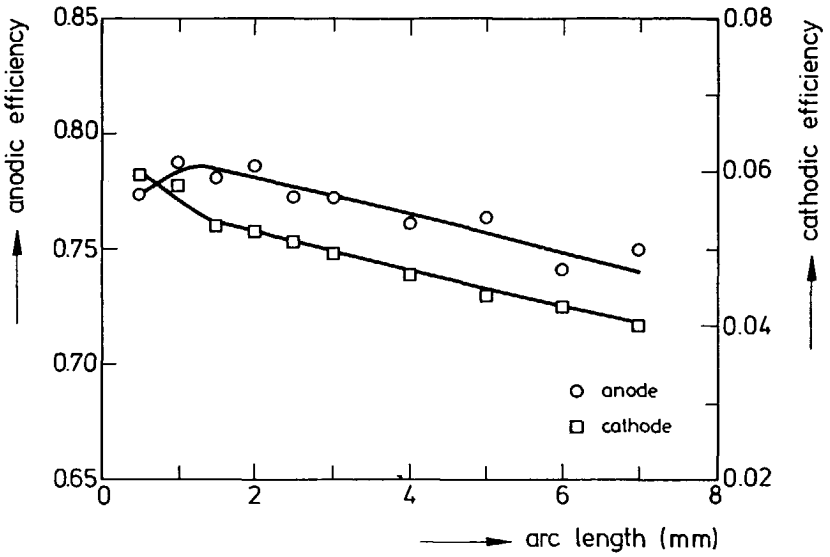

Figure 3.22 : Effect of arc length on anodic efficiency and cathodic efficiency. Copper anode, 3.2 mm W-ThO_2 electrode, 100 A arc current in argon shielding gas.

3.3.5 *Influence of polarity*

In normal (straight polarity) GTA welding, the workpiece is usually held positive. This is advantageous because the workpiece heat input is highest when the workpiece is held positive, whereas the heat input to the electrode is lowest when the electrode is held negative. Thus, electrode erosion is lowest in welding with straight polarity. When welding aluminium, however, alternating current is used to circumvent stability problems arising from the existence of an impenetrable oxide film on the aluminum. In GMA welding, reverse polarity is often used because of the higher melting rate of the electrode, which is used as a filler metal.

In order to examine the influence of polarity on heat flow, an experiment was performed with reverse polarity, i.e. the iron workpiece was used as cathode, whereas the electrode was held positive. The electrode used in the experiments with reverse polarity was a 4.8 mm W-ThO_2 electrode, since a 3.2 mm electrode was found to suffer too much erosion because of the increased heat input. Furthermore, it was

found necessary to restrict the arc current to 50 A in order to further diminish electrode damage.

Even under these circumstances, no stable arc could be maintained. Arc length increased dramatically during the experiments and arc rooting on the iron cathode was highly irregular as the cathode spot moved around very swiftly to find oxidized spots on the workpiece cathode. These spots were subsequently deoxidized, which in turn forced the cathode spot to move on. Thus, a deoxidized area with a diameter of about 25 mm was formed, resulting in a final arc length of about $\sqrt{(12.5^2+3^2)}$ =12.8 mm.

It was found that in the case of reverse polarity, arc voltage is much higher than in the case of straight polarity. At an arc current of 50 A and a preset arc length of 3 mm, an arc voltage of 19 to 22 V was measured, which is extremely high in comparison with the values normally encountered in straight polarity arcs (9 to 11 V).

In Table 3.9, the arc voltage, the heat input to the anode and cathode, the anodic efficiency and the cathodic efficiency are shown together with results obtained using straight polarity. The heat flow to the cathodic workpiece (reverse polarity) was found to be much higher than the heat flow to the anodic workpiece (straight polarity). For the electrode, a similar trend was found: the heat flow to the electrode in welding with reverse polarity is much higher than the heat flow to the electrode when welding with straight polarity.

It should be noted that in the case of reverse polarity, heat flow to both the anode and the cathode increased with time. This is reflected in Table 3.9, the first figure giving the value at the start of the experiment, the second giving the value at the end of the experiment. The table shows, that anodic efficiency decreased with time and cathodic efficiency increased with time. It is thought, that the lengthening of the arc with time is the most important cause for this time dependency. At longer arc length, more heat is lost in the arc column, and thus anodic efficiency and cathodic efficiency are both expected to decrease. Indeed, it has been shown in § 3.3.4 that anodic efficiency and cathodic efficiency both decrease with arc length when welding with straight polarity. The decrease in anodic (electrode) efficiency with time thus agrees with the results of the experiments described in § 3.3.4. The increase in cathodic (workpiece) efficiency, however, disagrees with expectations.

Table 3.9: Arc voltage, heat flow and efficiency for reverse polarity and straight polarity gas tungsten arcs.
Iron anode, 4.8 mm W-ThO_2 electrode, 50 A arc current and 3 mm arc length in argon shielding gas.

		reverse polarity	straight polarity
V_t	(V)	19.8 - 21.8	10.6
Q_a	(W)	155 - 158	353
Q_c	(W)	580 - 650	42.3
η_a	(%)	15.7 - 14.6	66.6
η_c	(%)	59.0 - 60.3	8.0

3.3.6 *Influence of shielding gas flow rate*

To examine the possible influence of the shielding gas flow rate on arc voltage and heat flow, an experiment was performed in which the argon gas flow rate was varied from 8 to 16 l/min. Using the standard conditions given in Table 3.5, the argon gas flow rate was found to have no effect at all on arc voltage. However, the gas flow rate does have a slight influence on the heat flow to the anode and cathode, as is shown in Fig. 3.23. This figure shows that the anode heat input and cathode heat input decrease slightly as the gas flow rate is increased. This finding is in agreement with expectation, since a higher gas flow rate will have an increased cooling effect on both anode and cathode.

As arc voltage was not affected by shielding gas flow rate, the decrease in anode heat input and cathode heat input is reflected in a similar decrease in anodic efficiency and cathodic efficiency.

3.3.7 *Influence of shielding gas composition*

An essential feature of GTA welding is that an inert gas must be used to shield the electrode and the liquid weld metal from the surrounding air. In most instances,

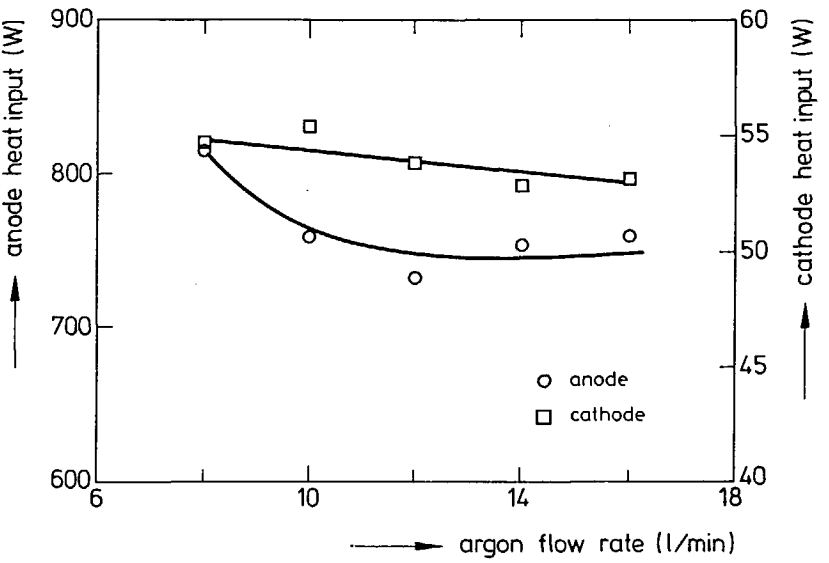

Figure 3.23 : Effect of argon gas flow rate on the heat transport to the anode and cathode.
Iron anode, 3.2 mm W-ThO_2 electrode, 3 mm arc length in argon shielding gas.

argon is used as shielding gas. Sometimes, helium or argon-helium mixtures are preferred.

To assess the influence of shielding gas composition on the heat flow during welding, experiments were carried out with shielding gas mixtures of argon and helium on copper workpieces at an arc current of 100 A. The results obtained are presented in Figs. 3.24, 3.25 and 3.26.

In Fig. 3.24 the arc voltage is plotted against the shielding gas composition. The figure shows, that arc voltage rises slowly when helium is added to the argon shielding gas and that a pronounced increase takes place when pure helium is used.

Figures 3.25 and 3.26 depict the heat flow and efficiency as a function of shielding gas composition. The behaviour of the heat flow to the anode and cathode resembles the behaviour of the arc voltage. The anodic efficiency shows a slight maximum at a shielding gas composition of about 25% argon / 75% helium. The cathodic efficiency shows a minimum at about the same shielding gas composition.

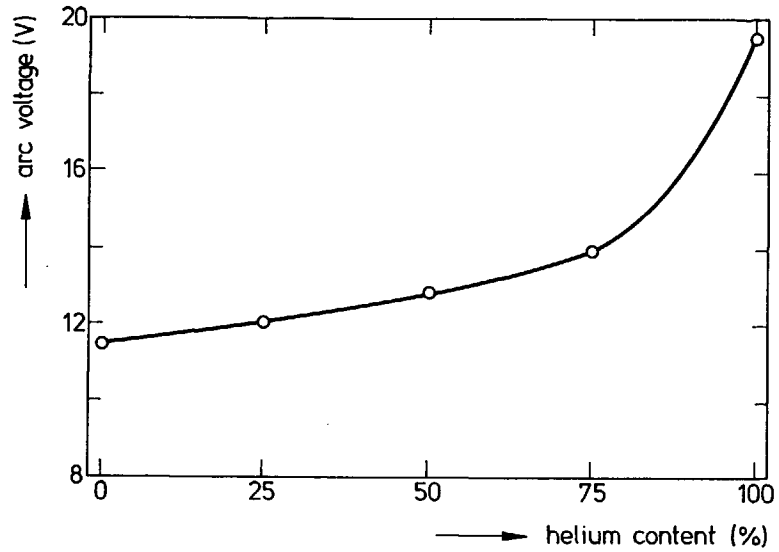

Figure 3.24 : Arc voltage as a function of the shielding gas composition.
Copper anode, 3.2 mm W-ThO_2 electrode, 100 A arc current and 3 mm arc length in Ar/He shielding gas mixtures.

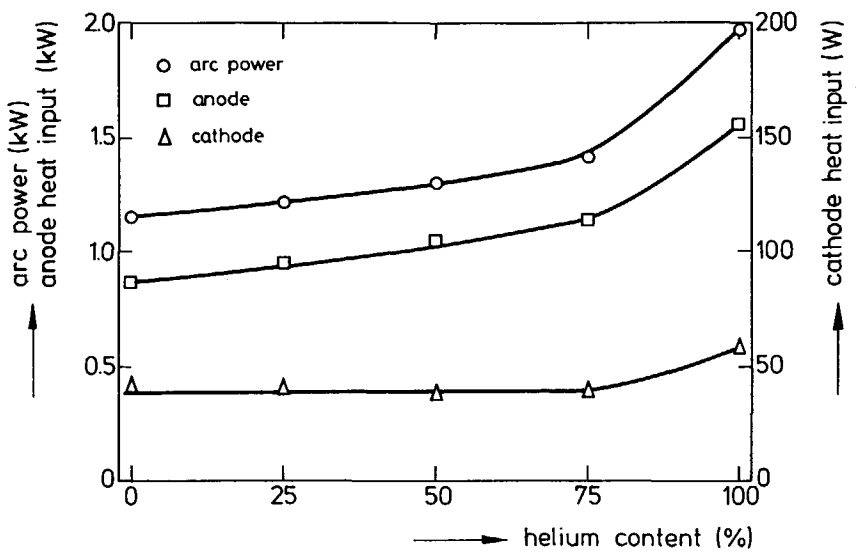

Figure 3.25 : Arc power, anode heat input and cathode heat input as a function of shielding gas composition.
Copper anode, 3.2 mm W-ThO_2 electrode, 100 A arc current and 3 mm arc length in Ar/He shielding gas mixtures.

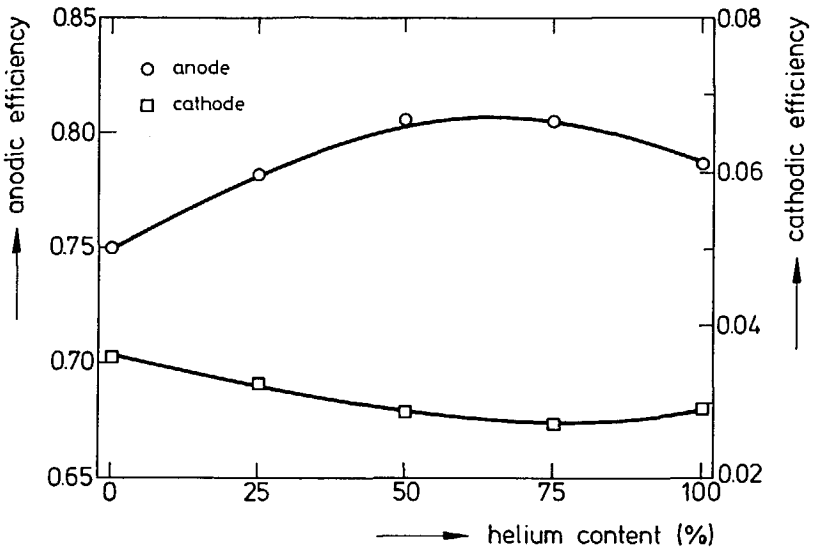

Figure 3.26 : Anodic efficiency and cathodic efficiency as a function of the shielding gas composition.
Copper anode, 3.2 mm W-ThO_2 electrode, 100 A arc current and 3 mm arc length in Ar/He shielding gases.

Experiments were also performed on iron anodes. During these experiments, it was noted that iron evaporated from the workpiece at a very high rate when using pure helium. This indicates that either the helium arc has a much higher overall temperature than argon/helium arcs, or that the anode spot is of such small dimensions that evaporation or sublimation takes place because of the constricted heat source. The amount of iron evaporated was measured and was found to account for about 0.2% of the arc power.

The results of the experiments on iron workpieces show a similar trend as the results found on copper workpieces, as can be concluded when comparing the anodic and cathodic efficiencies presented in Fig. 3.26 (copper workpiece) and 3.27 (iron workpiece). The results of heat conduction experiments carried out in a pressure vessel on mild steel workpieces show that this behaviour is independent of ambient pressure (see Chapter 4).

To examine the influence of gas composition on heat transport mechanisms to the anode and cathode further, heat transport was measured as a function of arc length

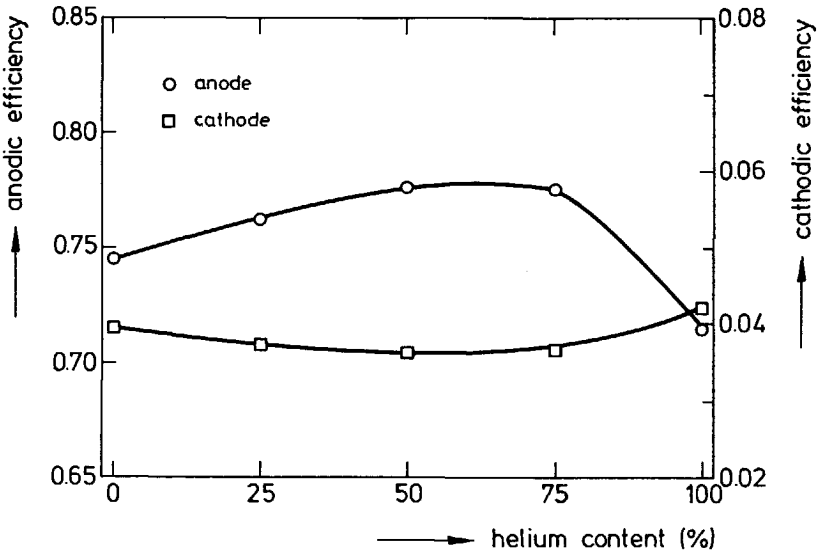

Figure 3.27 : Anodic efficiency and cathodic efficiency as a function of the shielding gas composition.
Iron anode, 3.2 mm W-ThO_2 electrode, 100 A arc current and 3 mm arc length in Ar/He shielding gases.

for various shielding gas compositions. As has been stated in the foregoing, extrapolation of arc voltage and heat flow to zero arc length could reveal valuable information. The results of these experiments are presented in Fig. 3.28. This figure depicts arc voltage-arc length curves for arcs on copper workpieces in various shielding gas mixtures and shows, that the arc voltage of arcs in helium shielding gas has a distinctly different dependence on arc length than the arc voltage of arcs in helium/argon mixtures. From Fig. 3.28, the arc column field strength and zero arc length voltage were obtained by linear extrapolation of the data obtained at arc lengths from 0.5 to 3 mm. The results are given in Table 3.10.

As can be concluded from the results presented in Table 3.10, the arc column field strength remains fairly constant at about 1 V/mm up to a helium content of about 90%. Above this helium content, arc column field strength increases abruptly to a value of about 3.5 V/mm. The zero arc length voltage increases in a much more gradual way with helium content. Obviously, helium affects arc column processes in a much different way than it affects processes in the anode fall region and cathode fall region.

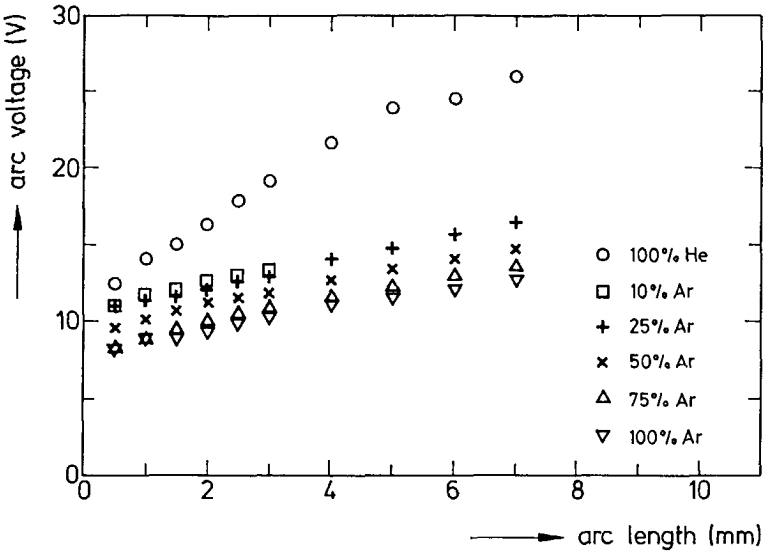

Figure 3.28: Arc voltage versus arc length for various shielding gas mixtures. Copper anode, 3.2 mm W-ThO_2 electrode, 100 A arc current in Ar/He shielding gases.

Table 3.10: Zero arc length voltage $V_t^{l=0}$ and arc column field strength E for various shielding gas compositions.
Copper anode, 3.2 mm W-ThO_2 electrode, 100 A arc current.

shielding gas composition	$V_t^{l=0}$ (V)	E (V/mm)
100 % Ar	8.5	0.95
75% Ar / 25% He	8.9	1.08
50% Ar / 50% He	9.4	1.05
25% Ar / 75% He	10.8	0.87
10% Ar / 90% He	12.8	0.72
100% He	12.5	3.48

References

3.1 O.H. Nestor,
"Heat intensity and current density distributions at the anode of high current, inert gas arcs".
Journal of Applied Physics 33 (1962), 5, p 1638.

3.2 G.J. Dunn, T.W. Eagar,
"Metal vapours in gas tungsten arcs: Part II.
Theoretical calculations of transport properties".
Metallurgical Transactions A 17A (1986), 10, p 1865.

3.3 J.F. Key,
"Anode/cathode geometry and shielding gas interrelationships in GTAW".
Welding Journal Research Supplement 59 (1980), 12, p 364s.

3.4 Welding Handbook
"Vol 1 : Fundamentals of welding".
American Welding Society, U.S. (1976).

3.5 A. Matsunawa, K. Nishiguchi,
"Arc characteristics in high pressure argon atmospheres".
Conference on Arc Physics and Weld Pool Behaviour, London (1979).

3.6 K. Goldman,
"Electric arcs in argon"
in:
"Physics of the welding arc"
Institute of Welding, London (1966).

4. Heat conduction experiments

4.1 Introduction

In this chapter, experiments are described which were carried out to obtain insight into the influence of ambient pressure on the heat flow during arc welding. Knowledge about the influence of pressure on arc behaviour is important in view of the application of arc welding under hyperbaric conditions. Hyperbaric welding in a gas filled habitat is often utilized as a construction and maintenance technique in offshore technology. When welding in a gas filled habitat under water, the gas pressure in the habitat balances the ambient pressure of the surrounding water. Often, argon is used as a shielding gas. At greater depths, however, helium is usually added to diminish the narcotic effects of pressurized argon.

In these experiments a pressure vessel was used, in which GTA welds could be made on steel plates. Use was made of thermocouples to measure the thermal cycle in the workpiece. From the cooling rate, deduced from these measurements, the workpiece heat input was calculated.

In contrast to the calorimetric method described in Chapter 3, the heat conduction method allows measurements to be made under more realistic welding conditions. During the experiments in the pressure vessel, a travelling arc was used which produced realistic weld beads in the steel workpiece.

4.2 Experimental setup

The welding experiments were carried out in a pressure vessel at ambient gas pressures from 1 to 19 bar. A schematic representation of the experimental setup in the pressure vessel is given in Fig. 4.1. In the vessel a water-cooled welding torch was mounted which was identical to the one used in the calorimetric experiments (see Chapter 3, Fig. 3.2). The torch could be moved in vertical and horizontal direction by means of two electric motors. The workpiece could be moved underneath the torch in the welding direction by means of another electric motor. Movements and displacements of the torch and the workpiece were controlled and monitored using a panel outside the vessel. A pneumatic plate exchange system allowed up to 15 plates to be welded after each other without the need to reopen the vessel in between two consecutive welding runs.

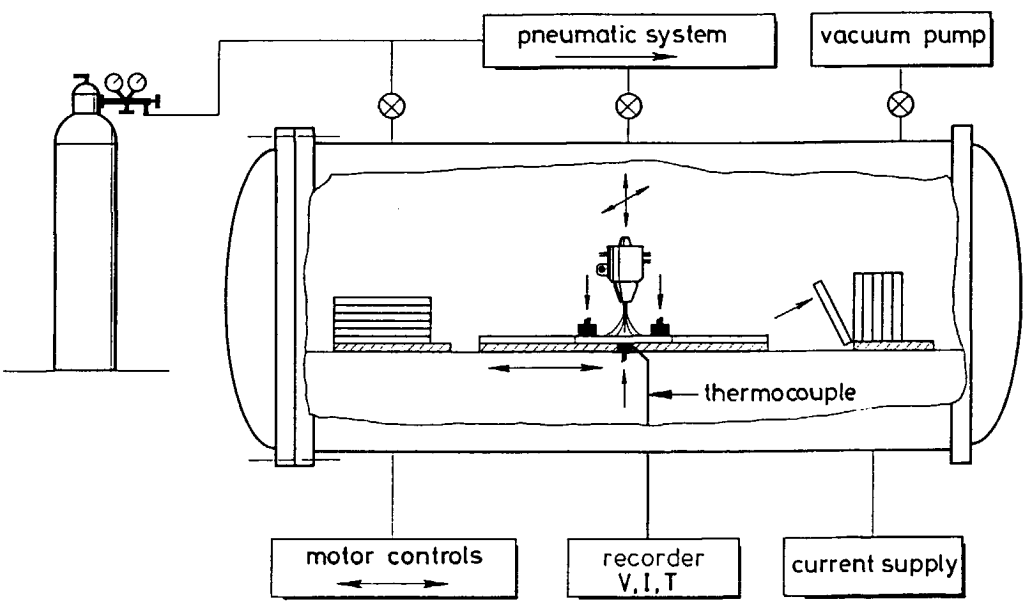

Figure 4.1: Schematic representation of the experimental setup in the pressure vessel.

The material used was steel Fe 510 in the form of plates with dimensions 200·200·10 mm and a composition as given in Chapter 3, Table 3.2. The plates were ground to provide a smooth, oxide free surface. In the backside of each plate a 5 mm deep hole was drilled in which a chromel-alumel thermocouple was placed. The free ends of the thermocouple wires were then soldered onto a small copper print, glued on the plate. Sufficient electrical contact between the thermocouple and the recorder outside the vessel was established by micro pressure cylinders.

Welding was carried out with straight polarity at constant arc length (3 mm), travel speed (1.25 mm/s) and welding current (110 and 210 A) in different gases (100% argon, 100% helium and argon/helium mixtures) at ambient pressures of 1 to 19 bar under static gas shielding conditions, i.e. without gas flow along the electrode.

At the start of the experiments a tungsten - 2% thoria electrode of 4.8 mm diameter and a 60° top angle was used. It was found, however, that with this electrode the arc becomes unstable, especially at high pressure, which results in irregular weld beads. For this reason the tungsten-thoria electrode was replaced by a pure tungsten electrode of 6.4 mm diameter and a 60° top angle. By using this type of electrode, instability of the arc could be avoided and regular weld beads were obtained. This is illustrated in Fig 4.2, in which top views of two weld beads, obtained using the two electrodes described above, are shown.

To ensure an oxygen and nitrogen free environment, the vessel was evacuated to a pressure below 0.05 bar and filled with the appropriate shielding gas to 1 bar. This procedure was repeated two or more times.

During welding, the cooling rate $\partial T/\partial t$ was measured by means of a chromel-alumel thermocouple located in the heat-affected zone (HAZ) of the weld. All welding parameters were registered on monitors outside the vessel. From the measured values of $\partial T/\partial t$ and the arc voltage V_t, the heat input Q_a from the arc to the workpiece and the anodic efficiency η_a were calculated using the Rosenthal equations described in the following section.

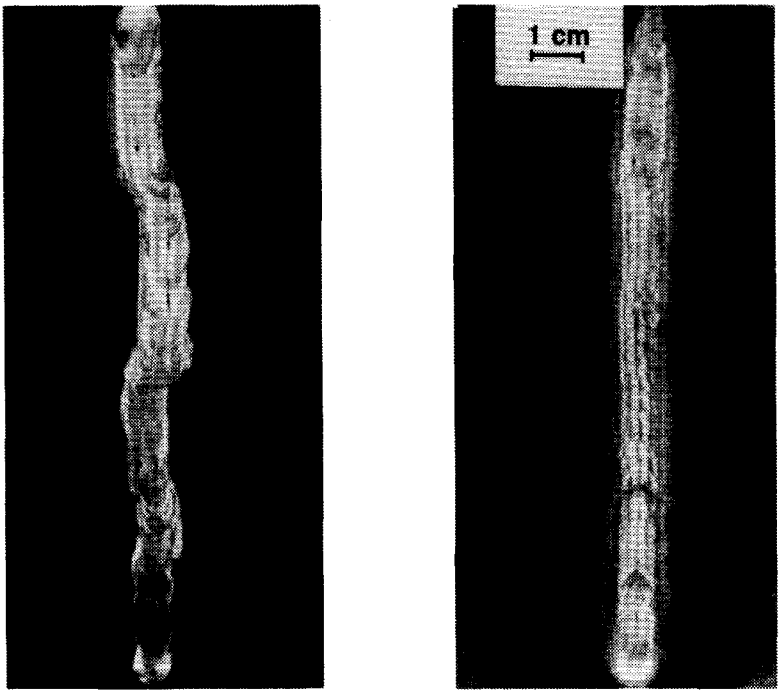

Figure 4.2: Weld beads produced at elevated pressure.
Left : 4.8 mm W-ThO_2 electrode, 200 A arc current, 13 bar argon.
Right : 6.4 mm W electrode, 200 A arc current, 14 bar argon.

4.3 Measuring method

As has been discussed already in § 2.3.2, the measurement of heat input by means of thermocouples is an indirect method based on the following analytical equations derived by Rosenthal [4.1].

In the two-dimensional case (thin plate), the temperature T is given as a function of time and place by

$$\text{2-D} : \quad T(t,r) - T_0 = \frac{Q_a}{2d\lambda v}\left(\frac{\alpha}{\pi t}\right)^{1/2} \exp\left(-\frac{r^2}{4\alpha t}\right) \tag{4.1}$$

In the three-dimensional case (thick plate), the isotherms are semi-circular and the temperature at any time and place is governed by

$$3\text{-D} : \quad T(t,r) - T_0 = \frac{Q_a}{2\pi\lambda v t} \exp\left(-\frac{r^2}{4\alpha t}\right) \tag{4.2}$$

In these equations, t, T_0, r, Q_a, v, d, λ and α represent time, the temperature at t=0, the distance to the weld centre line, the workpiece heat input, the travel speed, the plate thickness, the thermal conductivity and the thermal diffusion coefficient respectively.

Two simple methods can be used to relate the thermal cycle at a specific place to the heat input. The first method is based on measuring the cooling rate in the heat-affected zone. Differentiation of equations (4.1) and (4.2) for r=0 leads to equations which have empirically proven to be valid in the entire heat-affected zone

$$2\text{-D} : \quad \frac{\partial T}{\partial t} = -\frac{2\pi\lambda^2 d^2 v^2 (T-T_0)^3}{\alpha Q_a^2} \tag{4.3}$$

$$3\text{-D} : \quad \frac{\partial T}{\partial t} = -\frac{2\pi\lambda v (T-T_0)^2}{Q_a} \tag{4.4}$$

Distinction between the two- and three-dimensional case can be made by combining equations (4.3) and (4.4). A critical plate thickness d_{cr} can thus be found

$$d_{cr} = \sqrt{\frac{\alpha Q_a}{\lambda v}\left(\frac{1}{T-T_0}\right)} \tag{4.5}$$

In all experiments described in this chapter, the critical thickness is well above 15 mm. From the above, it then follows that the two-dimensional approach should be used.

The second method is based on the measurement of the peak temperature T_p at a specific place in the heat-affected zone. In the two-dimensional case, the peak temperature is given by the equation

$$2\text{-D} : \quad T_p(r) - T_0 = \left(\frac{1}{2\pi e}\right)^{1/2} \frac{\alpha Q_a}{d\lambda r v} \tag{4.6}$$

Preliminary experiments were performed to assess the most suitable method to calculate the heat input from the thermal history of the workpiece. In these experiments, both the cooling rate at 600°C and the peak temperature were measured with thermocouples, and the anode heat input was calculated using equations (4.3) and (4.6).

The use of the peak temperature and equation (4.6) proved to yield inaccurate results and showed poor reproducibility due to the relatively large errors in the measurement of the thermocouple position, and because the physical properties of the material have to be averaged over a certain temperature range. Data presented in literature clearly confirm the poor accuracy of this method [4.2].

When using the cooling rate in the heat-affected zone, the results are independent of the thermocouple position, and the physical constants which are to be substituted in equation (4.3) are known with much more precision, since the measurement takes place at a known and fixed temperature.

From the data obtained from the thermocouple readings, the cooling rate at 600°C was calculated by using a three-point, second order polynomial approach. In the present work the values of λ, ρ and C_p were taken to be 30 J/(Ksm), 7850 kg/m^3 and 760 J/(Kkg). The thermal diffusion coefficient is then given by $\alpha=\lambda/(\rho C_p)=5{\cdot}10^{-6}$ m^2/s. In the experiments described in this chapter, equation (4.3) was used to calculate the heat input to the workpiece. The heat transfer efficiency to the anode η_a can then be calculated using the equation

$$\eta_a = \frac{Q_a}{V_t I} \tag{4.7}$$

in which V_t and I represent the arc voltage and arc current.

When comparing results obtained in experiments at 1 bar in the pressure vessel with results obtained in the calorimetric experiments described in the previous chapter, a good correlation is found between these two methods. Differences in measured anodic efficiency did not exceed 0.05.

After sectioning, grinding, polishing and etching the welded plates, weld bead dimensions were determined using a Reichert optical microscope (average of three samples). From these dimensions the melting efficiency η_s, defined as the ratio between the heat required for heating (from room temperature) and melting the weld metal, and the heat input, was calculated using the equation

$$\eta_s = \frac{qAv}{Q_a} \tag{4.8}$$

with q the quantity of heat required to heat and melt a unit volume of metal, v the travel speed and A the cross-section area of the weld bead. In the present case the value of q was taken to be 11.5 J/mm^3.

4.4 Results and discussion

4.4.1 Influence of pressure

In the first set of experiments, the influence of pressure on workpiece heat input was investigated in an argon shielding gas atmosphere. An arc current of 210 A was used to obtain a peak temperature sufficiently high to ensure valid and accurate heat inputs to be calculated from equation (4.3).

In Fig. 4.3 the measured arc voltage is plotted as a function of ambient pressure in an argon atmosphere for an arc current of 210 A. The figure shows that arc voltage increases with pressure. Since the sum of the anode voltage drop and the cathode voltage drop is virtually unaffected by pressure [4.3], the increase in arc voltage must be attributed to arc column phenomena.

The relationship between the electric field strength E in the arc column (in V/mm) and pressure p (in bar) is often described by an equation of the form

$$E \propto p^{\beta} \tag{4.9}$$

in which β is a constant depending primarily on the shielding gas used. In the present case a least squares approximation yields

$$V = 10.8 + 2.1 p^{0.6} \tag{4.10}$$

At an arc length of 3 mm, the field strength E can thus be described as

$$E = 0.7\ p^{0.6} \tag{4.11}$$

This result is in reasonable agreement with other work dealing with the influence of pressure on arc voltage [4.4, 4.5].

In Fig. 4.4 the measured cooling rate is plotted as a function of pressure for an arc in argon and a current of 210 A. As can be seen in this figure the cooling rate slowly

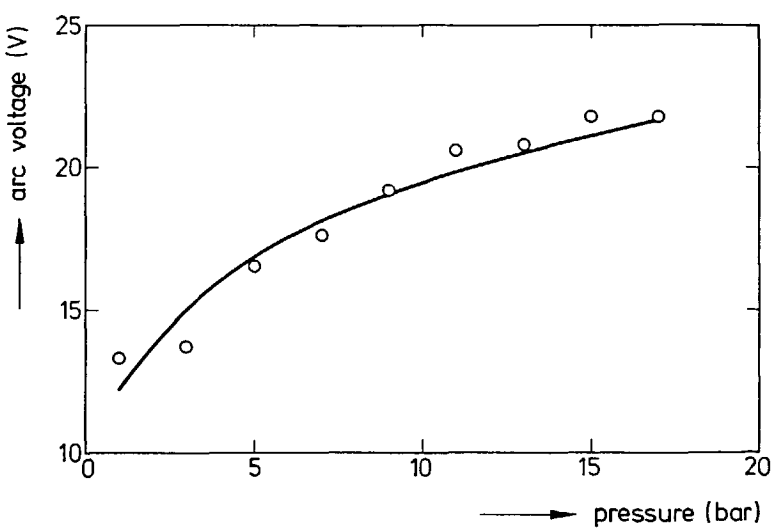

Figure 4.3: Arc voltage as a function of ambient pressure.
Steel anode, 4.8 mm W-ThO_2 electrode, 210 A arc current and 3 mm arc length in argon atmosphere.

decreases with increasing pressure. Using equation (4.3), the heat input to the workpiece was calculated. This leads to Fig. 4.5 in which the heat input is given as a function of pressure, together with the corresponding values of the arc power (V_tI).

As can be seen in Fig. 4.5, both the heat input and the arc power increase with increasing pressure. The increase of the heat input, however, is considerably smaller than that of the arc power. This means that anodic efficiency decreases with increasing pressure, as is clearly demonstrated by Fig. 4.6. Similar results were obtained by Allum [4.5, 4.6] who determined the pressure dependence of the anodic efficiency by calculating the workpiece heat input from the width of the heat-affected zone as well as by calorimetric experiments.

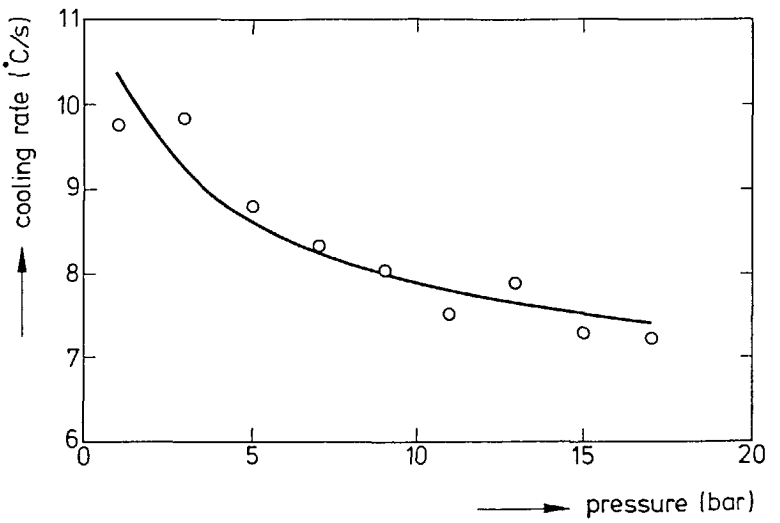

Figure 4.4: Cooling rate at 600 °C in the HAZ as a function of pressure.
Steel anode, 4.8 mm W-ThO_2 electrode, 210 A arc current and 3 mm arc length in argon atmosphere.

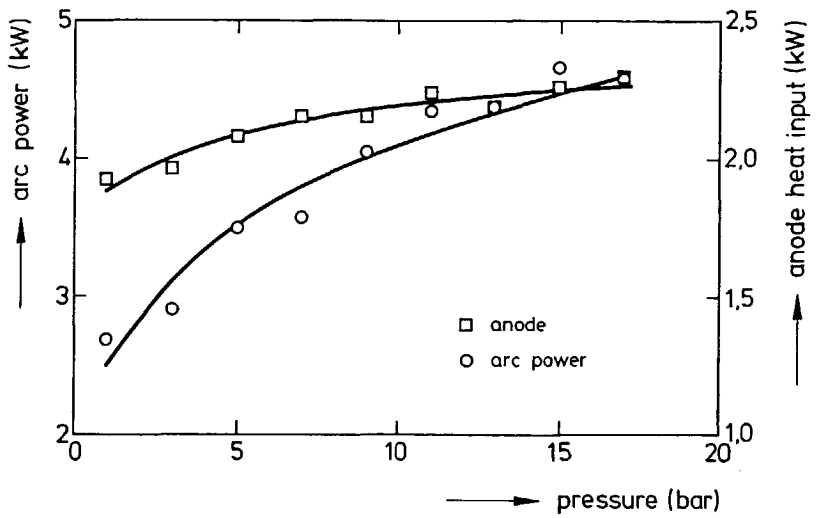

Figure 4.5: Arc power and anode heat input as a function of pressure.
Steel anode, 4.8 mm W-ThO_2 electrode, 210 A arc current and 3 mm arc length in argon atmosphere.

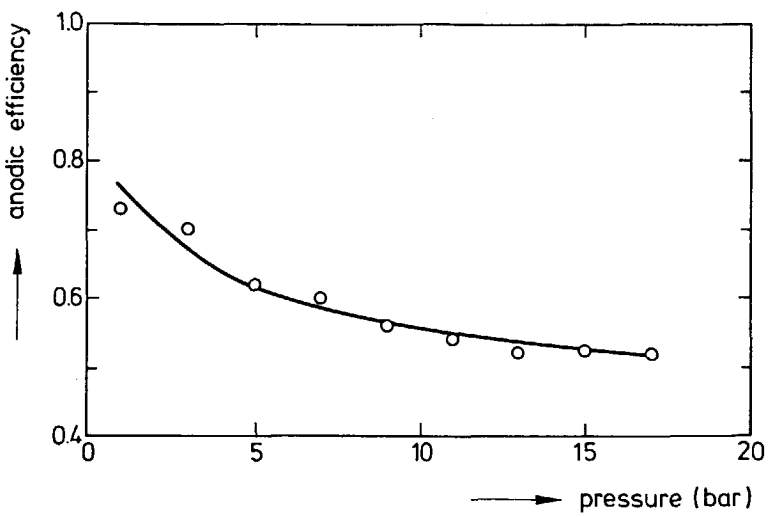

Figure 4.6: Anodic efficiency as a function of pressure.
Steel anode, 4.8 mm W-ThO_2 electrode, 210 A arc current and 3 mm arc length in argon atmosphere.

4.4.2 *Influence of gas composition*

In addition to the experiments carried out in pure argon as described above, a number of experiments was performed using argon/helium mixtures as shielding gas. Because in these mixtures weld penetration is greater than in pure argon, it was necessary to reduce the arc current to 110 A to prevent damage to the thermocouples.

It was found that for all gas mixtures employed, anodic efficiency decreases with increasing pressure. The magnitude of the anodic efficiency, however, differs significantly for the different gas mixtures. This is demonstrated by Fig. 4.7 in which the anodic efficiency is plotted as a function of the helium content for different values of the pressure. As can be seen in this figure, the anodic efficiency varies with helium content and shows a maximum at a gas composition of about 50% argon/50% helium. A similar maximum was also found in the calorimetric experiments described in the previous chapter (see Figs. 3.26 and 3.27). Taking into account the differences in the experimental conditions, the results obtained in the heat conduction experiments compare well to the results presented in the previous chapter.

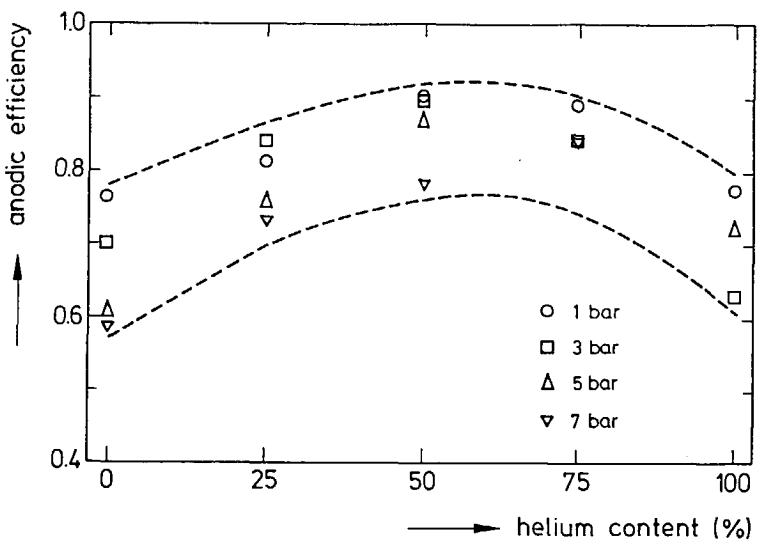

Figure 4.7: Anodic efficiency as a function of the gas composition at various pressures. Steel anode, 4.8 mm W-ThO_2 electrode, 110 A arc current and 3 mm arc length in argon/helium atmosphere mixtures.

In welding, weld bead dimensions are of great importance for the final quality of the weld. In order to measure the weld bead dimensions, all welds were sectioned, ground, polished, etched and examined microscopically.

In Fig. 4.8 the dimensions of the weld bead cross-section are given as a function of pressure for welds made in an argon atmosphere at an arc current of 210 A. The figure shows that weld bead width remains virtually constant, whereas penetration depth and cross-section surface area increase with pressure.

From the measured values of the cross-section surface area, values of the melting efficiency were calculated using equation (4.8). This yields Fig. 4.9, in which the melting efficiency is plotted as a function of pressure. The melting efficiency increases slightly with ambient pressure.

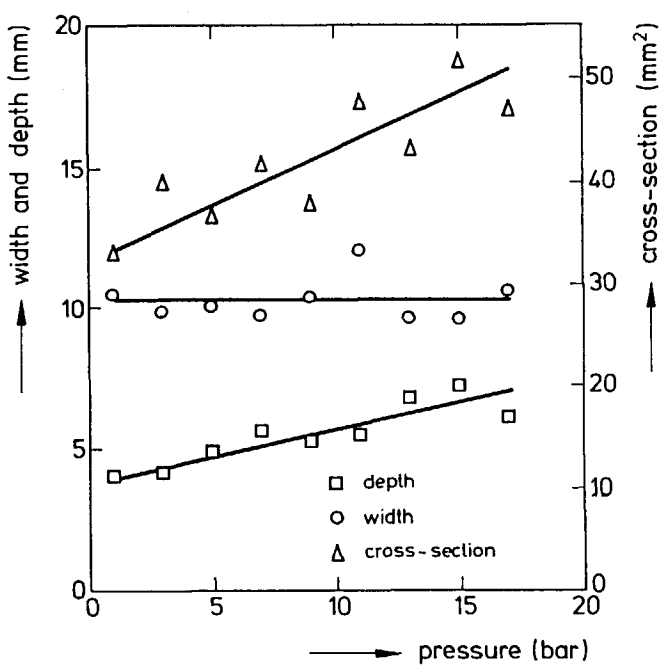

Figure 4.8: Weld bead dimensions as a function of pressure.
Steel anode, 4.8 mm W-ThO_2 electrode, 210 A arc current and 3 mm arc length in argon atmosphere.

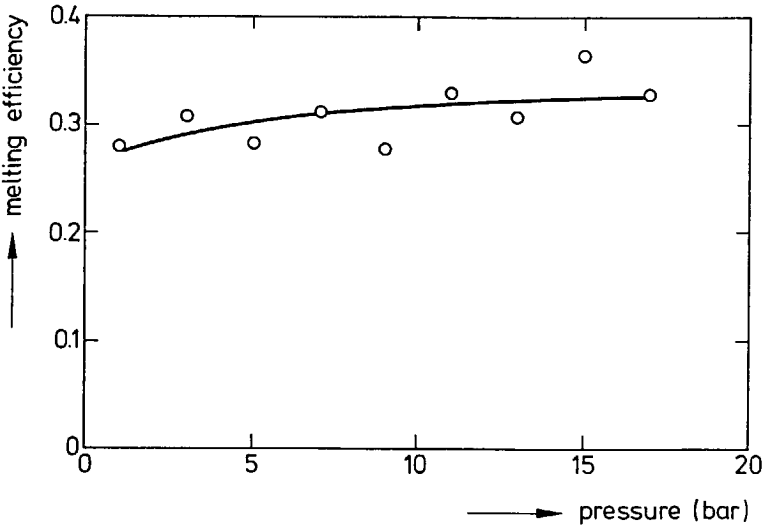

Figure 4.9: Melting efficiency as a function of pressure.
Steel anode, 4.8 mm W-ThO_2 electrode, 210 A arc current and 3 mm arc length in argon atmosphere.

Weld bead dimensions were also measured as a function of the helium content in argon/helium shielding gas mixtures. As previously stated, experiments in argon-helium mixtures were performed at a reduced arc current of 110 A. In Fig. 4.10 and Fig. 4.11, the weld bead depth and width are shown as a function of the helium content in the shielding gas for different pressures. As in the experiment in pure argon (Fig. 4.8), weld bead depth is much more affected by ambient pressure than weld bead width. Increasing the helium content in the shielding gas atmosphere increases both the weld bead depth and weld bead width. Again, weld bead depth is far more susceptible to changes in shielding gas atmosphere than weld bead width.

The melting efficiency, as calculated from the weld cross-section, is given in Fig. 4.12. It appears that the melting efficiency increases with increasing helium content for all pressures used, whereas the magnitude of the melting efficiency increases with increasing ambient pressure.

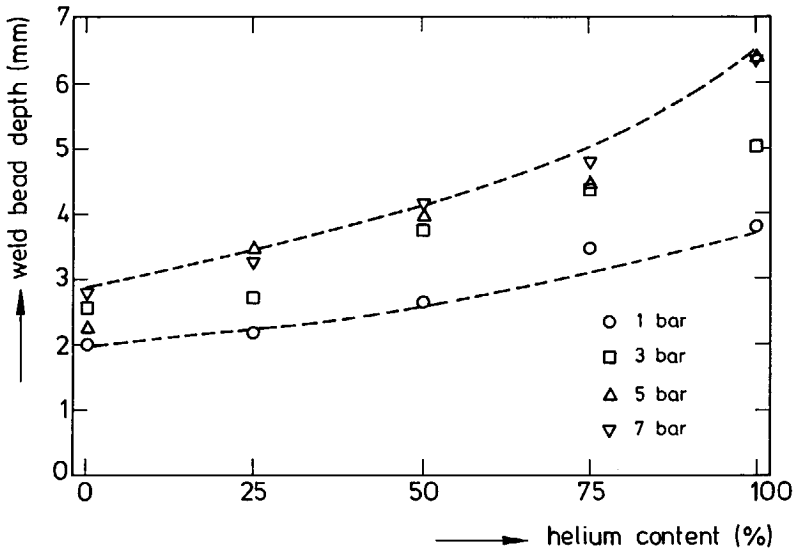

Figure 4.10: Weld bead depth as a function of the helium content for various pressures.
Steel anode, 4.8 mm W-ThO_2 electrode, 110 A arc current and 3 mm arc length in argon/helium atmosphere mixtures.

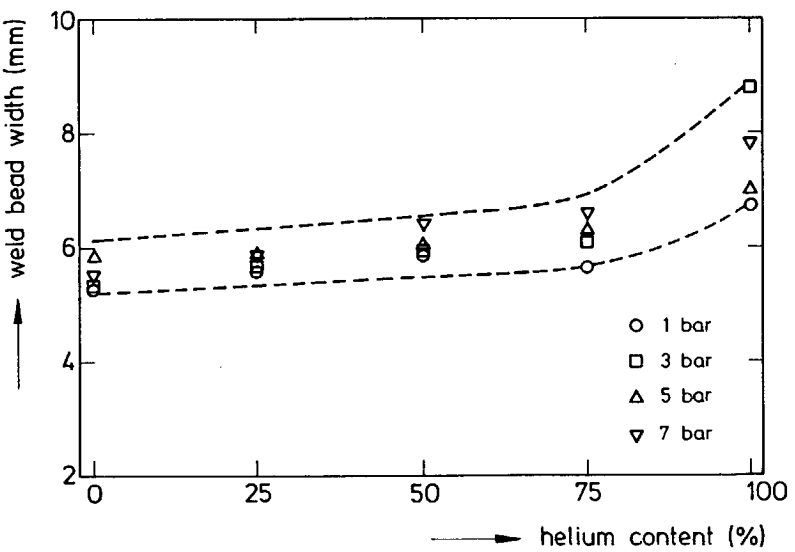

Figure 4.11: Weld bead width as a function of the helium content for various pressures.
Steel anode, 4.8 mm W-ThO_2 electrode, 110 A arc current and 3 mm arc length in argon/helium atmosphere mixtures.

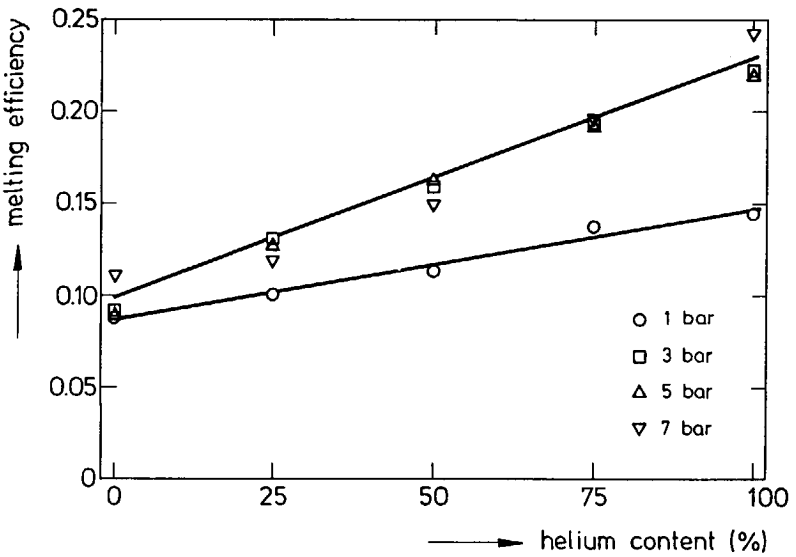

Figure 4.12: Melting efficiency as a function of gas composition for various pressures. Steel anode, 4.8 mm W-ThO_2 electrode, 110 A arc current and 3 mm arc length in argon/helium atmosphere mixtures.

References

4.1 D. Rosenthal,
"Mathematical theory of heat distribution during welding and cutting".
Welding Journal Research Supplement 20 (1941), 5, p 220s.

4.2 R.W. Niles, C.E. Jackson,
"Weld thermal efficiency of the GTAW process".
Welding Journal Research Supplement 54 (1975), 1, p 25s.

4.3 C.J. Allum,
"Effect of pressure on arcs".
Conference on Underwater Welding, Trondheim (1983).

4.4 O. Dijk, G. den Ouden,
"The effect of pressure on the TIG welding process".
Conference on Underwater Welding, Trondheim (1983).

4.5 C.J. Allum,
"The characteristics and structure of high pressure (1-42 bars) gas tungsten arcs".
Ph. D. thesis, Cranfield Institute of Technology, Cranfield (1982).

4.6 C.J. Allum,
"TIG's underwater role : present and future".
Welding and Metal Fabrication 52 (1984), 4, p 124.

5. Discussion

5.1 Introduction

In this chapter, heat flow during arc welding will be approached using the laws of arc physics. The results presented in the two previous chapters are compared to expectations based on known heat flow equations. The most widely used heat transport equations, as described briefly in Chapter 2, are

$$Q_t = V_t I = (V_a + V_c + V_p) I \tag{5.1}$$

$$Q_a = V_a I + \frac{3k(T_{pa} - T_a)}{2e} I + \frac{\phi_a}{e} I + c_a V_p I \tag{5.2}$$

$$Q_c = V_c I - \frac{3k(T_{pc} - T_c)}{2e} I - \frac{\phi_c}{e} I + c_c V_p I \tag{5.3}$$

with Q_t the arc power, Q_a and Q_c the anode heat input and cathode heat input, I the arc current, V_t the arc voltage, V_a and V_c the anode voltage drop and the cathode voltage drop, V_p the voltage drop across the arc column, ϕ_a and ϕ_c the work function of the anode and cathode material, k the constant of Planck, e the electric charge of the electron, T_a and T_c the temperature of the anode and cathode, T_{pa} and T_{pc} the plasma temperature in front of the anode and cathode and c_a and c_c fractional constants.

The anode heat flow balance and cathode heat flow balance given in equations (5.2) and (5.3) refer to volumes which comprise only the regions immediately adjacent to the electrode-arc interface. To describe the results, obtained using the calorimetric setup, however, the heat flow equations (5.2) and (5.3) should be modified. Evaluating the influence of thermoelectric effects, described in Appendix B, it follows that instead

of using the work function of the anode and cathode material, the work function of the copper extremities of the calorimeter should be used when describing the heat inputs to the anode and the cathode. This is directly due to the fact that the Peltier heat generated at the junctions between both electrodes and the copper parts of the calorimeter, is included in the measured heat flow to the anode calorimeter and cathode calorimeter.

It should also be noted that the work function is dependent on the temperature at the interface, as well as on the surface conditions. It is shown in Appendix B that the effect of temperature on the work function can be ignored, as this effect is compensated for by the Thomson effect in the conductor. Furthermore, it is shown that the work function is defined in such a way, that electrons emitted have no kinetic energy at all, i.e. T_e=0 K. This means that instead of the temperature difference between the electrons in the arc plasma and those in the electrode, the absolute temperature of the electrons in the arc plasma should be used.

On the basis of the foregoing, equations (5.2) and (5.3) can now be written as

$$Q_{am} = V_a I + \frac{3kT_{pa}}{2e} I + \frac{\phi_{Cu}}{e} I + c_a V_p I \tag{5.4}$$

$$Q_{cm} = V_c I - \frac{3kT_{pc}}{2e} I - \frac{\phi_{Cu}}{e} I + c_c V_p I \tag{5.5}$$

in which ϕ_{Cu} is the work function of copper against a vacuum at 0 K and Q_{am} and Q_{cm} represent the measured anode heat input and cathode heat input, including Peltier effects at material junctions and Thomson effects due to temperature gradients in both the anode and the cathode.

As can be seen from equations (5.4) and (5.5), all heat transport contributions at the right hand side are directly proportional to arc current. To reflect the basic processes which take place in the anode and cathode region, it was found appropriate to divide the anode heat input and the cathode heat input by the arc current. This results in the anode heat input per ampere (anode voltage, V_{anode}) and the cathode heat input per ampere (cathode voltage, $V_{cathode}$).

$$V_{anode} = \frac{Q_{am}}{I} = V_a + \frac{3kT_{pa}}{2e} + \frac{\phi_{Cu}}{e} + c_a V_P \tag{5.6}$$

$$V_{cathode} = \frac{Q_{cm}}{I} = V_c - \frac{3kT_{pc}}{2e} - \frac{\phi_{Cu}}{e} + c_c V_P \tag{5.7}$$

In most figures in this chapter, the heat flow results are presented in terms of the anode voltage and the cathode voltage. The terms anode voltage and cathode voltage may best be regarded as the generated heat per unit charge (J/C) or as the heat flow per unit charge flow (W/A) and should be distinguished from the terms anode voltage drop and cathode voltage drop (V_a and V_c). The latter reflect the voltage drops in the anode fall region and the cathode fall region.

Subtracting anode heat input per ampere and cathode heat input per ampere from the total arc voltage gives the arc column heat loss per ampere or column voltage

$$V_{column} = \frac{Q_p}{I} = V_t - \frac{Q_{am}}{I} - \frac{Q_{cm}}{I} \tag{5.8}$$

In this equation, Q_p represents the heat loss in the arc column. This quantity also comprises convective and radiative heat losses from both anode and cathode. The convective and radiative heat loss per ampere from the anode and cathode was calculated and found to be less than 0.3 V (see appendix A).

5.2 Influence of cathode conditions

In § 3.3.1, results were presented of heat flow measurements when using pure tungsten electrodes and electrodes containing oxide additions. As was stated above, division of the heat input by the arc current more directly depicts the basic processes in the arc. The results thus obtained are shown in Figs. 5.1 and 5.2, where the arc voltage, anode heat input per ampere, cathode heat input per ampere and column heat loss per ampere are given as a function of arc length. In Figs. 5.3 and 5.4, the

same quantities are depicted as a function of arc current for pure tungsten and tungsten-thoria electrodes. These four figures demonstrate, that pure tungsten electrodes have a higher cathode heat input per ampere and column heat loss per ampere than oxide-doped electrodes. The arc voltage and anode heat input are also higher when using pure tungsten electrodes, although above 100 A, the behaviour is slightly anomalous (see Fig. 5.3).

Effect of cathode composition

The difference in arc voltage between arcs, using tungsten cathodes and arcs, using oxide-doped electrodes, is about 1 V at an arc length of 3 mm (see Fig. 5.1). If it is assumed, that the anode voltage drop, V_a, and the voltage drop over the arc column, V_p, are not affected by the change in cathode composition, it follows from equation (5.1) that the cathode voltage drop V_c when using pure tungsten electrodes is about 1 V higher than in the case of oxide-doped electrodes.

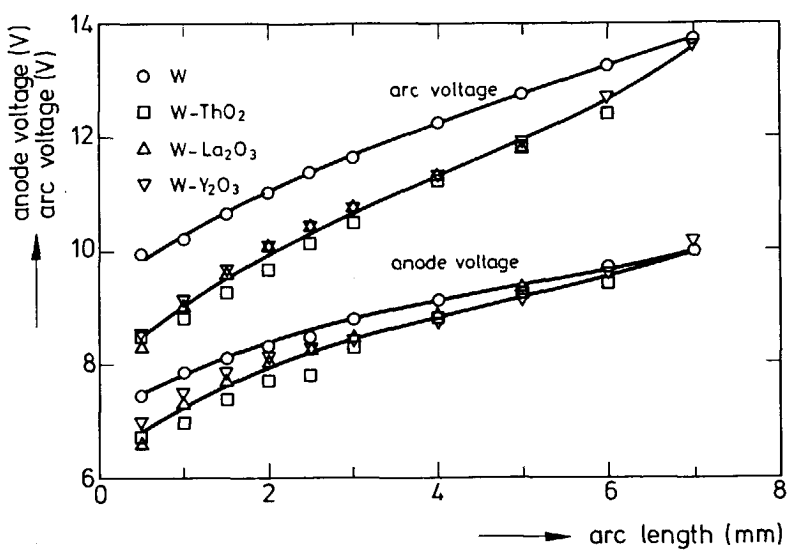

Figure 5.1: Arc voltage and anode voltage (heat input per ampere) as a function of arc length for electrodes of different compositions.
Tungsten anode, 3.2 mm electrode, 100 A arc current in argon shielding gas.

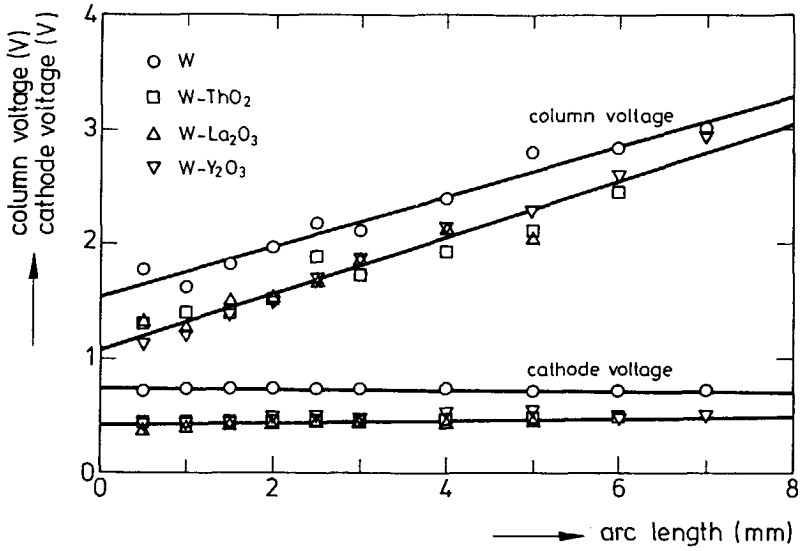

Figure 5.2: Cathode voltage (heat input per ampere) and column voltage (heat loss per ampere) as a function of arc length for electrodes of different compositions.
Tungsten anode, 3.2 mm electrode, 100 A arc current in argon shielding gas.

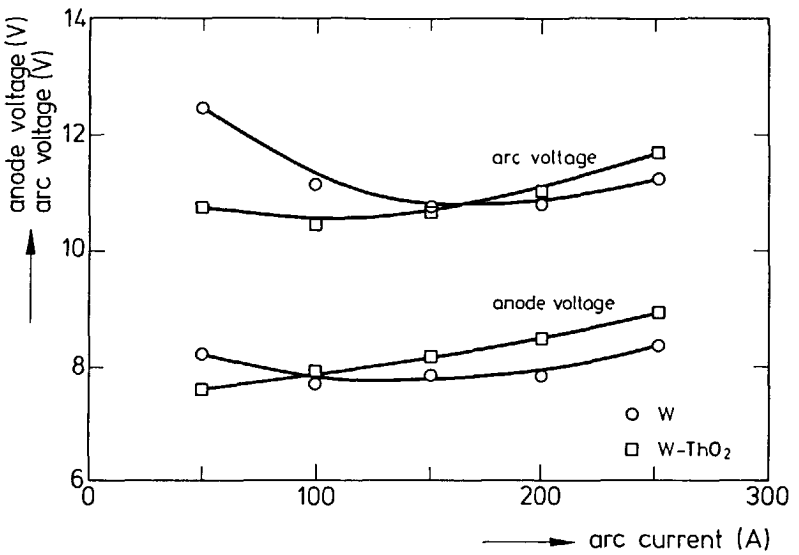

Figure 5.3: Arc voltage and anode voltage (heat input per ampere) as a function of arc current for pure tungsten and tungsten-thoria electrodes.
Tungsten anode, 3.2 mm. electrode, 3 mm arc length in argon shielding gas.

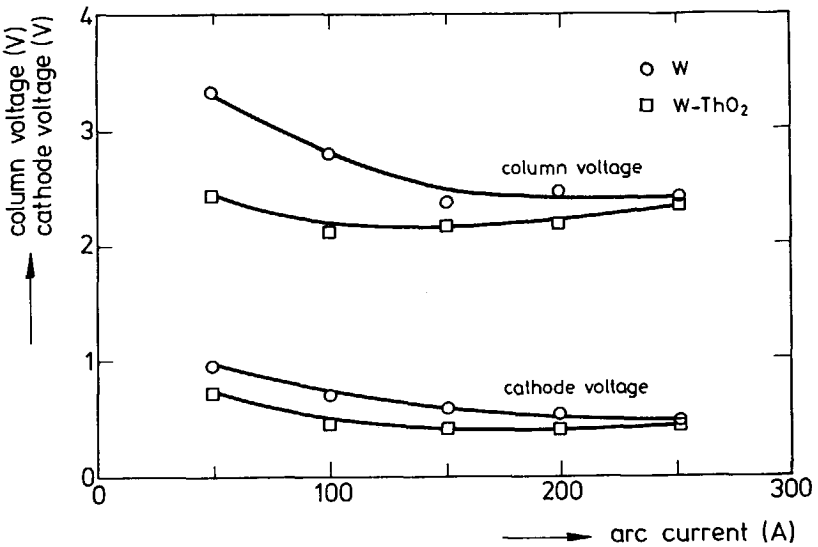

Figure 5.4: Cathode voltage (heat input per ampere) and column voltage (heat loss per ampere) as a function of arc current for pure tungsten and tungsten-thoria electrodes. Tungsten anode, 3.2 mm electrode, 3 mm arc length in argon shielding gas.

As can be concluded from the data presented in Figs. 5.1 and 5.2, not all the extra power, generated when using pure tungsten electrodes, enters the cathode. When comparing tungsten electrodes with oxide-doped electrodes at an arc length of 3 mm, the 1 V increase in arc voltage results in an increase of the cathode heat input per ampere of about 0.3 V, an increase in anode heat input per ampere of about 0.4 V, and an increase in column heat loss per ampere of about 0.3 V.

The higher cathode heat input per ampere observed in the case of pure tungsten electrodes can not be explained by changes in radiative or joule heating effects, since these are very small [5.1]. It was also shown that the change in work function of the electrode has no effect on the heat flow to the cathode calorimeter. When using electrodes with oxide additions, the decreased evaporation cooling at the electrode tip is cancelled by the Peltier effect at the junction with the copper torch body. Furthermore, the field strength in the arc plasma is not affected by the cathode material (the slope of the arc voltage-arc length curve is constant). Thus, it is reasonable to assume that the temperature of the electrons in the plasma is

independent of the cathode composition. In view of the foregoing, the difference in cathode heat input per ampere can only be due to a change in the cathode voltage drop.

However, as the change in cathode heat input per ampere of 0.3 V is much smaller than the 1 V change in cathode voltage drop, it must be concluded that not all of the heat generated in the cathode fall region is transferred to the cathode. Apparently, some of the heat generated in the cathode fall region is lost to the column. Part of this heat is subsequently transferred to the anode. This of course, has important implications for the validity of equations (5.2) to (5.8), as will be shown later in Chapter 6.

The discussion above shows that the lower work function of the oxides does not affect the heat flow balance of the cathode calorimeter. The favourable effect of oxide additions on electrode erosion is due to the effect of the work function on the temperature required to maintain sufficient electron emission. The Richardson equation, given earlier in Chapter 2, describes the thermionic emission as

$$J = AT^2 \exp\left(-\frac{\phi_c}{kT}\right) \tag{5.9}$$

In this equation, J represents the current density, T the temperature, ϕ_c the cathode work function, k the Boltzmann constant and A a material constant which has a value in the order of $6 \cdot 10^5$ $Am^{-2}K^{-2}$.

Since the constant A is not very sensitive to the material composition, the surface temperature of a tungsten electrode (ϕ_W=4.6 eV) will be much higher than that of oxide containing electrodes (ϕ_{W+OX}≈3 eV), as has indeed been found [5.2]. The heat loss from the cathode tip to its surrounding will thus be higher when using a pure tungsten electrode. To maintain the high temperature of the electrode tip, the heat production in the cathode fall region of a tungsten electrode has to be higher than the heat production in the cathode region of oxide-doped electrodes. It is believed that this is achieved by an increase in cathode voltage drop and a simultaneous decrease in cathode spot diameter.

An interesting observation is the fact that all oxide containing electrodes show an essentially similar behaviour in terms of heat input and arc voltage. Apparently, the type of oxide present is not as important as the actual presence of oxygen itself.

As already mentioned, heat is transferred from the cathode fall region to the arc column. This heat transport process is more intense in the case of pure tungsten electrodes than in the case of oxide-doped electrodes. This behaviour can be understood by the fact that the electromagnetic pressure in front of a tungsten cathode is higher than the pressure in front of oxide containing electrodes. The higher electromagnetic pressure when using pure tungsten electrodes is a consequence of the effect of electrode tip temperature on cathode spot dimensions.

Sufficient electron emission only takes place when the temperature of the tungsten electrode is higher than the temperature of oxide-doped electrodes. The higher temperature of the tungsten cathode will favour a decrease in the cathode spot dimensions. This can easily be deduced from normal heat transport formulations and from the Richardson equation (5.9). Because of the high temperature, the temperature profile at the electrode tip will be much steeper, as has also been measured spectroscopically by Ushio [5.2]. This indicates that at cathodes which exhibit higher tip temperatures, electron emission will take place within a smaller temperature range. Thus, the cathode spot is expected to be smaller in the case of tungsten cathodes. A smaller cathode spot will result in higher plasma jet velocities. This increase in plasma jet intensity will promote heat losses from the cathode fall region and lead to an increase of the column contribution to the anode heating.

As shown in Fig. 5.4, the difference between pure tungsten electrodes and tungsten-thoria electrodes in terms of cathode heat input per ampere and column heat loss per ampere disappears at high arc currents. This behaviour is accompanied by the depletion of oxides at the electrode tip, as was shown by an EPMA analysis (see Chapter 3, Fig. 3.11). This leads to the conclusion that degradation of the tungsten-thoria electrode is due to evaporation of thoria from the electrode tip. Because the oxides in the electrode tip disappear, the electrode will eventually exhibit a behaviour, similar to that of pure tungsten electrodes.

The effective work function of oxide-doped electrodes

Under similar experimental conditions, oxide-doped electrodes were found to consume less heat than pure tungsten electrodes. At 100 A arc current and 3 mm arc length, the difference in heat input per ampere amounts to about 0.3 V (see Fig. 5.2). This 0.3 V decrease in heat input per ampere, however, is too small to explain the favourable erosion behaviour of the oxide containing electrodes. As stated in appendix B, the effect of using a material with a lower work function is, that part of the cooling Peltier effect is moved from the electrode tip to the electrode/torch junction. As equation (5.3) represents the heat flow balance of the cathode tip and equation (5.5) the heat flow balance of the cathode calorimeter, combining these equations gives the actual heat production at the cathode tip Q_c[1)]

$$\frac{Q_c}{I} = \frac{Q_{cm}}{I} + \frac{\phi_{Cu} - \phi_c}{e} \qquad (5.10)$$

in which Q_{cm} is the heat flow to the cathode calorimeter, I the arc current, e the electron charge and ϕ_{Cu} and ϕ_c the work functions of copper and of the material at the cathode tip. The value of Q_c can now be calculated for a pure tungsten electrode and for an oxide-doped electrode. Taking ϕ_{Cu}=4.4 eV, ϕ_W=4.6 eV, ϕ_{W+OX}=3 eV and using the data from Fig. 5.2, i.e. pure tungsten: Q_{cm}/I=0.7 V and oxide-doped tungsten: Q_{cm}/I=0.4 V, it follows

tungsten electrode : $Q_c/I = 0.7 - 0.2 = 0.5$ V

oxide-doped electrode : $Q_c/I = 0.4 + 1.4 = 1.8$ V

Thus, according to equation (5.10), the power generated at the tip of an oxide-doped electrode is 3 to 4 times higher than the power produced at the tip of a pure tungsten electrode. This, however, is contradictory to the observed erosion behaviour. In fact, oxides are usually added to tungsten electrodes to improve welding characteristics and to reduce electrode erosion. As shown above, the 1.6 eV reduction in work function would have the opposite effect. This apparent discrepancy can be

1) Actually, combining equations (5.3) and (5.5) leaves a temperature term T_c. This temperature term should be ignored, since in equation (5.3), the work function should also have been defined against T=0 K (See Appendix B).

explained by making a distinction between the bulk work function of the electrode material and the work function at the surface.

In oxide containing electrodes, the oxide phase is randomly dispersed in the tungsten matrix. Since the electrical conductivity of the oxide phase is much lower than the conductivity of the tungsten matrix, all of the arc current will pass through the matrix. Thus, at the interface between the oxide-doped electrode and the copper electrode holder, a Peltier effect will occur which is comparable to the Peltier effect occurring when pure tungsten electrodes are used. Only at the electrode/arc interface, the oxides play a significant role in promoting thermal emission. Electrons are transported to the electrode tip through the pure tungsten matrix, and enter the oxide phase close to the electrode surface. Any Peltier effect occurring due to the difference in Fermi-energy level between the tungsten matrix and the oxide phase will thus take place close to the electrode surface.

The work function of oxide containing electrodes is usually calculated from experiments on photoelectric emission. Though the work function measured in this way might well accurately describe the condition at the cathode surface, it must be realized that the bulk work function of the cathode is not significantly altered by the addition of oxides. Hence, it is not correct to use the work function of the cathode surface when calculating the heat production at the cathode tip.

5.3 Influence of anode conditions

In § 3.3.2, results of experiments performed with copper, tungsten, steel and iron workpieces have been described. The arc voltage, anode heat input per ampere, cathode heat input per ampere and column heat loss per ampere for the four anode materials are given in Figs. 5.5 and 5.6 as a function of arc length. For the four anode materials used, differences in arc voltage and anode heat input per ampere are in the range of 1 V. Of these materials, copper showed the highest arc voltage and anode heat input per ampere. As becomes clear from Fig. 5.6, the cathode heat input per

ampere and the column heat loss per ampere are virtually independent of anode composition.

As was already stated in Chapter 3, a distinction should be made between the behaviour of the iron and steel workpieces on one hand, and the behaviour of the copper and tungsten workpieces on the other. The copper and tungsten workpieces did not show any melting. In the case of iron and steel workpieces, however, anode melting took place. This resulted in poor reproducibility, since the molten pool tended to rise towards the electrode, thus decreasing arc length. The results of the experiments on iron and steel resemble the results found when using pure tungsten anodes. In view of the poor reproducibility, however, the results obtained on the anodes of iron and steel will be discarded in the remainder of this section.

In the anode heat flow model described by equation (5.6), the work function of the anode does not influence anode heat transport, since this effect is counteracted by Peltier effects in the calorimeter. Furthermore, the influence of the Joule heating can be neglected because of the large conducting cross-section.

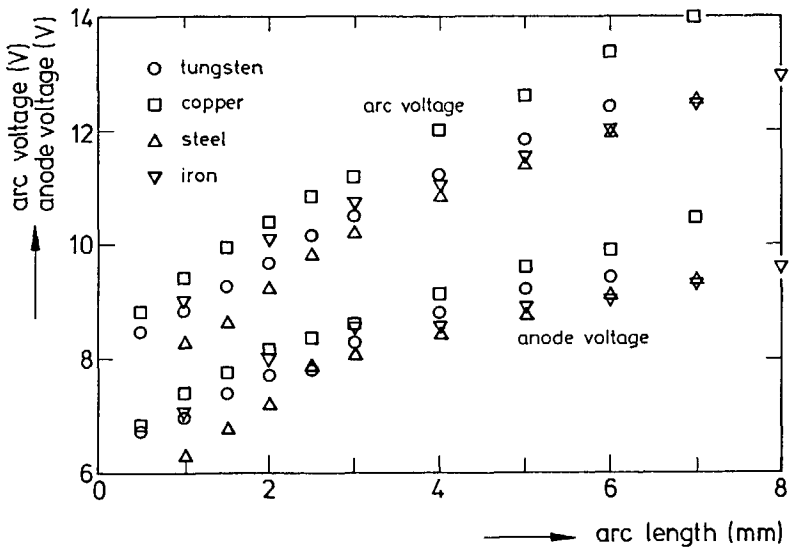

Figure 5.5: Arc voltage and anode voltage (heat input per ampere) for tungsten, copper, steel and iron anodes as a function of arc length.
3.2 mm W-ThO_2 electrode, 100 A arc current in argon shielding gas.

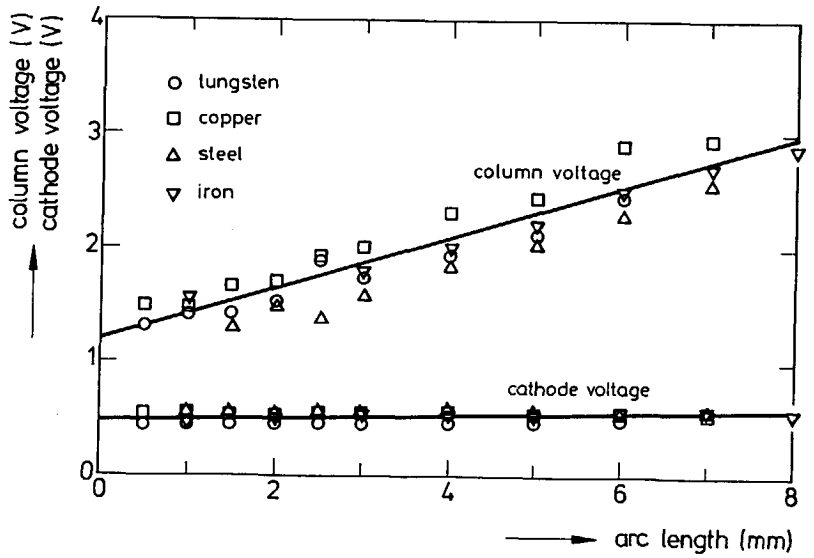

Figure 5.6: Cathode voltage (heat input per ampere) and column voltage (heat loss per ampere) for tungsten, copper, steel and iron anodes as a function of arc length. 3.2 mm W-ThO_2 electrode, 100 A arc current in argon shielding gas.

From the data presented in Fig. 5.5 it becomes clear that the copper anode has a higher arc voltage and anode heat input per ampere than the tungsten anode. The cathode heat input per ampere is not affected (see Fig. 5.6), indicating that the cathode voltage drop is about the same for both anode materials. Because the arc voltage, extrapolated to zero arc length, is higher in the case of a copper anode, it can be concluded that copper has a higher anode voltage drop than tungsten. Since no evaporation of the workpiece material was observed, the difference in anode voltage drop can only be due to the lower surface temperature of the copper workpiece. Finite difference calculations show that the surface temperature of the copper workpiece is below 300°C, whereas the surface temperature of the tungsten workpiece was calculated to be about 700°C (see Appendix A).

In the anode fall region, the temperature of the heavy particles decreases from the plasma temperature to the temperature of the anode surface, whereas the electron temperature in the anode fall region remains relatively high [5.3]. Decreasing the anode temperature will thus lead to a decrease of the heavy particles temperature in the anode fall region. Due to the interaction between electrons and heavy particles, the average electron temperature will decrease as well, which will reduce electrical

conductivity and current density in the anode fall region. Furthermore, the increase of the temperature difference between the anode and the plasma will lead to an increase in anode layer thickness. The decrease in current density J and the increase in anode layer thickness λ will result in a change of the anode voltage drop V_a, as can be deduced from the Child-Langmuir relation (see § 2.2.3)

$$\lambda \approx \left(\frac{4\varepsilon_0}{9}\right)^{1/2} \left(\frac{2e}{m}\right)^{1/4} \frac{V_a^{3/4}}{J^{1/2}} \tag{5.11}$$

From the above, it follows that anode temperature affects the anode voltage drop. The 0.7 V difference in arc voltage can thus be explained qualitatively by the difference in anode surface temperature.

The results obtained in experiments on iron and steel workpieces, although characterized by relatively large scatter, match the results found when using tungsten anodes. The surface temperature of iron and steel workpieces was calculated to be higher than the surface temperature of the tungsten anode (see Appendix A). A complicating factor in comparing these data could be the presence of metal vapours originating from the weld pool formed on the iron and steel workpieces.

The presence of metal vapours only extends over a region very near to the workpiece [5.4] and does not significantly influence the arc column behaviour or the cathode heat input, as is clear from Fig. 5.6. The fact that the metal vapours remain close to the anode is quite understandable, as the plasma jet inhibits the metal vapour to move towards the cathode. It is thought, that the relatively low ionization potential of the metal vapour (7.9 V for iron, 15.8 V for argon) will increase the electron density near the anode and simultaneously decrease the electron temperature in the plasma adjacent to the anode. This decrease in temperature will slightly decrease the heat input to the anode due to the reduced thermal energy of the electrons. However, the higher electron density will increase current density and thus increase the anode voltage drop, as can be deduced from the Child-Langmuir equation (5.11).

The outcome of the combined occurrence of these two effects can not be calculated by simple means. However, the small differences in arc voltage and anode

heat input observed when using iron anodes of thicknesses of 2, 5 and 10 mm indicate, that the influence of metal vapours is only very small.

It can be concluded, that anode composition in itself has no significant effect on the heat transport during GTA welding. The work function of the anode has no direct effect on processes playing in the anode fall region. Furthermore, the influence of metal vapours originating from the anode was shown to be relatively small. The differences in anode heat input found can be explained in terms of the anode surface temperature. The anode surface temperature is important because of its effect on the anode voltage drop.

5.4 Influence of arc current

The effect of arc current on arc power, anode heat input and cathode heat input has already been discussed in § 3.3.3. In the arc current range of 10 to 250 A, arc power, anode heat input and cathode heat input rise almost linearly with arc current. In Figs. 5.7 and 5.8, the arc voltage, anode heat input per ampere, cathode heat input per ampere and column heat loss per ampere are depicted as a function of arc current for arc currents from 10 to 100 A and from 50 to 250 A. As is shown in these figures, the cathode heat input per ampere and column heat loss per ampere decrease as arc current is increased. This decrease is most notable at arc currents below 25 A. Arc voltage and anode heat input per ampere also decrease as arc current is increased, but start to increase again after a slight minimum at an arc current of around 25 A.

These effects can be explained qualitatively in terms of three different phenomena. With increasing current, heat transport per ampere to the anode and cathode, and also the column heat loss per ampere, will change due to:

- changes in the anode voltage drop and cathode voltage drop;
- an increase of the electron temperature in the arc plasma;

- an increase in the plasma jet velocity. This will increase the column convective contribution to the anode heating and decrease the heat loss in the arc column.

The cathode heat input per ampere decreases with arc current. The most notable decrease takes place at low arc current. The sharp decline in cathode heat input per ampere in the arc current range below 25 A can not be explained by the change in electron cooling, since the Thomson cooling effect is only small. Furthermore, the plasma jet is directed from the cathode to the anode, so that convective heating is not thought to play a role at the cathode. It follows that the decrease in cathode heat input per ampere with increasing arc current is due to a decrease in cathode voltage drop, as has also been reported by Finkelnburg [5.5].

The column heat loss per ampere is also found to decrease as arc current is increased. This decrease is most notable for arc currents below 50 A, whereas it is almost negligible at arc currents above 100 A. This is in accordance with expectation,

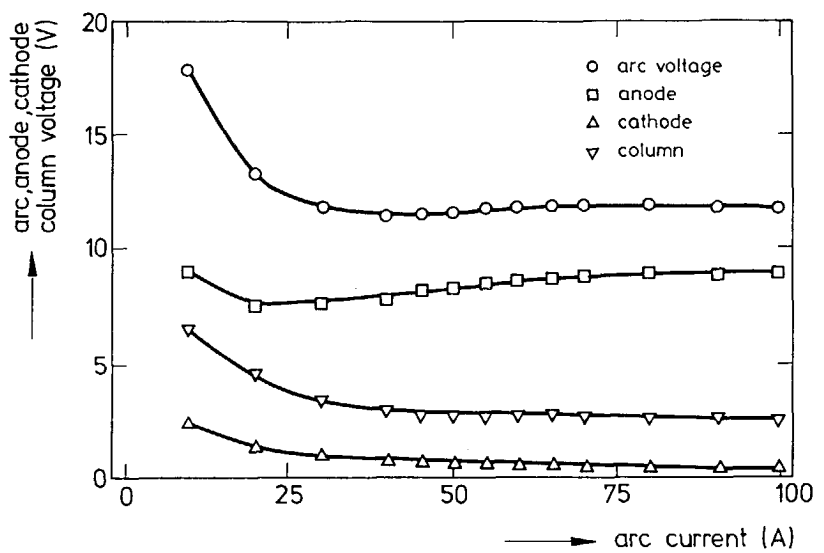

Figure 5.7: Effect of arc current on arc voltage, anode voltage and cathode voltage (heat input per ampere) and column voltage (heat loss per ampere).
Copper anode, 3.2 mm W-ThO_2 electrode, 3 mm arc length in argon shielding gas.

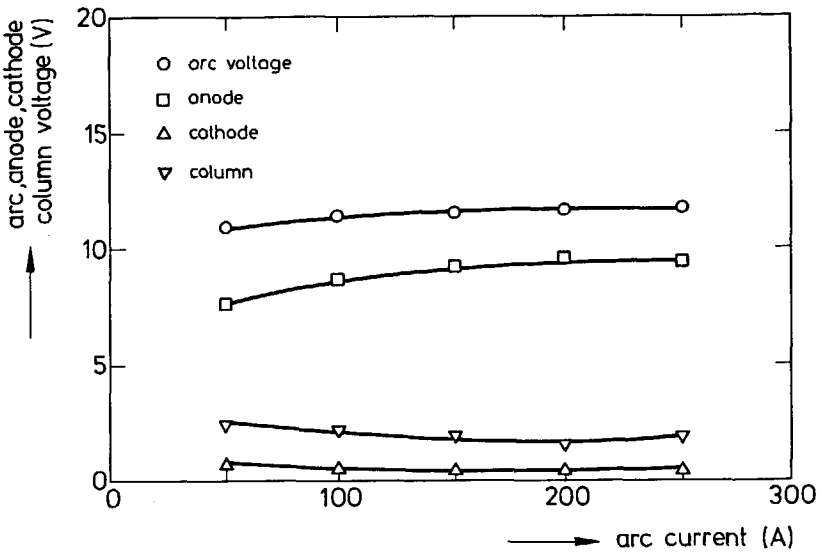

Figure 5.8: Effect of arc current on arc voltage, anode voltage and cathode voltage (heat input per ampere) and column voltage (heat loss per ampere).
Copper anode, 3.2 mm W-ThO_2 electrode, 3 mm arc length in argon shielding gas.

since the arc temperature increases with arc current, thus increasing the degree of ionization and the electrical conductivity of the arc plasma. At low current (<50 A), the arc is relatively unstable and a high field strength in the arc column is needed to maintain a plasma temperature which exhibits a sufficient degree of ionization. At these low arc currents, the temperature of the arc plasma is relatively low and the column heat loss per ampere will be high due to the high arc column field strength. At arc currents above 50 A, the rate of the decrease in column heat loss per ampere becomes increasingly smaller. This is reflected by the electric field strength in the arc, which was measured (from the slope of the arc voltage-arc length curve) to remain virtually constant at arc currents above 100 A.

Except for arc currents below 25 A, anode heat input per ampere rises gradually with arc current. The high anode heat input per ampere at low arc current is thought to be a consequence of the increased contribution of the arc column. The column heat loss per ampere is relatively high at low arc current, so that the column convective

For the cathode, the heat input was found to be independent of arc length. It then follows that the constant c_c in equations (5.3), (5.5) and (5.7) is zero. This is in agreement with expectation. The convective contribution to the cathode heat input is zero, since the plasma jet is directed from the cathode to the anode, whereas the radiative contribution is negligibly small because of the small surface area of the cathode and because of the small fraction of the arc power that appears as radiation.

Extrapolation to zero arc length, elimination of arc column contribution

As described in Chapter 2, the extrapolation of arc voltage to zero arc length is supposed to yield the sum of the anode voltage drop and the cathode voltage drop. This follows directly from equation (5.1) by letting the voltage drop over the arc column approach zero. It is reasonable to assume that the sum of the anode heat input per ampere and the cathode heat input per ampere, extrapolated to zero arc length yields the arc voltage at zero arc length. Another way of describing this assumption would be, to postulate that the sum of the anodic efficiency and cathodic efficiency approaches 100% when arc length approaches zero. When the voltage drop over the arc column V_p is assumed to be zero, combination of equations (5.1), (5.6), (5.7) and (5.8) gives

$$\frac{Q_p}{I} = V_a + V_c - \frac{Q_{am}+Q_{cm}}{I} = \frac{3k}{2e}(T_{pc}-T_{pa}) \qquad (5.15)$$

Table 5.1 gives the extrapolated values of Q_p/I for various shielding gas compositions on iron and copper anodes. From the values given in the table it follows that the temperature term on the right hand side of equation (5.15) is about 1.4 V. With a thermal energy per electron of $3kT/2 = T \cdot 1.4 \cdot 10^{-23}$ J, the electron temperature in front of the cathode, T_{pc}, is about 11000 K higher than the electron temperature T_{pa} in front of the anode. The electrons leaving the cathode region must transfer a significant amount of energy to the neutral atoms to account for this fall in temperature. Differences in electron temperature of this order have been found at normal arc length [5.7]. Apparently, this difference does not disappear when arc length approaches zero.

Table 5.1 : The arc column heat loss per ampere (Q_p/I) at zero arc length for various shielding gas compositions on iron and copper anodes.
3.2 mm W-ThO_2 electrode, 100 A arc current.

anode	Fe	Cu
gas composition	Q_p/I (V)	Q_p/I (V)
100% He	1.7	1.5
75% He + 25% Ar	1.3	1.7
50% He + 50% Ar	1.6	1.4
25% He + 75% Ar	1.2	1.3
100% Ar	1.4	1.3

It has already been suggested in § 5.2 that some of the heat generated in the cathode region is lost to the column. This is confirmed by the results just described and can be understood by realizing that for the existence of an arc, both electrons and ions are necessary. Apart from inelastic collisions producing ions and electrons, elastic collisions between electrons, ions and atoms will occur. This process will extract energy from the system. The observed discrepancy of 1.4 V can largely be explained by this phenomena. The radiative and convective losses from both electrodes to the surroundings will also contribute to the column heat loss per ampere at zero arc length. These contributions, however, only account for less than 0.3 V (see Appendix A).

5.6 Influence of polarity

As has been described in § 3.3.5, arc rooting on the cathodic workpiece was observed to be highly irregular in the case of reverse polarity. This is thought to be a consequence of the large dimensions of the cathodic workpiece. Due to the better cooling of the cathode surface, the surface temperature of the cathodic workpiece will

be much lower than the surface temperature of a cathodic electrode and thermionic emission of electrons will become increasingly difficult. Thus, field emission becomes an important emission mechanism.

Field emission takes place when isolating oxide films are formed on the cathode surface. On these oxide films, positive ions can condense. This helps to build up a large electric field and promotes field emission [5.8]. The intense heat at the cathode spot subsequently evaporates (or sublimates) the oxides, which means that once a certain oxidized spot has served as cathode spot, it is destroyed, forcing the cathode spot to move on.

Thermionic emission will only play a minor role in welding with reverse polarity. The temperature of the workpiece surface is so low, that thermionic emission could only take place at oxides with work functions considerably lower than those of oxide-doped electrodes normally used in welding with straight polarity. The possibility of thermionic emission, however, can not be dismissed totally.

As was shown in § 3.3.5, a cathodic workpiece (reverse polarity) receives more heat than an anodic workpiece (straight polarity). The anodic electrode (reverse polarity) also consumes more power than the cathodic electrode (straight polarity). The results in terms of heat input per ampere are given in Table 5.2. The table shows, that at 50 A the power lost in the column in the case of reverse polarity is about twice as high as in the case of straight polarity. This can be explained by the increased effective arc length. The maximum arc length at the end of the experiment with reverse polarity was 13 mm, whereas arc length was 3 mm in experiments with straight polarity. In view of this difference in arc length, however, the column heat loss per ampere is in fact rather small. In this respect it should be noted that arc rooting took place over the entire deoxidized area of the workpiece cathode, so that the time averaged arc length will be in between 3 and 13 mm. Consequently, the arc column field strength during welding with reverse polarity might well be comparable to the arc column field strength when welding with straight polarity.

The heat flow to the workpiece in the case of reverse polarity is relatively high. Clearly, the cathode voltage drop is much higher than in the case of a gas tungsten arc in normal operation. If field emission is the governing electron producing process

Table 5.2: Arc voltage, anode voltage, cathode voltage and column voltage (V_t, Q_{am}/I, Q_{cm}/I, Q_p/I) in the case of reverse and straight polarity.
Iron anode, 4.8 mm W-ThO_2 electrode, 50 A arc current and 3 mm arc length in argon shielding gas.

		reverse polarity	straight polarity
V_t	(V)	19.8 - 21.8	10.6
Q_{am}/I	(V)	3.1 - 3.2	7.1
Q_{cm}/I	(V)	11.7 - 13.1	0.85
Q_p/I	(V)	5.0 - 5.5	2.7

at the cathode, this is not surprising. Due to the high field strength required for field emission, it is necessary that the cathode voltage drop be higher than in the case of thermionic emission. An estimate of the cathode voltage drop yields a value in the range of 16 to 20 V.

The heat flow to the electrode in the case of reverse polarity is surprisingly low. On the basis of the heat transport formulation given in equation (5.6), the minimum heat input per ampere is given by the sum of the anode voltage drop, a contribution related to the anode work function and the electron thermal contribution. With an anode voltage drop of 1 V, a work function of ϕ_{Cu}=4.4 eV and an electron thermal contribution of $3kT_{pa}/2e$=1.3 V (T_{pa}=10000 K), a heat input per ampere of 6.7 V is found. This estimate is much higher than the experimentally found heat input per ampere of 3.1 V. Apparently, part of the heat produced at the anode is lost. Two processes are important in this respect.

a. Because of the small dimensions of the anodic electrode, a plasma jet will develop which is directed towards the cathodic workpiece. Thus, cold shielding gas is forced along the electrode which will reduce the amount of heat measured at the torch calorimeter.

b. The surface temperature of the anodic electrode is so high, that radiation becomes an important heat drain. At an arc current of 50 A, the tungsten electrode already showed considerable melting at its tip. In fact, the tip of the 4.8 mm diameter

tungsten electrode was observed to form a molten sphere. At the melting point of tungsten (3680 K), the emissivity of tungsten is about 0.35, so that the emitted power can be calculated from the Stefan-Boltzmann law to be 3.6 W/mm^2. Thus, the radiative power loss from the electrode tip amounts to 130 W. At an arc current of 50 A, this accounts for a heat loss per ampere of 2.6 V.

It is concluded, that the low anode heat input measured is due to an excessive heat loss from the electrode.

5.7 Influence of gas composition

In § 3.3.6 it was shown that anode heat input increases gradually with increasing helium content up until a helium content of 75% and that a more pronounced increase in heat input occurs at higher helium content. Cathode heat input remains constant for gas compositions containing less than 75% but also increases at higher helium content. The results in terms of arc voltage, anode heat input per ampere, cathode heat input per ampere and column heat loss per ampere are presented in Fig. 5.9. As arc current was kept constant in these experiments, the trends in terms of heat input per ampere are identical to those in terms of heat input.

It is clear from the results presented in Fig. 5.9 that anode heat input per ampere and column heat loss per ampere are much more affected by gas composition than cathode heat input per ampere. As was shown in Chapter 3, Table 3.10, the arc column field strength is about 0.9 V/mm for shielding gases containing 0 to 90% helium and shows a distinct increase when pure helium is used. The slow rise in arc column field strength at low helium contents can be explained by realizing that argon is the main supplier of electrons in the arc plasma, as the ionization energy of argon is substantially lower than that of helium (15.8 eV versus 24.6 eV). The effect of a reduced argon content can be counteracted by a small rise in arc plasma temperature, which will significantly increase the degree of ionization of the argon. Only at argon

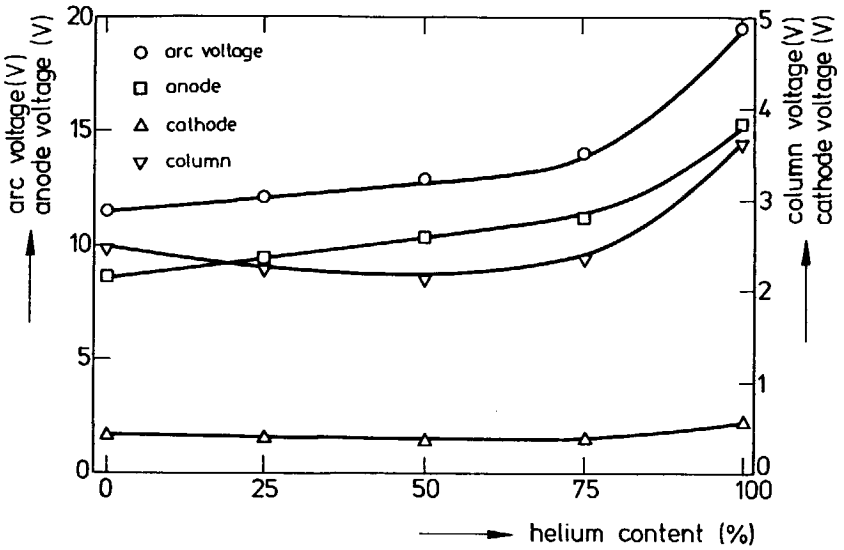

Figure 5.9: Arc voltage, anode and cathode voltage (heat input per ampere) and column voltage (heat loss per ampere) as a function of helium content.
Copper anode, 3.2 mm W-ThO_2 electrode, 100 A arc current and 3 mm arc length.

contents which are too small to provide a sufficient electron density, the arc plasma temperature will rise considerably in order to ionize the helium atoms. Small amounts of elements with low ionization potentials can profoundly alter the behaviour of plasmas, as was shown by Johnson and Pfender [5.9]. Sharapov [5.10] calculated the effective ionization potential of gas mixtures. The effective ionization potential is defined as the ionization potential at which the electron density in a pure gas would be equal to the electron density in the employed gas mixture. Using the approach of Sharapov, the effective ionization potential of argon/helium mixtures was calculated and is given as a function of the helium content in Fig. 5.10. This figure shows that the effective ionization potential has a similar dependence on gas composition as the arc column field strength given in Table 3.10 and the column heat loss per ampere given in Fig. 5.9. The fast rise in arc column field strength at high helium content is in contradiction to the more gradual dependence found by Ludwig [5.11]. It should be noted, that the form of the curve in Fig. 5.10 is strongly dependent on the plasma temperature. The arc current used in these experiments is relatively low, resulting in a low plasma temperature. As shown above, the rapid rise in the column heat loss per

ampere above a helium content of 75% can be explained by the effect of helium on the effective ionization potential of the shielding gas mixture.

The increase in anode heat input per ampere at shielding gas compositions containing over 75% of helium is partially due to the increased convective contribution of the arc column. The increase in the Thomson effect due to the increase in plasma temperature will also play a role. The anode heat input per ampere, however, also increases at low helium contents. As the increase in arc column temperature with increasing helium content is not expected to be substantial at low helium content and, moreover, the arc column field strength and thus the power generated in the column is constant at low helium content, this must be due to an increase in anode voltage drop V_a. As was shown in Chapter 3, Table 3.10, the zero arc length voltage, representing the sum of anode voltage drop and cathode voltage drop, indeed increases with increasing helium content in the shielding gas.

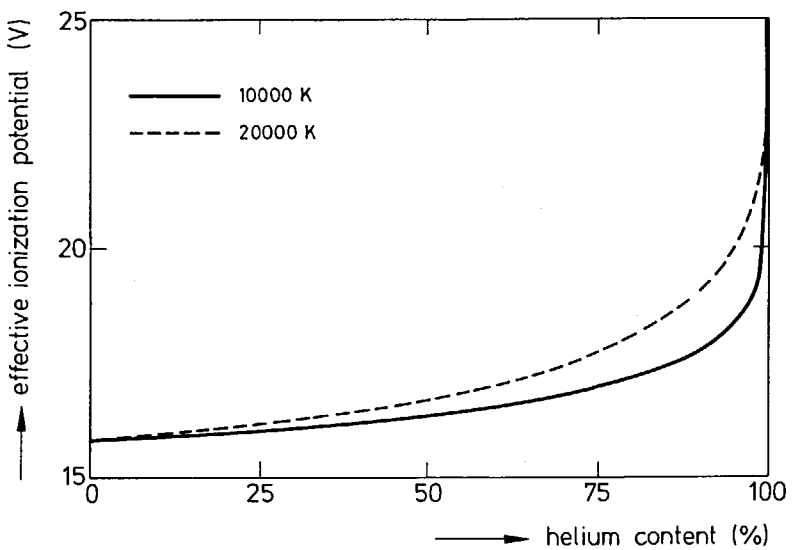

Figure 5.10: Effective ionization potential as a function of the helium content in argon-helium shielding gas mixtures [5.10].

In the case of the cathode, the heat input per ampere is constant for helium contents up to about 75%. The higher plasma temperature when using shielding gases with high helium content will result in a lower cathode heat input by increased Thomson cooling of the electrode. The observed rise in cathode heat input with increasing helium content in the shielding gas indicates that the cathode voltage drop V_c increases with helium content.

5.8 Influence of ambient pressure

In Chapter 4 it was shown that arc voltage rises considerably with ambient pressure and that the relationship between arc voltage and ambient pressure can be described by

$$V_t = 10.8 + 2.1 p^{0.6} \qquad (5.16)$$

As the anode voltage drop and cathode voltage drop are independent of ambient pressure [5.12], the pressure dependence of the arc voltage is directly related to the pressure dependence of the voltage drop over the arc column. When increasing ambient pressure, three phenomena are believed to play a role in the arc column :

- an increase of the thermal conductivity, leading to an increase in conductive losses and a decrease in arc column diameter;
- a decrease of the electrical conductivity;
- an increase of convective heat loss due to the higher heat capacity per unit volume of the surrounding gas. This also decreases the arc column diameter.

These phenomena lead, separately or in combination, to an increase of the electric field strength in the arc column and, thus, to an increase of the total arc voltage.

The effectiveness of the column contribution to the anode heating can be calculated from the experimental results. Differentiation of equation (5.6) with respect to p was used to calculate the constant c_a, which leads to

$$\frac{\partial(Q_{am}/I)}{\partial p} = \frac{\partial V_a}{\partial p} + \frac{3k}{2e}\frac{\partial T_{pa}}{\partial p} + \frac{\partial(\phi/e)}{\partial p} + V_p\frac{\partial c_a}{\partial p} + c_a\frac{\partial V_p}{\partial p} \qquad (5.17)$$

Assuming the anode voltage drop V_a, the anode work function ϕ and the constant c_a to be independent of ambient pressure, equation (5.17) reduces to

$$c_a = \frac{1}{\left(\frac{\partial V_p}{\partial p}\right)}\left(\frac{\partial(Q_{am}/I)}{\partial p} - \frac{3k}{2e}\frac{\partial T_{pa}}{\partial p}\right) \qquad (5.18)$$

Values of the derivatives $\partial(Q_{am}/I)/\partial p$ and $\partial V_p/\partial p$ were obtained from the experimental results presented in § 4.4.1. Substitution of these values in equation (5.18) and disregarding the temperature term, leads to $c_a \approx 0.3$. Since the arc column temperature increases with increasing pressure [5.12], this is a maximum estimate. When comparing this result with the findings presented in § 5.5 ($c_a \approx 0.4$ to 0.7) it is evident that the assumptions made above can not all be valid.

The anode heat input and the anode heat input per ampere increase with increasing ambient pressure. This is a result of the increase in the arc column convective contribution, caused by the increase in arc column power, and of the increased thermal energy of the electrons due to the increase in arc column temperature. As shown in Chapter 4, anode heat input increases only slowly with increasing pressure. If 40 to 70% of the column power were transferred to the anode (as found in § 5.5), the anode heat input should rise much faster with increasing pressure than has actually been found. This indicates that the anode voltage drop V_a decreases with ambient pressure.

In Chapter 4 it was shown that melting efficiency increases both with increasing pressure and with increasing helium content in the shielding atmosphere. The increase of melting efficiency with pressure is associated with an increase of the workpiece

heat input and with constriction of the arc. Both effects lead to an increase in heat flux (heat input per unit surface area of the workpiece) and hence to a more efficient use of the heat entering the workpiece.

When the helium content in the shielding gas atmosphere is increased, the heat input to the workpiece increases as well. The heat flow distribution of the arc when using helium was shown to be highly dependent on the experimental parameters [5.13], but does not change considerably with changes in gas composition. It is therefore believed, that the increase in heat input is the main cause for the increase in melting efficiency.

References

5.1 L.E. Cram,
"A model of the cathode of a thermionic arc".
J. Physics D: Applied Physics 16 (1983), p 1643.

5.2 M. Ushio, A.A. Sadek, F. Matsuda,
"GTA Electrode Temperature Measurement and Its Related Phenomena".
IIW Doc 212-733-89 (1989).

5.3 D.M. Chen, E. Pfender,
"Two-temperature modeling of the anode contraction region of high-intensity arcs".
IEEE Transactions on Plasma Science PS-9 (1981), 4, p 265.

5.4 G.J. Dunn, C.D. Allemand, T.W. Eagar,
"Metal Vapors in Gas Tungsten Arcs: Part 1. Spectroscopy and Monochromatic Photography".
Metallurgical Transactions A 17A (1986), 10, p 1851.

5.5 W. Finkelnburg,
"Elektrische Bögen und thermisches Plasma" in :
"Handbuch de Physik", Band 22: "Gasentladungenm II".
Springer-Verlag, Berlin (1956).

5.6 P.A. Schoeck,
"An investigation of the anode energy balance of high intensity argon arcs in argon", in :
"Modern developments in heat transfer".
Academic Press, New York & London (1963).

5.7 G.N. Haddad, A.J.D. Farmer,
"Temperature measurements in gas tungsten arcs".
Welding Journal Research Supplement 64 (1985), 12, p 339s.

5.8 A.E. Guile,
"Processes at arc cathode roots on non refractory metals having films of their own oxide".
Conference on Arc Physics and Weld Pool Behaviour, London (1979).

5.9 D.C. Johnson, E. Pfender,
"The effect of low-ionisation-potential contaminants on thermal plasmas".
Plasma Chemistry & Plasma Processing 3 (1983), 2, p 259.

5.10 M.G. Sharapov,
"Effective temperature of the column of a constricted arc running in a mixture of argon and helium". Welding Production (1984), 8, p 1.

5.11 H.C. Ludwig,
"Plasma-energy transfer in gas-shielded welding arcs".
Welding Journal Research Supplement 48 (1975), 7, p 296s.

5.12 C.J. Allum,
"Effect of pressure on arcs".
Conference on Underwater Welding, Trondheim (1983).

5.13 N.S. Tsai, T.W. Eagar,
"Distribution of the heat and current fluxes in Gas Tungsten Arcs".
Metallurgical Transactions B, 16B, (1985), 12, p 841.

6. A heat flow model for the Gas Tungsten Arc

In the previous chapter, heat flow in the arc was discussed in a general way, with emphasis on the influence of the experimental parameters. In this chapter, the results will be evaluated separately for the arc column, the anode region and the cathode region. This leads to a comprehensive model which describes the heat flow in the arc column, cathode region and anode region.

6.1 Arc column

One of the two basic properties of the arc column is that it behaves like a plasma in Local Thermodynamic Equilibrium (LTE). This means that electrons and heavy particles are in mutual equilibrium and have equal temperatures. Secondly, no space charge exists in the arc column. This will result in an electric field strength which is independent of the axial position in the arc. Indeed, it was found that arc column field strength is only slightly influenced by arc length, which is demonstrated by the linear dependence of arc voltage on arc length. Furthermore, arc current, anode composition and cathode composition were shown to have no significant effect on the arc column field strength. Addition of small amounts of helium to argon shielding gas has no significant effect on arc column behaviour. Only when the argon content is insufficient to produce an electron density high enough to sustain the arc discharge, arc column temperature and field strength will increase in order to ionize helium atoms.

A significant part of the heat produced in the arc column is transferred to the anode. This occurs by radiation and convection. The radiative term is relatively small: the total radiative power per ampere, produced in the arc column, does not exceed

0.4 V, as has been shown by Allum [6.1]. If half of this radiative heat flow reaches the workpiece and half of the amount of heat reaching the workpiece is absorbed, the total radiative contribution will be 0.1 V at most. Thus, radiation can be neglected and the convective contribution dominates.

The convective contribution is very hard to estimate, since it requires knowledge of the convective boundary layer thickness in front of the anode and the physical properties of the plasma involved. The convective boundary layer thickness depends on the plasma jet velocity and on the viscosity and density of the plasma. Estimates of the physical properties of the plasma are hindered both by uncertainties in the temperatures involved and by a lack of knowledge about the temperature dependence of these properties. The plasma state at the anode (in particular its non-equilibrium state) can not be taken into account because of lack of data. Given estimates of the boundary layer thickness and of the physical properties of the plasma involved, the convective contribution to the anode heating can be calculated using the equations given in Chapter 2. In view of the foregoing, it is believed that these calculations are not particularly useful.

The data presented in § 5.5 show, that 40 to 70% of the heat, generated in the arc column, is transferred to the anode. In the case of a 3 mm, 100 A arc in argon, this leads to an anode heat input per ampere of 1 to 2 V. This contribution represents 15 to 25% percent of the total anode heat input, which is in agreement with the calculations of Schoeck [6.2].

In § 5.5 it was shown that the cathode heat input is independent of arc length. Therefore it is believed that there is no convective or radiative heat flow from the column to the cathode. This is plausible since the cathode surface area is so small that incident radiation will be negligible. With an electrode top angle of 60°, only about 8% of the radiation produced in the arc will reach the cathode. Given the same data as used above, the radiative contribution will be in the order of 0.02 V maximum. The convective contribution will be negligible since the plasma jet will inhibit the hot plasma to approach the cathode.

The extrapolation of arc voltage to zero arc length is assumed to yield the sum of the anode voltage drop and the cathode voltage drop. If both voltage drops are

independent of arc length, this assumption implies that the heat generated in the arc column is directly proportional to arc length. Thus, the arc column heat loss per ampere is expected to also show a proportional dependence on arc length. This was examined by plotting the arc column heat loss per ampere as a function of arc length. The arc column heat loss per ampere was derived by subtracting anode heat input per ampere and cathode heat input per ampere from the total arc voltage (see equation (5.8)). The results are given in Figs. 6.1 and Fig. 6.2 for arc currents from 50 to 200 A and for shielding gas compositions ranging from 100% argon to 100% helium. The column heat loss per ampere shows a linear relationship with arc length. The y-axis intercept, however, is in the order of 1.4 V, whereas it should be zero in case of a direct proportionality between arc column heat loss per ampere and arc length. In Chapter 5, similar results were presented for various cathode compositions and anode compositions (see Figs. 5.2 and 5.6).

The zero arc length discrepancy is thought to be due to the fact that the electric field strength is not constant, but instead is a function of the axial position in the arc. If the electric field strength is dependent on the axial position in the arc, extrapolation

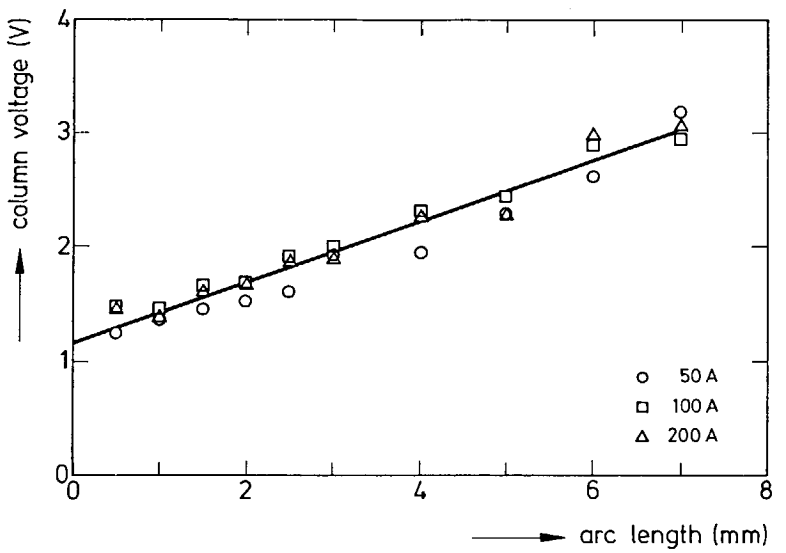

Figure 6.1: Column voltage (heat loss per ampere) as a function of arc length for arc currents of 50, 100 and 200 A.
Copper anode, 3.2 mm W-ThO_2 electrode in argon shielding gas.

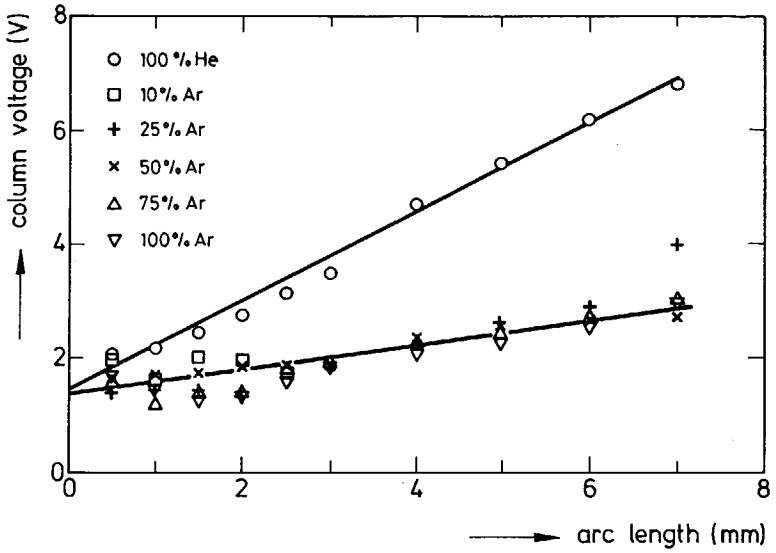

Figure 6.2: The column voltage (heat loss per ampere) as a function of arc length for various argon-helium shielding gas mixtures.
Iron anode, 3.2 mm W-ThO_2 electrode, 100 A arc current.

of the arc voltage to zero arc length does not yield the sum of the anode voltage drop and cathode voltage drop. Due to the constriction of the arc at the cathode, the electric field strength increases when the cathode is approached. It is reported that 0.5 mm in front of the cathode, a field strength as high as 2-3 V/mm may exist, whereas the average field strength in argon plasmas is only about 1 V/mm [6.3, 6.4].

The fact that field strength does not change abruptly when going from the cathode fall region to the arc column region is not surprising. Such an abrupt transition from the very high field strength in the cathode fall region (~10^7 V/m) to the relatively low field strength in the arc column (~10^3 V/m) could only exist if the space charge causing the cathode voltage drop would be confined within a layer of infinitely small thickness. The thickness of the boundary layer between the arc column and the cathode fall region was calculated to be about 0.1-0.5 mm [6.5]. The above also applies to the anode region. Boundary layer dimensions and field strengths are of the same order as those, found at the cathode.

The foregoing leads to a somewhat different description of the arc. This is visualized in Fig. 6.3, in which the potential is plotted as a function of the position

between the cathode and the anode. In this figure, the previously defined anode voltage drop and cathode voltage drop V_a and V_c are given together with the new anode voltage drop V_a^* and cathode voltage drop V_c^* which comprise the voltage drops over the boundary layers. These new voltage drops then include all space charge in front of the anode and cathode, but differ from the previously defined voltage drops in that not all of the heat, generated in these regions, is transferred to the anode and cathode.

As will be dealt with later in § 6.2, it is concluded that most of the column heat loss at zero arc length originates from the cathode boundary layer. In the anode boundary layer, a similar but much smaller heat loss occurs. The power lost in the cathode boundary layer is used to heat up the gas atoms entering the cathode region from room temperature to arc temperature and can be described by a term $\dot{m}C_p\Delta T_h$, in which $\dot{m}$, C_p and ΔT_h represent the mass flow of the shielding gas, its specific heat and the average temperature rise of the shielding gas. At an argon shielding gas flow rate of 10 l/min, an average temperature rise of 1000 K of the shielding gas would require about 150 W. At an arc current of 100 A, this represents a heat drain of 1.5 V.

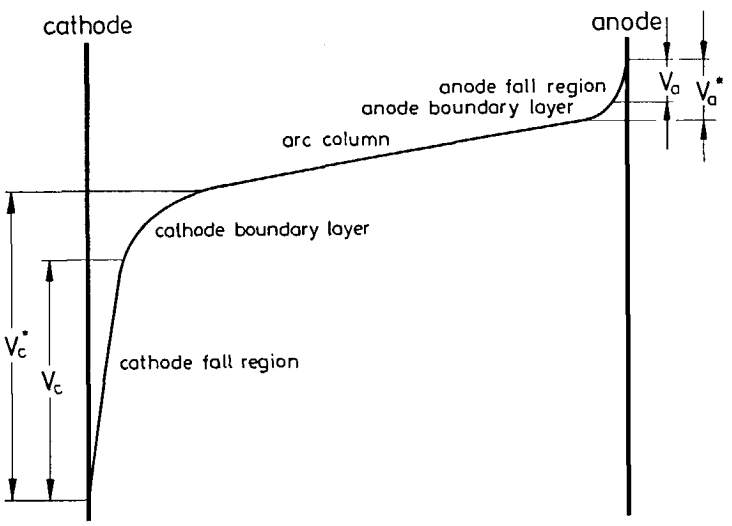

Figure 6.3: A modified model of the arc.

This shielding gas heating term can thus qualitatively explain the observed heat loss from the arc column at zero arc length.

The heat generated in the arc column and the cathode boundary region then consists of two terms. In the arc column, the heat production can be described by Q=lEI, in which l, E and I represent the arc length, arc column field strength and arc current. In the cathode boundary region, the heat production can be described by a term $Q=\dot{m}C_p\Delta T_h$.

Some of the heat thus generated will later be transferred to the anode. This heat transport mechanism has previously been described by a simple constant c_a. However, as the shielding gas heating term is virtually independent of arc length, whereas the arc column field strength term is directly proportional to arc length, it is much more appropriate to separate these terms in the heat flow balance. If a fraction f_a of the shielding gas heating term and a fraction c_a of the field strength term is transferred to the anode, the heat lost in the arc column can be written as

$$Q_p = (1-c_a)lEI + (1-f_a)\dot{m}C_p\Delta T_h \qquad (6.1)$$

A factor which can affect the result of the extrapolation of the column heat loss to zero arc length, is the dependence of the heat transfer from the column to the anode (represented by f_a and c_a in equation (6.1)) on arc length. At very low arc length, the plasma jet is much less intense and the anode thermal and convective boundary layer thickness will increase. The characteristic flow length L, used in the equations given previously in Chapter 2, will increase and this will lead to smaller heat flows at small arc length. Arc column temperature and arc column diameter will also be affected by arc length. Thus, the convective heat transport to the anode is a complex (most likely non-linear) function of arc length. Extrapolation of anode heat input to zero arc length will then result in an anode heat input in which the arc column contribution is still present.

It is believed, that errors in extrapolation of the field strength term are small since at low arc length (say 0.5 mm), the term lE only contributes about 0.5 V. Since the plasma jet velocity and the arc column diameter both decrease with decreasing arc length [6.6], the fraction f_a will decrease as well. At low arc length, practically none of the heat produced in the arc column and cathode boundary layer will be

transferred to the anode. Thus, errors in extrapolation of the column convective contribution to the anode heating are expected to be too low to account for the 1.4 V axis intercept of the column heat loss per ampere.

6.2 Cathode

In § 5.1, simple heat flow equations were given for the cathode (equations (5.3), (5.5) and (5.7)). These equations describe the heat flow balance over a volume which comprises the electrode and a small part of the arc (i.e. the cathode fall region). Thus, the terms in these equations do not relate exclusively to phenomena acting at the arc/electrode interface, but also to phenomena acting at the interface of the fall region and the arc column.

When considering the situation in the cathode region in more detail, it becomes clear that the energy, obtained by an electron crossing the cathode fall region (eV_c), does not contribute directly to the cathode heat input Q_c. Electrons emitted do not return to the cathode, but instead travel to the anode. For the same reason, the thermal energy obtained by the electrons when entering the arc plasma ($3kT_{pc}/2e$) does not directly lead to cooling of the cathode. Obviously, processes take place at the interface of the arc column and the cathode fall region which bridge this apparent discrepancy.

The processes taking place in this boundary layer can be described as follows. The energy obtained by the electrons in crossing the collision-free fall region is transferred into a drift velocity v_d, with $\frac{1}{2}m_e v_d^2 = eV_c$. This drift velocity should be distinguished from the thermal velocity v_t given by $\overline{\frac{1}{2}m_e v_t^2} = 3kT_e/2$. In the boundary layer separating the cathode fall region and the arc column, collisions between the electrons coming from the fall region and heavy particles take place. Due to these collisions, the drift velocity of the electrons is converted into a more random velocity distribution, which leads to an increase of the electron temperature. The electron energy flow is used to ionize atoms, to heat up atoms and ions and to produce radiation. The ions produced

travel to the cathode and transfer their energy at the cathode surface. This energy consists of the thermal energy of the ions and their kinetic energy obtained in crossing the cathode fall region. As the ions are neutralized at the cathode surface, the difference between their ionization energy and the cathode work function is also released. Part of the radiation produced in the boundary layer is absorbed by the cathode.

An important part of the atoms heated up by elastic collisions with electrons, however, will never reach the cathode as the plasma jet that develops due to the contraction of the arc at the cathode, transports atoms from the cathode region to the arc column. Atoms leaving the cathode region are replaced by atoms from the shielding gas which flows along the cathode. This results in a convective heat loss from the cathode boundary layer to the arc column.

Disregarding radiation, the energy transferred to the cathode is given by

$$Q_{cm} = \left(V_c + \frac{E_i - \phi_{Cu}}{e} + \frac{3k\Delta T_i}{2e} \right) I_i - \frac{\phi_{Cu}}{e} I_e \qquad (6.2)$$

In this equation, V_c, E_i, ΔT_i, I_i and I_e represent the cathode voltage drop, the ionization energy of the shielding gas, the temperature difference of the ions in the boundary layer and those at the cathode surface and the ion and electron current. Substituting V_c=7.5 V, E_i=15 eV, ΔT_i=10000 K, ϕ_{Cu}=4.4 eV and Q_{cm}/I=0.4 V (see § 5.2) leads to an ion current contribution of I_i/I≈0.20. This is in excellent agreement with calculations carried out by Hsu [6.5], who also arrived at an ion current contribution of 20%.

As already explained in § 6.1, heat losses from the cathode region to the arc column are not negligible. The plasma jet developing at the cathode transports atoms heated in the cathode boundary layer to the arc column. This convective heat loss from the cathode boundary layer can be described by a term $\dot{m}C_p\Delta T_h$, in which $\dot{m}$, C_p and ΔT_h represent the mass flow of the shielding gas, its specific heat and the average temperature rise of the shielding gas.

Although the physical processes occurring in the cathode region are accurately described by equation (6.2), this equation can not be used to calculate the cathode heat input, since the electron and ion current contribution needed for the evaluation of equation (6.2) can not be determined. It is therefore more appropriate to use similar equations as those given earlier in Chapter 5.

In describing the cathode heat flow it should be noted that not all the ions arriving at the cathode are produced in the cathode boundary layer. In the arc column, a fraction f_{pi} of the current is carried by ions. These ions transfer their ionization energy E_i from the arc column to the cathode. Thus, a term $f_{pi}E_i/e$, representing this extra energy, should be included in the cathode heat flow balance. A good estimate of the fraction f_{pi} is given by the ratio of the mobility of ions and electrons: $f_{pi}=\sqrt{(m_e/m_i)}$, in which m_e and m_i are the electron mass and ion mass. For argon, f_{pi} is about 0.4%, which results in an ion heat flow contribution of only 0.06 V. For helium, this contribution is about 0.3 V.

On the basis of the foregoing, a modified heat flow balance of the cathode region can be given[1)]

$$Q_{cm} = V_c^* I - \frac{3kT_{pc}}{2e} I - \frac{\phi_{Cu}}{e} I - \dot{m} C_p \Delta T_h + f_{pi} \frac{E_i}{e} I \qquad (6.3)$$

With the help of the model developed above, the increase in cathode voltage drop with decreasing arc current, described in § 5.4, can be explained. According to this model, ionization is a prerequisite for the cathode fall region. Ionization occurs when electrons leaving the cathode fall region collide with atoms present in the boundary layer. At decreasing arc current, the plasma temperature in the arc column decreases. Thus, the probability that electrons leaving the cathode fall region will ionize atoms in the plasma decreases as well. Electrons passing the cathode fall region gain an energy of eV_c, typically 8 eV. The ionization energy of argon is 15 eV. At low arc current the argon atoms are relatively immobile, i.e. have low temperature, and

---

1) In this equation, the work function of copper is used instead of the work function of the cathode material. This is necessary because this equation describes the heat flow to the calorimeter, thus including Peltier effects at the junction of the electrode and the copper torch (see Appendix B).

thermal ionization is less likely. Therefore, electron energy has to increase to sustain the ionization process. This is achieved by an increase in cathode voltage drop. Increasing the arc current will increase the temperature of the heavy particles and therefore promote thermal ionization. The cathode voltage drop thus decreases as arc current is increased.

A similar explanation can be given for the increase in cathode voltage drop when pure helium is used as shielding gas instead of argon. Due to the higher ionization energy of the helium atoms, the electron energy and thus the cathode voltage drop V_c has to increase to maintain a sufficient degree of ionization.

The cathode voltage drop can now be calculated using the experimental results presented in Chapter 3. Substitution of equation (6.1) in equation (6.3) and subsequent extrapolation to zero arc length leads to

$$V_c^* = \frac{Q_{cm}^{l=0}}{I} + \frac{1}{1-f_a}\frac{Q_p^{l=0}}{I} + \frac{\phi_{Cu}}{e} + \frac{3kT_{pc}}{2e} - f_{pi}\frac{E_i}{e} \qquad (6.4)$$

Values of the cathode voltage drop were calculated using equation (6.4) for various experimental conditions. In these calculations, data from Chapter 3 (values of Q_p/I and Q_{cm}/I extrapolated to zero arc length), a work function of ϕ_{Cu}=4.4 eV and an electron temperature of T_{pc}=10000 K were used. The fraction f_a was assumed to be zero. The results are given in Table 6.1 at the end of this chapter, together with calculated values of the anode voltage drop.

The cathode voltage drop is about 7.5 V for oxide-doped electrodes in argon, and is slightly higher when using oxide-doped electrodes in helium shielding gas and for pure tungsten electrodes in argon shielding gas.

6.3 Anode

In § 5.1, simple heat flow equations were given for the anode (equations (5.2), (5.4) and (5.6)). These equations represent the heat flow balance over a volume which comprises the anode and a small part of the arc (i.e. the anode fall region).

The processes taking place at the arc column-anode region boundary are much easier to understand than those described for the cathode region in § 6.2. The heat flow terms in equation (5.2) all contribute directly to the anode heating. Electrons entering the anode carry a thermal energy of $3kT_{pa}/2$ and a kinetic energy of eV_a due to the anode voltage drop and this energy is transferred directly to the anode. As electrons enter the anode, the work function of the anode material is also released.

However, as ions do not exist in the anode region, ionization must take place in the anode boundary layer. As the ions produced in the boundary layer move towards the cathode, this energy is transported from the anode region to the cathode region. Hence, ionization in the boundary layer accounts for a heat loss of $f_{pi}E_iI/e$. As this heat loss is fairly small, the difference between the anode voltage drop V_a and the voltage drop V_a^* which includes the anode boundary layer will also be small.

The convective and radiative contribution from the arc column to the anode heat input, represented in the heat transport equations in the previous chapter by a term c_aV_pI, is extremely difficult to assess. In fact, representation of this contribution by a term directly proportional to the arc column voltage drop V_p is an oversimplification of the actual situation. In § 6.1 the column heat production was subdivided into two terms, describing the heating of the shielding gas and the arc column Joule heating (equation (6.1)). A fraction f_a of the shielding gas heating term, and a fraction c_a of the Joule heating term was assumed to be transferred to the anode.

A modified anode heat flow balance can thus be written as[2)]

$$Q_{am} = V_a^* I + \frac{3kT_{pa}}{2e} I + \frac{\phi_{Cu}}{e} I + f_a \dot{m} C_p \Delta T_h + c_a |EI| - f_{pi} \frac{E_i}{e} I \qquad (6.5)$$

The electron associated heat input to the anode consists of terms related to the anode voltage drop, the thermal energy of the electrons and the work function of the anode. The anode voltage drop V_a^* comprises the small voltage drop in the boundary layer, in which heat is lost to the arc column due to ionization of the arc plasma.

In addition to the electron associated heat input to the anode, some of the power generated in the column is transferred to the anode by radiation and convection. Of all heating terms mentioned above, the anode voltage drop and the column convective contribution are the ones which are most difficult to assess.

To calculate the anode voltage drop from the anode heat input per ampere extrapolated to zero arc length, a similar equation as equation (6.4) can be used. Combination of equations (6.1) and (6.5) gives

$$V_a^* = \frac{Q_{am}^{l=0}}{I} - \frac{f_a}{1-f_a} \frac{Q_p^{l=0}}{I} - \frac{\phi_{Cu}}{e} - \frac{3kT_{pa}}{2e} + f_{pi} \frac{E_i}{e} \qquad (6.6)$$

As already mentioned in § 6.1, the factor f_a which describes the fraction of the shielding gas heating term which is transferred to the anode, decreases with arc length, f_a is taken to be zero.

A realistic estimate of the electron temperature in front of the anode is 10000 K. The thermal energy of the electrons entering the anode then contributes 1.3 V to the anode heat input per ampere. The electron temperature clearly depends on welding parameters such as arc current, arc length and shielding gas composition. The maximum error in this estimate is about 5000 K, or 0.65 V.

[2)] In this equation, the work function of copper is used instead of the work function of the anode material. This is necessary because this equation describes the heat flow to the anode calorimeter, thus including Peltier effects at the junction of the workpiece and the copper extremities of the calorimeter (see Appendix B).

Taking all this into account, an estimate of the anode voltage drop can be made using the data presented in Chapter 3. The thus obtained values of the anode voltage drop are given in Table 6.1 together with the calculated values of the cathode voltage drop, extrapolated arc voltage, anode heat input per ampere, cathode heat input per ampere and column heat loss per ampere.

It can be seen from this table that the anode voltage drop is in the order of 1 V in argon shielding gas and 3 to 5 V in helium shielding gas. The low anode voltage drop calculated in the case of iron and steel workpieces is thought to be due to the inaccurate extrapolation of the arc voltage and anode heat input. Because of the formation of a weld pool which protruded from the workpiece, the actual arc length is not equal to the preset arc length used in the extrapolations.

Table 6.1: Calculated values of the voltage drops V_a^* and V_c^*.

cathode	anode	I (A)	gas (%He)	$V_t^{I=0}$ (V)	$Q_{am}^{I=0}/I$ (V)	$Q_{cm}^{I=0}/I$ (V)	V_c^* (V)	V_a^* (V)
W-ThO_2	Cu	50	0	8.8	7.0	0.67	7.4	1.4
		100		8.4	6.6	0.52	7.4	1.0
		200		9.0	7.2	0.55	7.4	1.6
W-ThO_2	Cu	100	0	8.4	6.6	0.52	7.4	1.0
			25	8.8	7.1	0.48	7.3	1.5
			50	9.4	7.5	0.46	7.5	1.9
			75	10.8	8.7	0.48	7.7	3.1
			100	12.5	10.3	0.64	7.6	4.9
W-ThO_2	Fe	100	0	7.9	6.0	0.50	7.5	0.4
			25	7.8	6.1	0.58	7.3	0.5
			50	9.2	7.0	0.61	7.8	1.4
			75	10.6	8.7	0.68	7.5	3.1
			100	11.2	8.6	0.93	8.0	3.2
W-ThO_2	Fe 510	100	0	7.2	5.4	0.55	7.4	-0.2
W-ThO_2	W	100	0	8.0	6.4	0.44	7.2	0.8
W-La_2O_3				8.0	6.5	0.37	7.1	0.9
W-Y_2O_3				8.2	6.9	0.42	6.9	1.3
W				9.5	7.3	0.72	7.8	1.7

References

6.1 C.J. Allum,
"The characteristics and structure of high pressure (1-42 bars) gas tungsten arcs".
Ph. D. thesis at the Cranfield Institute of Technology, Cranfield, 1982.

6.2 P.A. Schoeck,
"An investigation of the anode energy balance of high intensity argon arcs in argon", in :
"Modern developments in heat transfer".
Academic Press, New York & London, 1963.

6.3 H.N. Olsen,
"Temperature measurements in high current arc plasmas".
Am. Phys. Soc. Bulletin (1957), 1, p 81.

6.4 D.L. Evans, R.S. Tankin,
"Measurement of emission and absorption of radiation by an argon plasma".
Phys. Fluids 10 (1967), 6, p 1137.

6.5 K.C. Hsu, E Pfender,
"Analysis of the cathode region of a free-burning, high intensity argon arc".
Journal of Applied Physics 54 (1983), 7, p 3818.

6.6 N.S. Tsai, T.W. Eagar,
"Distribution of the heat and current fluxes in Gas Tungsten Arcs".
Metallurgical Transactions B 16B (1985), 12, p 841.

6.7 G.N. Haddad, A.J.D. Farmer,
"Temperature measurements in gas tungsten arcs".
Welding Journal Research Supplement 64 (1985), 12, p 339s.

A. Heat transport in the calorimeter

The workpiece and electrode calorimeter described in Chapter 3 are supposed to carry off all the heat transferred by the welding arc. If heat losses occur, this will have a direct bearing on the results obtained in the experiments. To minimize heat losses, both calorimeters were cooled with ample water so that the temperature of the calorimeter was sufficiently low. Both calorimeters were not thermally isolated. For the torch and the bottom of the workpiece calorimeter, this was found to be unnecessary. For the workpiece top, isolation is impossible due the presence of the arc. Calculations were performed to validate the neglect of convective and radiative heat losses from the calorimeters. For the torch calorimeter, an analytical approach of the heat loss is given in § A.1. For the workpiece calorimeter, both an analytical (§ A.2.1) and numerical (§ A.2.2) approach was followed.

A.1 The torch calorimeter

The torch calorimeter was made of a large copper body, shown in Fig. A.1. Heat loss from the torch body occurs through :

a) convection to the shielding gas which flows directly around the water compartment;
b) convection from the torch perimeter to the surrounding gas;
c) convection from the hot electrode to the shielding gas;
d) radiation, especially from the hot electrode.

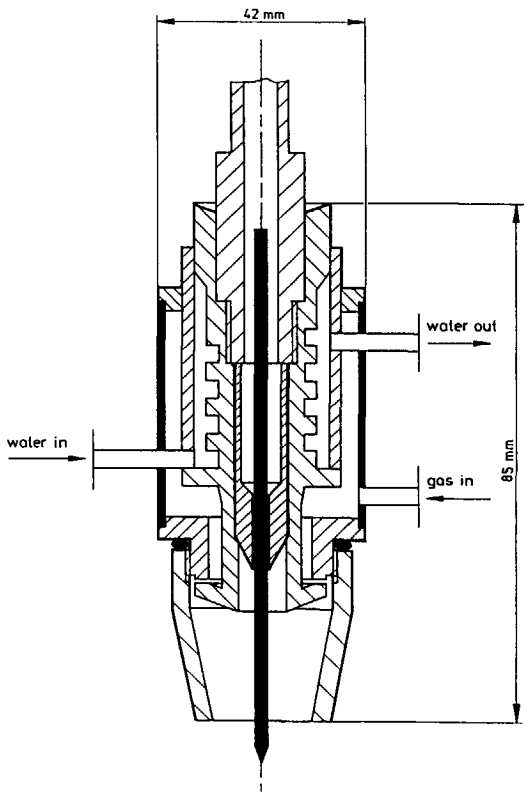

Figure A.1: Schematic representation of the welding torch used.

ad (a)

The total shielding gas flow rate was 10 l/min. If the argon shielding gas would rise 1°C in temperature, the associated heat flow would be $\Delta T\ \dot{m}\ C_p = 0.15$ W. At an arc current of 100 A, the cooling water temperature rise was about 3°C. If the shielding gas would reach the same temperature as the cooling water, a heat loss of only 0.45 W would occur.

ad (b)

As the torch is made of copper, the temperature at the torch surface will be approximately the same as the temperature of the cooling water. Due to the small temperature rise of the cooling water, the heat loss to the surrounding air is very small. The heat transfer coefficient h can be calculated from the Nusselt number Nu. For convective heat transport from a vertical wall [A.1], the following equation is valid

$$\frac{hL}{\lambda} = Nu = 0.55(Gr\ Pr)^{0.25} \qquad (A.1)$$

with Gr the Grashof number which can be written as

$$Gr = \frac{L^3 g}{\nu^2}\frac{\Delta\rho}{\rho} \qquad (A.2)$$

and Pr the Prandtl number Pr which has a value of about 0.7 for air at 300 K.

In these equations, L is the calorimeter height, g the gravitational constant, λ the thermal conductivity of air, $\Delta\rho$ the density difference of the air at the calorimeter temperature and that of the surrounding air ρ, and ν the kinematic viscosity. With L=0.06 m, g=10 m/s^2, λ=0.026 W/mK, $\Delta\rho/\rho=\Delta T/T$=0.01, and ν=1.3 10^{-5} m^2/s, the Nusselt number and heat transfer coefficient can be calculated: Nu=9.5, h=4.1 W/m^{2}K.

The total surface area of the calorimeter is about 75 cm^2. With a temperature rise of the calorimeter of 3°C, and a heat transfer coefficient of 4.1 W/m^{2}K, the heat loss will be 0.09 W.

ad (c,d)

As was calculated by Cram [A.2], the convective and radiative heat loss from the tungsten electrode itself is in the order of 5 W for an arc current of 100 A. This heat loss can not be avoided, since the high temperature of the electrode is essential for the operation of the arc.

It is concluded that at an arc current of 100 A the total error in measurement of the torch calorimeter heat input does not exceed 6 W. This can be significant compared to the cathode heat input of 40 to 70 W, but is negligible when compared to the arc power of about 1100 W.

A.2 The workpiece calorimeter

The workpiece calorimeter consists of a stainless steel compartment, on which the workpiece could be mounted by four steel clamps. The bottom surface of the calorimeter has a uniform temperature, so that approximations of the heat loss can be made using normal heat transport equations. This will be discussed in § A.2.1. The top surface of the calorimeter is formed by the workpiece, and has a temperature ranging from 20°C at the edge to about 2500°C underneath the arc. In view of this temperature gradient, radiation and convection to the surroundings can best be calculated using a numerical approach. This will be described in § A.2.2.

A.2.1 Analytical modelling of the workpiece heat transport

In this section, the heat loss from the bottom part of the calorimeter is estimated. The temperature of the bottom part of the calorimeter is taken to be equal to the temperature of the cooling water, which is a maximum estimate.

The heat transfer coefficient for convective heat transport from a horizontal plane is given by [A.1]

$$Nu = \frac{hL}{\lambda} = 0.17\ (Gr\ Pr)^{0.33} \qquad (A.3)$$

Taking $\Delta\rho/\rho=\Delta T/T=0.03$ (10°C temperature difference), the characteristic flow length L=0.18 m and the other constants as in § A.1, we arrive at a heat transfer coefficient of $h=4.4\ W/m^2K$.

The bottom surface of the calorimeter has a diameter of 18 cm, and a surface area of 0.025 m^2. With a temperature difference of 10°C, the total heat loss would be 1.1 W. This is an upper estimate, since equation (A.3) is valid for convection above a horizontal plane, a situation in which buoyancy promotes convective heat transport. It is concluded, that the heat loss from the bottom of the calorimeter is small

compared to the anode heat input, which is typically 800 W at an arc current of 100 A and an arc length of 3 mm.

A.2.2 Numerical modelling of the workpiece heat transport

Modelling

For the workpiece at the top of the calorimeter, a finite difference program was written in Turbo Pascal to assess the radiative and convective heat losses. A radially symmetrical grid of 25x25 elements was used. In the through-thickness (z-) direction, elements were spaced equidistantly, in the radial (r-) direction, elements were spaced exponentially. The smallest element (at r=0) was 0.4 mm x 0.4 mm in size.

In this program, five heat transport mechanisms were taken into account.

(a) Firstly, the arc heat input was assumed to take place at the centre of the workpiece, with a conical heat flux distribution having a radius of 3 mm. Arc heat input was taken to be 500, 1000 and 2000 W, typical for the range of arc currents used in the experiments (50 to 250 A).

(b) The heat transport in the workpiece takes place by normal conduction. The thermal conductivity was described by a temperature dependent function and rises steeply as the melting point of the workpiece is reached.

The temperature of any element in the workpiece was calculated from its enthalpy. The enthalpy function was calculated from the temperature dependent specific heat, taking into account the latent heat of melting.

(c) Heat transport to the water underneath the workpiece was calculated using a position dependent heat transfer coefficient. Heat transport due to forced convection along a flat plate can be described by [A.1]

$$Nu = \frac{hL}{\lambda} = 0.33\ Re^{0.5}\ Pr^{0.33} \qquad (A.4)$$

in which the Reynolds number is given by

$$Re = \frac{vL}{\nu} \qquad (A.5)$$

with L the characteristic flow length, v the water flow velocity and ν the kinematic viscosity. The heat transfer coefficient h calculated from (A.4) is dependent on the position, i.e. close to the centre of the calorimeter, the water flow velocity and the Reynolds number Re are high, whereas at the extremities both are very low.

The heat transfer coefficient calculated from (A.4) was multiplied by a fit-factor. This fit-factor was chosen in such a way, that the calculated temperature profile of the top surface matched the temperature profile measured during experiments using a chromel-alumel thermocouple. Water temperature was assumed to be constant at 20°C.

(d) Convective heat transport to the air above the workpiece was calculated using a temperature dependent heat transfer coefficient. The heat transport to the air above the workpiece is strongly dependent on the temperature of the workpiece. It was calculated from equation (A.3), that the heat transfer coefficient increases with increasing workpiece temperature. At 2400°C, for example, the heat transfer coefficient was calculated to be 18 W/m^2K, whereas it is only 4 W/m^2K at 20°C. The air temperature was assumed to be constant (20°C). Underneath the arc (3 mm width), no convective heat loss to the hot arc plasma takes place.

(e) Radiative heat transport to the surrounding was described by the Stefan-Boltzmann law, with an emission coefficient of 0.4.

Results

Calculations were performed for iron, copper and tungsten workpieces of 10 mm thickness with heat inputs of 500, 1000 and 2000 W. The heat transfer coefficient for heat transport to the cooling water was multiplied by a fit-factor 4. This yielded realistic temperature profiles at the workpiece top for all workpieces. A typical temperature distribution at the top and bottom surface of a copper workpiece is given in Fig. A.2. Radiation proved to be the most important source of heat loss for the iron workpiece. For copper and tungsten workpieces, convection was the main source of heat loss. In Table A.1, the calculated maximum temperature at the workpiece top surface and the heat loss are given percent wise for anode heat inputs of 500, 1000

and 2000 W. The table shows, that heat losses amount to 1.1-2.4% of the total heat entering the iron workpiece. These heat losses will be smaller when using copper or tungsten workpieces, or workpieces with reduced thickness, since the surface temperature of those workpieces will be lower.

Table A.1: Calculated maximum temperature and heat loss from the workpiece top surface.

anode material:	Copper		Iron		Tungsten	
anode heat input (W)	T_{max} (°C)	heat loss (%)	T_{max} (°C)	heat loss (%)	T_{max} (°C)	heat loss (%)
500	151	1.0	1375	1.1	329	0.9
1000	286	0.7	1881	1.4	697	0.7
2000	563	0.6	2644	2.4	1554	0.7

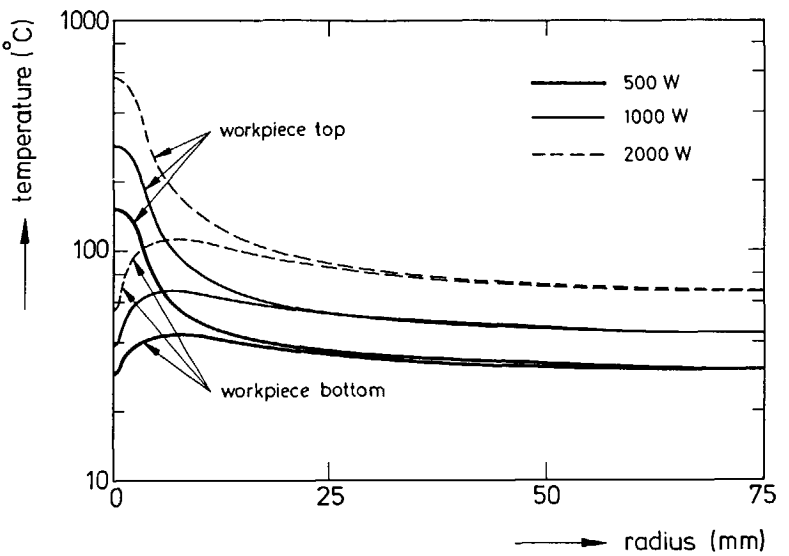

Figure A.2: Calculated temperature distribution of the top and bottom surface of a copper workpiece of diameter 150 mm and thickness 10 mm for heat inputs of 500, 1000 and 2000 W.

A.3 Conclusions

From the above, the following conclusions can be drawn.

- The heat loss from the torch is relatively low. Most of the heat loss is due to radiation and convection from the tungsten electrode. This heat loss can not be avoided. At an arc current of 100 A, radiative and convective heat losses are in the order of 6 W. This is about 12% of the total heat entering the electrode.
- The heat loss from the workpiece calorimeter is radiation dominated for iron workpieces and convection dominated for copper and tungsten workpieces. Radiative and convective heat losses from iron workpieces can be as high as 2.4% of the workpiece heat input. When using copper and tungsten workpieces, however, the total heat loss does not exceed 1% of the workpiece heat input.
- The total heat loss from torch and workpiece calorimeter is relatively low. At an arc current of 100 A, a maximum of about 30 W is lost. On a voltage scale, this amounts to 0.3 V.

References

A.1 W.J. Beek & K.M.K. Muttzall,
"Transport Phenomena".
John Wiley & Sons, London (1975).

A.2 L.E. Cram,
"A model of the cathode of a thermionic arc".
J. Physics D: Applied Physics 16 (1983), p 1643.

B. Thermoelectric effects

Thermoelectric effects are electric effects which occur when temperature gradients are present, or vice versa. Basically, there are three thermoelectric effects: the Peltier effect, the Thomson effect and the Seebeck effect.

In the following section, the fundamentals of thermoelectricity are described briefly. Next, the relationship between these three thermoelectric effects is discussed. Finally, the implications for the calorimetric measurements during arc welding will be addressed.

B.1 Theory of thermoelectricity

The Peltier, Thomson and Seebeck effects all find their origin in the Fermi energy level of materials, and in the temperature dependence of this Fermi energy level. Hence, all thermoelectric properties are bulk properties. Although the Seebeck and Peltier effects can only be measured when two or more materials are involved, the basic thermoelectric properties are dependent only on the material itself. As the Fermi energy level and work function are of prime importance to the understanding of thermoelectricity, these will be dealt with first.

Definition of the Fermi energy level and the work function

In metals, valence electrons become conduction electrons and move about freely through the volume of the metal. These electrons form the free electron Fermi gas. The electrons in this electron gas can only have energy states which obey distinct laws which relate their wave function to the metal-ion properties and the lattice spacings of the metal. The Pauli exclusion principle then prescribes that no two electrons can

occupy identical states. Hence, not all electrons have identical energies and an electron energy distribution exists. A typical energy distribution function is given schematically in Fig. B.1. At absolute zero, there is a distinct maximum energy level for the electrons given by the solid curve in Fig. B.1. When increasing the temperature, only electrons close to this maximum energy level are affected, giving rise to an energy distribution represented by the dashed curve in Fig. B.1. The Fermi-energy level E_F is defined as the energy level of the electron state at which the chance of occupation is 0.5. The Fermi energy level is only slightly influenced by temperature.

The Fermi energy level and the work function are two material properties which are closely related. The work function ϕ is defined as the difference in energy between an electron at rest in vacuum and an electron at the Fermi energy level. This is illustrated in Fig. B.1. Work functions can be measured by determination of the threshold energy for photoelectric emission. If $h\omega$ is the energy of an incident photon, then the Einstein equation gives $h\omega=\phi+E$, in which E is the kinetic energy of the emitted electron.

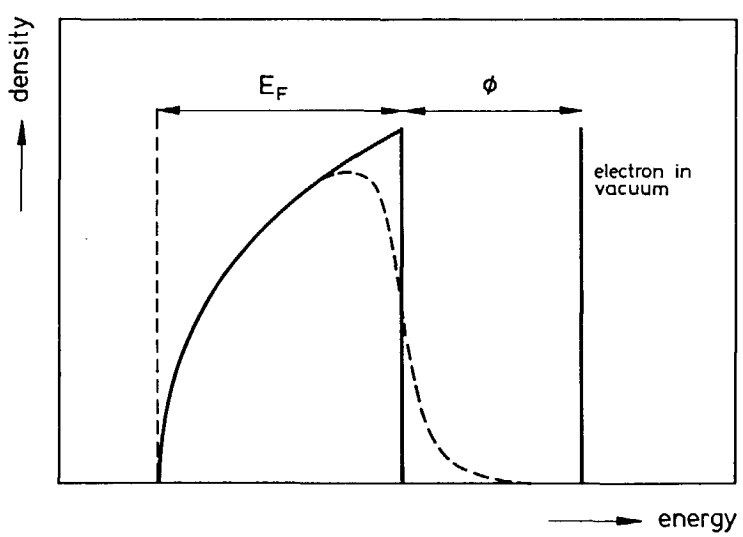

Figure B.1: Density of single-particle states as a function of energy for a free electron gas (from [B.1]).

The Peltier effect

If an electron is transported from a material with a high work function to a material with a low work function, the difference in work function appears as the Peltier heat. When the current flow is reversed, a cooling effect will occur. This Peltier cooling is sometimes used in refrigerators. The Peltier coefficient π is expressed in volts.

The Thomson effect

If a material is heated, the energy distribution of the conduction electrons within the material will change (see Fig. B.1). Electrons travelling through a temperature gradient will thus gain or lose energy, and can be perceived as having a specific heat. This Thomson effect is usually small, since only electrons with energies close to the Fermi energy level can gain energy and contribute to the Thomson effect. In semiconductors, conduction by positive holes can give rise to a negative Thomson coefficient. Phonons (energy-quantized elastic waves within the lattice) also contribute to the Thomson effect. Phonons can be produced as a result of collisions of electrons with the lattice (phonon-drag). The Thomson coefficient μ is expressed in volts per Kelvin.

The Seebeck effect

The Seebeck effect is well known as its principle is widely used in the measurement of temperature by thermocouples. If two materials are joined, electrons from the material with the highest thermodynamic potential will cross the interface to the material in which electrons have the lowest thermodynamic potential. This gives rise to a Seebeck potential. This Seebeck potential, however, can only be measured when two junctions of different temperature are involved. The Seebeck coefficient S of a material, also known as the absolute thermoelectric power, is expressed in volts per Kelvin.

B.2 Relationship between the three thermoelectric effects

In Fig. B.2, a simple circuit is shown, in which all three thermoelectric effects occur. In this figure, a current supply is present at point D. Between points A and B, a bar of material (2) is included in a circuit that otherwise consists of material (1). A temperature gradient exists over this bar, as well as over the section B-C ($T_A=T_C>T_B$).

When a current I is passed through this circuit, a Peltier effect will take place at the junctions A and B. This Peltier effect will give rise to a heat production Q at junctions A and B

$$Q_A = \pi_{12}(T_A)It \quad ; \quad Q_B = -\pi_{12}(T_B)It \tag{B.1}$$

In these equations, π_{12} ($=\pi_1-\pi_2$) represents the Peltier coefficient of the material combination (1)/(2) and t represents time.

The Thomson effect will occur in the sections A-B and B-C. The Thomson heat Q produced in sections A-B and B-C will be

$$Q_{AB} = +\int_{T_B}^{T_A} \mu_2(T)It\,dT \quad ; \quad Q_{BC} = -\int_{T_B}^{T_A} \mu_1(T)It\,dT \tag{B.2}$$

in which μ is the Thomson coefficient and the suffixes 1 and 2 represent the materials (1) and (2).

At point D, the Seebeck effect can be observed, as the circuit D-A-B-C-D consists of two thermocouples (1-2) and (2-1) at temperature T_A and T_B. This Seebeck potential U_S is equal to

$$U_S = \int_{T_B}^{T_A} S_{12}(T)\,dT \tag{B.3}$$

in which $S_{12}(T)$ ($=S_1(T)-S_2(T)$) is the Seebeck coefficient of a material junction (1)/(2) at temperature T in volts per Kelvin.

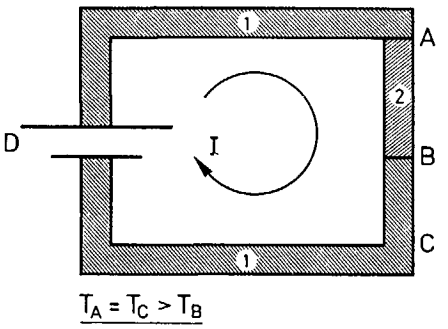

Figure B.2 : Sample circuit in which the Peltier effect, Thomson effect and Seebeck effect all play a role.

The overall balance of heat should comply with Ohm's law, i.e. $U_D It = I^2 Rt$, in which U_D is the voltage measured at point D. Taking into account the thermoelectric effects just described, the heat balance can be written as

$$U_D It = I^2 Rt + \left(\pi_{12}(T_A) - \pi_{12}(T_B) + \int_{T_B}^{T_A} \left(\mu_2(T) - \mu_1(T)\right) dT \right) It \qquad (B.4)$$

As is clear from this equation, there is an apparent deviation from the law of Ohm, represented by the term in brackets. This term represents the Seebeck potential U_S which acts against the supplied voltage U_D, or

$$U_S = \pi_{12}(T_A) - \pi_{12}(T_B) + \int_{T_B}^{T_A} \left(\mu_2(T) - \mu_1(T)\right) dT \qquad (B.5)$$

Thermodynamic description of thermoelectric effects

In equation (B.5), a distinct relationship between the Peltier, Thomson and Seebeck effects is given. There exist, however, relationships between the individual thermoelectric effects, generally known as the Kelvin equations

$$\mu = T\frac{\partial S}{\partial T} \tag{B.6}$$

$$\pi = TS \tag{B.7}$$

In these equations, the Thomson coefficient, Peltier coefficient and the Seebeck coefficient can be seen as the specific heat of the electrons, the enthalpy change due to a change of state, and the entropy function of the electrons. This is best demonstrated by a comparison with classic thermodynamic theory.

In this thermodynamic analogon, the Seebeck effect is represented by a "transport entropy function" S(T,p) where T and p represent temperature and pressure, such that when an electric charge q passes between any two points A and B of a circuit in the direction A→B, the entropy absorbed (reversibly) is given by $q\cdot\{S(T_B,p_B)-S(T_A,p_A)\}$.

It follows immediately that the Peltier heat π_{12} developed per unit charge at the isothermal junction of conductors 1 and 2 is given by $\pi_{12}=-T(S_2-S_1)=TS_{12}$, or $\pi=TS$, where $\pi_{12}=\pi_1-\pi_2$ and $S_{12}=S_1-S_2$. The Peltier heat should thus be regarded as the enthalpy change occurring when electrons change their entropy state. The analogon in classic thermodynamic terms can be written as: $dH=TdS+VdP$, $\Delta H_p=T\Delta S_p$.

Secondly, for a single conductor under a temperature gradient dT/dx, the Thomson heat μ can be deduced to be $\mu=T(dS/dT)$. This follows from basic thermodynamics in which the specific heat C_p follows from: $C_p=dH/dT=TdS/dT$.

Finally, it can be shown that in a circuit as in Fig. B.2 the Seebeck potential U_S is indeed given by $S_{12}(T_A-T_B)$. The Seebeck coefficient S can thus be regarded as the transport entropy of electric charge.

From the above, it should be clear that thermoelectric effects are reversible, i.e. on reversing the current, all heat flows originating from these thermoelectric effects will change sign. This also means, that there is no net effect on heat production in the system as a whole. In Fig. B.2, the overall heat balance still complies with the law of Ohm, as can be concluded from equation (B.4). Local heat production can, however, change due to Peltier and Thomson effects.

B.3 Implications for the calorimetric measurement of heat flow during arc welding

Due to the high current and temperature gradients, thermoelectric effects can play a significant role in calorimetric measurements of the heat transport during the arc welding process. In Fig. B.3, the places where these effects are expected to occur are indicated.

The Thomson effect is occurring where electrons travel through a temperature gradient. This does not only apply to the electrode and workpiece, but also to the arc plasma. The Thomson coefficients of the materials used in the calorimeter are a function of temperature and are much smaller than the Thomson coefficient of free electrons in a vacuum (with a Thomson coefficient of $\mu_p=3k/2e$ V/K), since in a metal most electrons are bound to specific energy levels. Generally speaking, Thomson coefficients of metals are in the order of 1 to 10% of the Thomson coefficient in vacuum.

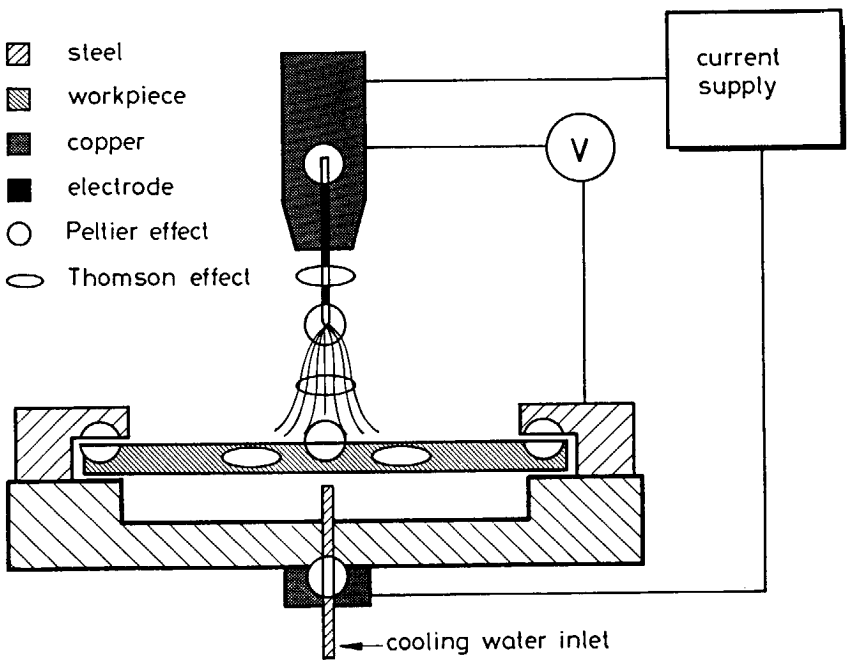

Figure B.3 : Thermoelectric effects in the calorimetric setup.

As shown in Fig. B.3, Peltier effects occur at all material junctions, including the arc/electrode interfaces, where electrons enter and leave the arc. The work function of electrons in the arc is zero. As the Fermi energy level of any material is a function of temperature, the work function and thus the Peltier effect will change with temperature.

Data on the Peltier coefficient, Seebeck coefficient and Thomson coefficient are not available for all the materials and temperature ranges in question. For instance, work functions of pure metals are usually measured at room temperature. Seebeck coefficients are only known for commercially employed thermocouple materials and pure metals. Data on Thomson coefficients are also very scarce. The individual contribution of either of these three processes is thus unknown. However, because of their relationship described in the previous section, the total effect of these three thermodynamic effects can be determined

As has been stated in the previous section, the first law of thermodynamics applies to thermoelectric effects. Because thermoelectric effects are reversible, only the initial and final state of the electrons is of importance in determining the heat flow associated with the overall process of charge transport, and the path followed is of no effect. This has the following bearing on the heat transport formulations for the calorimetric setup.

- An electron entering the calorimeter at the cathode side enters the copper torch body at room temperature. The electron finally arrives in the arc plasma at a temperature of T_{pc}. If the electron was emitted from the copper torch body immediately upon entering and subsequently heated to obtain the plasma temperature T_{pc}, the electron would gain an energy $Q=\phi_{Cu}+e\mu_p T_{pc}=\phi_{Cu}+3kT_{pc}/2$.

  As the followed path is of no effect, the same heat Q is gained by the electron in the realistic situation in which the electron enters the oxide-doped tungsten electrode via the copper torch, travels through a temperature gradient and is emitted at the electrode tip, which has a temperature of about 3000 K, to the plasma at temperature T_{pc}.

The energy Q is of course taken from the cathode calorimeter. A similar heat balance applies for the anode, but in this case the electron energy is transferred to the anode.

- Only when the local heat balance at the electrode/arc interface is being assessed, it is necessary to use the temperature and composition dependent work function of the electrode in question. This can be of some importance, since in particular Peltier effects are taking place at remote locations.

  This is especially relevant for the cathode, as the thermal load at the cathode tip is of prime importance to the cathode erosion.

References

B.1 C. Kittel,
"Introduction to solid state physics", 6th ed.
John Wiley & Sons, New York (1986).

B.2 R. Kronig,
"Leerboek der Natuurkunde".
Scheltema & Holkema, Amsterdam (1946).

B.3 K.C. MacDonald,
"Thermoelectricity: an introduction to the principles".
John Wiley & Sons, New York (1962).

Summary

In this thesis, a study is presented which was carried out to obtain insight into the basic heat flow processes during Gas Tungsten Arc welding. Understanding the basic heat transport processes in the arc is of importance in assessing the relationship between welding parameters and weld quality. With the increasing interest in mechanization and automation of the welding process, this relationship has become the subject of intensified research.

Calorimetric experiments were performed to determine the influence of welding parameters such as cathode composition, anode composition, arc current, arc length, polarity, shielding gas flow rate and shielding gas composition on the heat flow to the anode and the cathode. In a pressure vessel, the influence of ambient pressure and shielding gas composition was determined in experiments using the thermal cycle of the workpiece to calculate the workpiece heat input.

The welding arc may be divided into three zones. The anode fall region and cathode fall region are characterized by a relatively high potential drop (1-8 V) over a very small region (~ 1 μm). The arc column comprises the remainder of the arc (several mm's), and has an electric field strength not higher than a few V/mm.

Of the three regions mentioned, the anode fall region and cathode fall region are the least well understood. The heat transport to the anode consists of contributions related to the anode voltage drop, the anode work function, the thermal energy of the electrons entering the anode, and convective and radiative heat transport processes. The heat transport to the cathode can be described in similar terms. In the case of the cathode, however, the emission and subsequent heating of electrons constitutes a heat drain. The cathode voltage drop and the convection and radiation from the arc plasma contribute to the heat production in the cathode region.

It was shown, that the heat transport models presented in literature do not take proper account of thermoelectric effects. The influence of the addition of oxides with low work functions to the cathode, for instance, is poorly understood. Furthermore, Thomson effects in the materials involved are usually ignored.

It was found that about 75 to 80% of the gross arc power is transferred to the anode. The results also indicate, that the anode voltage drop is in the order of 1 V in argon shielding gases, and in the order of 4 V in helium shielding gas. This represents about 15% and 40% respectively of the anode heat input. The convective contribution of the arc column is substantial, i.e. convective heat transport from the arc plasma to the anode accounts for 10 to 20% of the anode heat input. The electron thermal contribution is of the same order of magnitude. The major contribution to the anode heat input, however, is due to the impinging electrons releasing an energy equal to the work function of the anode material. This accounts for up to 60% of the anode heat input.

Anode composition and anode melting were shown not to affect the heat transport processes mentioned above. Increasing arc length increases the anode heat input because of the increase in the convective heat transport. The anode heat input shows an almost proportional dependence on arc current, indicating that the anode voltage drop is little affected by arc current. When increasing ambient pressure, the anode heat input rises because of the increased convective contribution of the arc column. Increasing ambient pressure also leads to a contraction of the arc. This results in a significantly increased weld penetration.

Due to the substantial cooling effect of the electrons emitted from the cathode surface, less than 10% of the gross arc power is actually transferred to the cathode. This is advantageous, since erosion of the electrode in GTA welding, incited by the high temperature of the electrode tip, is detrimental to welding productivity. The results obtained show that the convective and radiative contribution of the arc column to the cathode heating is negligibly small. The cathode voltage drop is about 7 V in argon shielding gas and is slightly higher when helium shielding gas is used.

In practice, oxides are added to the tungsten electrode to improve welding characteristics and reduce electrode erosion. This favourable effect is attributed to the low work function of the oxides, which increases the thermionic emission of electrons from the electrode tip. It was shown that the low work function of these oxides has no effect on the heat balance equation of the cathode as a whole (including the torch).

However, the low work function does affect the current density at the electrode tip, thus decreasing the cathode voltage drop and the thermal load at the electrode tip.

Arc length was shown to be of no effect on the cathode heat input. When using pure helium as a shielding gas, heat input is considerably higher than in the case of welding in argon or argon/helium shielding gas mixtures. This is due to a higher cathode voltage drop when using helium shielding gas. The cathode voltage drop was also found to increase when arc current was decreased below 50 A.

In the arc column, heat is lost by radiation, convection and conduction. As shown by the results obtained in the calorimetric experiments, the heat lost in the arc column has a linear dependence on arc length. In contrast to assumptions usually made in literature, however, the arc column heat loss does not vanish when arc length approaches zero. At an arc current of 100 A, for example, extrapolation of the heat loss in the arc column to zero arc length leaves about 140 W. This discrepancy is explained by assuming a nonlinear potential profile over the arc column. In front of the cathode, a relatively high potential gradient exists. Due to this high potential gradient, the energy is generated which is needed to maintain a plasma temperature high enough to sustain a sufficient degree of ionization.

These findings necessitate a somewhat different approach of the arc. In literature, the arc is usually presented by a simplified model, in which the electric field strength is taken to be constant for all the three regions mentioned earlier, thus implying a discontinuity at the interfaces of these regions. The present work shows that the electric field strength is much more gradually dependent on axial position. Hence, a strict distinction between the anode voltage drop, the cathode voltage drop and the voltage drop over the arc column region can not be made. This has in particular consequences for the heat balance of the cathode.

Samenvatting

In dit proefschrift wordt een onderzoek gepresenteerd dat is uitgevoerd om een beter inzicht te verkrijgen in de fundamentele warmtetransportprocessen die plaatsvinden tijdens het wolfram inert gas (TIG) lasproces. Inzicht in deze materie is onontbeerlijk voor de beschrijving van de relatie tussen lasparameters en laskwaliteit. Met het oog op de steeds toenemende automatisering en mechanisering in de industrie is deze relatie een belangrijk onderzoeksobject geworden.

Om de invloed van lasparameters zoals kathodesamenstelling, anodesamenstelling, lasstroom, booglengte, polariteit, beschermgasdebiet en beschermgassamenstelling op het warmtetransport naar de anode en kathode te bepalen zijn calorimetrische experimenten uitgevoerd. Bovendien is gebruik gemaakt van een drukvat, om daarmede de invloed van de omgevingsdruk en de beschermgassamenstelling op het warmtetransport naar de anode te kunnen bepalen. In deze laatste experimenten is de warmte-inbreng in de anode berekend uit de thermische cyclus van het werkstuk.

De lasboog kan worden onderverdeeld in drie zones. Het anodevalgebied en het kathodevalgebied worden gekenmerkt door een relatief grote spanningsval (1-8 V) over een relatief kleine afstand (~ 1 μm). De boogzuil beslaat het overige gedeelte van de boog (enkele mm) en de elektrische veldsterkte is er relatief laag (enkele V/mm). Van de drie voornoemde zones worden de processen in het anodevalgebied en het kathodevalgebied het minst begrepen. Het warmtetransport naar de anode bestaat uit termen die de spanningsval over het anodevalgebied (anodeval), de intree-arbeid van elektronen in het anodemateriaal, de thermische energie van de invallende elektronen en de convectieve en stralingsbijdragen uit de boogzuil beschrijven. Het warmtetransport naar de kathode kan op dezelfde wijze beschreven worden, zij het dat de emissie en verhitting van de elektronen warmte onttrekt aan het kathodevalgebied. In het kathodevalgebied wordt warmte geproduceerd als gevolg van de spanningsval aldaar (de kathodeval), en ten gevolge van convectie en straling uit de boogzuil.

Het blijkt, dat in de uit de literatuur bekende warmetransportmodellen de invloed van thermo-elektrische effecten niet goed wordt verdisconteerd. Zo wordt bijvoorbeeld het effect van oxydische toevoegingen aan de kathode niet op de juiste wijze geinterpreteerd. Bovendien worden Thomson effecten in de anode en kathode in het algemeen verwaarloosd.

Uit de experimenten blijkt, dat circa 75 tot 80% van het bruto boogvermogen ten goede komt aan de anode. De resultaten geven aan, dat de anodeval ongeveer 1 V bedraagt in argon beschermgas, en circa 4 V in helium. Dit komt overeen met respectievelijk 15% en 40% van de warmte-inbreng in de anode. Het convectieve warmtetransport van de boogzuil naar de anode is aanzienlijk, en bedraagt ongeveer 10 tot 20% van de warmte-inbreng in de anode. De bijdrage tengevolge van de thermische energie van de invallende elektronen is van dezelfde ordegrootte. De belangrijkste bijdrage aan de warmte-inbreng in de anode wordt echter gevormd door de invallende elektronen, die elk een energie ter grootte van de intree-arbeid van het anodemateriaal vrijmaken. Dit levert tot 60% van de totale warmte-inbreng in de anode.

De anodesamenstelling en het smelten van de anode blijken geen significante gevolgen te hebben voor de hierboven genoemde warmtetransportprocessen. Vergroting van de booglengte doet de warmte-inbreng in de anode toenemen vanwege de stijging van het convectieve warmtetransport uit de boogzuil. De warmte-inbreng in de anode is vrijwel rechtevenredig met de lasstroom, hetgeen impliceert dat de anodeval niet significant wordt beïnvloed door de lasstroom. Als de omgevingsdruk wordt verhoogd stijgt ook de warmte-inbreng in de anode tengevolge van de toeneming van de convectieve bijdrage uit de boogzuil. De verhoogde druk leidt ook tot contractie van de boog, hetgeen de lasbaddiepte sterk doet toenemen.

Als gevolg van het substantiële koelend effect van de emissie van elektronen op de kathode wordt slechts 10% of minder van het bruto boogvermogen aan de kathode afgegeven. Dit is gunstig, aangezien een hoge warmteproduktie erosie van de elektrode in de hand werkt, hetgeen nadelig is voor de produktiviteit van het lasproces. De verkregen resultaten geven aan, dat het warmtetransport naar de kathode door convectie en straling verwaarloosbaar klein is. De kathodeval is

ongeveer 7 V in argon beschermgas en is iets hoger wanneer in helium beschermgas wordt gelast.

In de praktijk worden vaak oxydes toegevoegd aan de elektrode om de las-eigenschappen te verbeteren en de elektrode-erosie te minimaliseren. Dit gunstige effect van oxydes wordt toegeschreven aan hun lage uittreepotentiaal, hetgeen de emissie van elektronen bevordert. De lage uittreepotentiaal van deze oxydes heeft echter geen direct effect op de warmtetransportvergelijking van de kathode. De lage uittreepotentiaal beïnvloedt echter wel de stroomdichtheid aan de tip van de elektrode, en verhoogt zodoende zowel de kathodeval als de warmte-inbreng in de kathode.

De booglengte bleek geen invloed te hebben op de warmte-inbreng in de kathode. Bij gebruik van helium beschermgas is de warmte-inbreng in de kathode aanzienlijk hoger dan bij gebruik van argon of argon/helium mengsels. Dit is een gevolg van de hogere kathodeval bij gebruik van helium. De kathodeval neemt ook toe als de lasstroom wordt verlaagd tot beneden 50 A.

In de boogzuil gaat warmte verloren aan de omgeving door straling, geleiding en convectie. Uit de resultaten van de calorimetrische experimenten bleek, dat dit warmteverlies lineair afhankelijk is van de booglengte. In tegenstelling tot de in de literatuur gebruikelijke veronderstelling, nadert het warmteverlies in de boogzuil echter niet tot nul als de booglengte naar nul nadert. Bij een lasstroom van bijvoorbeeld 100 A levert extrapolatie van het warmteverlies in de boogzuil naar booglengte nul een warmteverlies op van circa 140 W. Dit wordt verklaard door de veronderstelling van een niet-lineair potentiaalverloop over de boogzuil. Met name voor de kathode bestaat een grote potentiaalgradiënt, waardoor ter plaatse veel energie wordt ontwikkeld. Deze energie is noodzakelijk om het boogplasma op een temperatuur te brengen die hoog genoeg is om een voldoend hoge ionisatiegraad te bewerkstelligen.

Het voorgaande leidt noodzakelijkerwijs tot een aangepast model van de lasboog. In de literatuur wordt de lasboog in het algemeen voorgesteld als zijnde opgebouwd uit drie zones (anodevalgebied, kathodevalgebied, boogzuil), waarbij de veldsterkte in elk van deze zones constant wordt verondersteld. Dit geeft aanleiding tot discontinuïteiten op de grensvlakken van deze zones. Dit onderzoek leidt tot een

model waarin de veldsterkte een veel vloeiender verloop vertoont met de axiale positie in de lasboog. Het is daarom niet juist, een strikt onderscheid te maken tussen de potentiaalvallen in het anodevalgebied, het kathodevalgebied en de boogzuil. Dit heeft vooral consequenties voor de warmtebalans van de kathode.

LEVENSLOOP

De schrijver van dit proefschrift werd geboren op 8 augustus 1960 te Langedijk. Na het doorlopen van het Atheneum B aan het Petrus Canisius College in Alkmaar werd in september 1978 begonnen met de studie metaalkunde aan de toenmalige Tussenafdeling der Metaalkunde van de T.H. Delft. Het propadeutisch examen (P2) en kandidaatsexamen (K2) werden afgelegd in respectievelijk oktober 1980 en juni 1983. In de sectie Lastechnologie en Niet-Destructief Onderzoek werd het afstudeeronderzoek betreffende het diffusielassen van aluminiumoxyde aan goud voltooid, waarop in juni 1984 het ingenieursdiploma werd behaald. In dezelfde sectie werd daarop een onderzoek aangevangen naar de invloed van de omgevingsdruk op het TIG- en MIG-lasproces. Van 1986 tot 1990 werd het promotieonderzoek naar het warmtetransport tijdens het TIG-lasproces uitgevoerd, hetgeen tot het voor U liggende proefschrift heeft geleid. De schrijver dezes heeft inmiddels een baan geaccepteerd als tijdelijk onderzoeker bij het National Research Institute for Metals in Tokyo, Japan, waar hij de komende twee jaar onderzoek zal verrichten.